University of Reading

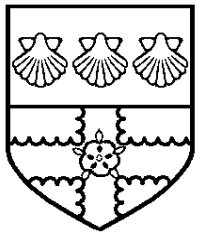

A Nonhydrostatic Numerical Model in σ-coordinates and Simulations of Mesoscale Phenomena

by

Ming Xue

A dissertation submitted in partial fulfilment

of Doctor's Degree of Philosophy in Meteorology

Department of Meteorology

July, 1989

ABSTRACT

A nonhydrostatic mesoscale numerical model is developed and simulations of various mesoscale phenomena using this model are described.

The model is based on a quasi-nonhydrostatic equation system in the normalized pressure – σ coordinates. The system is free of vertical sound waves but contains Lamb wave modes which are however significantly retarded in nonhydrostatic regime. An integration time step comparable to that of an anelastic model system can be used when grid length is around a few kilometres. The current model includes also parameterized microphysical processes.

The solution procedure of the model is analogous to that of an anelastic system in terrain-following height-coordinates. An elliptic equation has to be solved for the geopotential height perturbation. Conventional finite differencing techniques are used except in the advection of thermodynamical variables, where the flux-corrected transport scheme (FCT) is employed. FCT eliminates the problem of 'negative water' generation and significantly improves the model accuracy. Radiative conditions are applied at the lateral boundaries, and at the upper boundary radiative condition is simulated by an absorbing layer. Subgrid scale turbulence is parameterizd using the deformation and Richardson number dependent formulation. Three water phases, i.e. water vapour, cloud water and rain water, are present in the model with Kessler's microphysics parameterizations being adopted.

A number of two dimensional mesoscale problems are studied using the model. They include, dry and moist gravity waves and related phenomena in stratified air streams flowing over a 2-D ridge, long-lived squall line systems and deep orographic convection.

Firstly, the model solutions of small amplitude mountain gravity waves in various regimes are verified against analytical solutions and good agreement is found. The model is then used to simulate the 1972 Boulder severe downslope windstorm and the results lend further support to Smith's nonlinear flow transition mechanism of severe downslope winds. Two events of mountain lee waves which occurred over the west of the British Isles are also studied. The lee wave patterns observed from satellite are well reproduced, and furthermore, the effects of mountain height and scales, orography spectrum and moisture condensation on the formation and evolution of trapped lee waves and associated clouds are examined.

A series of simulations of long-lived squall lines is performed which demonstrate in particular the role of the interaction between cold pool outflow and low-level ambient inflow, and the mechanism by which such an interaction determines and maintains an optimal state of squall line convection. It is shown that it is the momentum rather than the

vorticity in the inflow that plays the key role. An optimal condition for the most intense, long-lasting squall lines is proposed based on the propagation speed of the cold pool. The sensitivities of convection to the use of FCT scheme, to spatial resolution and to diffusion are also examined.

Deep orographic convection is also studied using the σ-coordinate model. The Big Thompson storm that remained quasi-stationary on the upwind slope of the Front Range of the Rocky Mountains and caused flash floods is simulated. An intense and quasi-stationary storm is obtained when an isolated orography profile is used. A plateau type mountain is found to produce fast-moving storm systems which is explained in terms of the cold outflow strength. Experiments showing the effect of modifications to an ambient sounding are also presented and finally the restrictions of two-dimensionality on the storm simulations discussed.

Table of Contents

CHAPTER ONE

CHAPTER TWO

CHAPTER THREE

CHAPTER FOUR

CHAPTER FIVE

CHAPTER SIX

CHAPTER SEVEN

Chapter One

General Introduction and the Quasi-Non-Hydrostatic Equation System

1.1 General introduction

The purpose of this research is to develop a mesoscale numerical model based on a new equation system, i.e. the quasi-nonhydrostatic system in pressure-based sigma-coordinates (Miller and White, 1984), to explore and exploit the unique features of this model and to study problems in relation to various types of orographic forcing and nonhydrostatic convective processes.

Essentially all limited area and global scale weather forecasting models use pressure or normalized pressure σ as the vertical coordinate. The use of a pressure-based coordinate system circumvents the difficulties in determining air density which is not routinely observed, and facilitates the use of observational data generally made on pressure levels. On the other hand, almost all nonhydrostatic meteorological models are based on height coordinates. The anelastic equation system derived by Ogura and Phillips (1962) is the foundation of most of these models. More recently, the fully compressible equation set in height coordinates has also been used in formulating small-to-mesoscale numerical models (e.g. Klemp and Wilhelmson, 1978).

However, Miller (1974) demonstrated that a quasi-nonhydrostatic equation system could also be obtained in pressure coordinates, and a numerical model using this system of equations was developed (Miller and Pearce, 1974) and was later on successfully used in modeling studies of convective storms. This equation system was further extended to

σ-coordinates by Miller and White (1984) so that irregular bottom terrain can be treated similarly as in large scale σ-coordinate system. In pressure based coordinates, the thermodynamic calculations are more straightforward since pressure itself is a state variable. Based on such a coordinate system, a nonhydrostatic mesoscale model will have the same advantages as its hydrostatic counterpart, moreover, it is potentially advantageous to nest with large scale numerical models.

The σ-coordinate quasi-nonhydrostatic equation system is introduced in the rest of this chapter and the properties of the system are discussed in some detail.

Chapter two deals with the numerical solution of dynamical processes in the model. The solution procedure of dynamical processes is analogous to that for the anelastic system in terrain-following height coordinates but there are extra complications due to the time dependence of the surface pressure. A complicated elliptic equation has to be solved for the geopotential height perturbation. The numerical aspects of finite differencing, time integration, boundary conditions and the methods to solve the elliptic equation are discussed and described in detail.

Chapter three is devoted to the thermodynamical, microphysical and diabatic processes. An accurate, shape-preserving (positive definite for positive scalars) advection scheme (FCT) is used to advect the thermal and water quantities and its implementation in the model are described first. The current model includes three water phases, namely, water vapour, cloud water and rain water. The treatment of microphysical processes including evaporation and condensation of water vapour, auto-conversion and accretion to rain water and the rain water evaporation and sedimentation are presented. Finally in this chapter, the parameterization of sub-grid scale turbulence and formulations of numerical diffusion are discussed.

Chapter four is a study of a variety of dynamical problems of flow over mountain ridges. It starts with a review of theories of mountain gravity waves, followed by a section of model experiments of basically linear mountain waves in various wave regimes. The comparison of these results with analytical solutions serves as a verification

to the model dynamics. At the same time, the procedure of model initialization and the use of the hydrostatic version of this model are discussed. The section that follows deals with mountain gravity waves with large amplitudes. An introduction to severe downslope winds associated with these large amplitude waves are given, and then simulations of the 11 January 1971 Boulder severe downslope wind storm using our model are reported. A final state of flow that has a surface drag ten times that of the linear prediction and three times that of the value obtained by previous investigators (e.g. Peltier and Clark, 1979) is obtained. The flow field at this stage very closely resembles the observed field and the nonlinear solution of Smith (1985). The mechanism of wave amplification is clearly demonstrated. Section 4.5 describes a series of dry and moist numerical experiments of mountain lee waves with two observed soundings. The observed lee wave clouds are well reproduced, and further the effects of atmospheric structure and the condensation of moisture on the lee wave formation and evolution are studies. Certain theoretical explanations are provided.

In Chapter five are numerical studies on long-lived convective system - squall lines. A review is first given on the current understandings on the development and evolution of squall lines, especially those in two dimensional framework. A set of experiments with idealized wind profiles and a fixed thermodynamic sounding are designed to examine the role of the interaction between the rain-induced outflow from the system and the low-level inflow and also the mechanism by which such interaction determines the fate of squall lines. The role of vorticity versus momentum in the inflow is discussed. A criterion or optimal condition for long-lived squall lines is suggested. In this chapter, we also examine the sensitivities of convection to model resolution and diffusion formulations.

Deep orographic convection is studied in Chapter six. This is where the potential of the current model is explored to the largest extent. The study attempts to simulate the Big Thompson storm that occurred over the Big Thompson Canyon, Rocky Mountains and caused flash floods in the river drainage on 31 July to 1 August, 1976 (Caracena, et al. 1979). A pre-storm sounding is used as the model input and different types of mountain

profiles are used. The quasi-stationary Big Thompson storm is successfully simulated in certain experiments. The effects of the mountain shape and height and the modification to the moisture profile are examined

Finally, Chapter seven gives a brief summary on the results of this work and draws a number of interesting conclusions.

1.2 Quasi-non-hydrostatic (QNH) equation system

Pressure has been widely used as a vertical coordinate in modeling and theoretical studies of large-scale hydrostatic flows ever since the pioneering work of Eliassen (1949). The advantages of using pressure coordinates in meteorological applications are generally recognized. The use of pressure as the vertical coordinate, together with the hydrostatic relation, eliminates from the governing equations the density of the air, which is a quantity that is not routinely observed in meteorology. Moreover its use simplifies the mass continuity equation. The further transformation into σ-coordinate that was first introduced by Phillips (1957) circumvents the difficulties with the lower boundary, which is often not a surface of constant pressure. However pressure (or normalized pressure σ) coordinates were not used for non-hydrostatic flows until Miller (1974) and Miller and Pearce (1974), who derived and used for cumulonimbus studies a quasi-non-hydrostatic set of equations in pressure coordinates. This set of equations has since been extensively used in numerical simulations of cumulonimbus and related studies (e.g. Miller and Pearce (1974), Moncrieff and Miller (1976), and Thorpe, et. al. (1982)). Miller and White (1984) presented a more vigorous derivation of the equation set of Miller (1974) by performing systematic scaling analysis and power series expansion. A sigma-coordinate (defined as pressure divided by the surface pressure) equation set was obtained by direct transformation from the pressure coordinate counterpart. The energy conservation of the approximated equation systems and the existence of physical wave modes in them are discussed in their paper.

1.2.1 Basic equations

The primitive equation set governing the motion of air as a perfect gas consists of the momentum, mass continuity, and thermodynamic equations. For simplicity the friction terms and diabatic terms are neglected for the moment, but will be included later. These equations in geometric height coordinates on an f-plane are:

$$\frac{du}{dt} - fv = -\frac{1}{\rho}\frac{\partial p}{\partial x} \tag{1.2.1}$$

$$\frac{dv}{dt} + fu = -\frac{1}{\rho}\frac{\partial p}{\partial y} \tag{1.2.2}$$

$$\frac{dw}{dt} = -\frac{1}{\rho}\frac{\partial p}{\partial z} - g \tag{1.2.3}$$

$$\frac{\partial u}{\partial x} + \frac{\partial v}{\partial y} + \frac{\partial w}{\partial z} = -\frac{d}{dt}(\ln\rho) \tag{1.2.4}$$

$$\frac{d\theta}{dt} = 0 \tag{1.2.5}$$

$$\theta = T\left(\frac{p_0}{p}\right)^{\kappa} = \frac{T}{\Pi} \tag{1.2.6}$$

where the non-dimensional pressure

$$\Pi \equiv \left(\frac{p}{p_0}\right)^{\kappa}$$

and the substantial derivative is defined as

$$\frac{d}{dt} = \frac{\partial}{\partial t} + u\frac{\partial}{\partial x} + v\frac{\partial}{\partial y} + w\frac{\partial}{\partial z}.$$

All the partial differentiations with respect to t, x and y are carried out at constant height z.

Following meteorological conventions, **u** = (u, v, w) is the velocity vector in Cartesian coordinates (x, y, z) and equations (1.2.3), (1.2.4) and (1.2.5) are the momentum equations for the three components. $f=2\Omega\sin\varphi$ (φ is the earth latitude) is the Coriolis parameter. Eq.(1.2.4) is the mass conservation equation and (1.2.5) the

thermodynamic equation. θ is potential temperature which is defined by (1.2.6) where $\kappa \equiv R/C_p$ with R being the gas constant for dry air, C_p the specific heat of dry air at constant pressure, and p_0=1000 HPa. The pressure p, density ρ and temperature T satisfy the ideal gas law $p=\rho RT$.

For mesoscale flows, the Rossby number is of order unity so that the Coriolis terms are important. However, for simplicity the Coriolis effects are not included in the rest of this chapter when we derive briefly the Quasi-non-hydrostatic equation system. This effect can readily be included in the equation system obtained, and it is included in the actual numerical model as will be seen in chapter three. And for the same reason, we will be discussing the equation system in a two dimensional frame work (independent of coordinate y), but the extension into three dimensions is straightforward. The simplified equation set is then

(Set A)

$$\frac{du}{dt} = -\frac{1}{\rho}\frac{\partial p}{\partial x} \qquad (1.2.7)$$

$$\frac{dw}{dt} = -\frac{1}{\rho}\frac{\partial p}{\partial z} - g \qquad (1.2.8)$$

$$\frac{\partial u}{\partial x} + \frac{\partial w}{\partial z} = -\frac{d}{dt}(\ln\rho) \qquad (1.2.9)$$

$$\frac{d\theta}{dt} = 0 \qquad (1.2.10)$$

The numerical model is formulated in two dimensions as a first attempt, but it is formulated such that the extension into a three dimensional form is straightforward. Issues related to the three dimensional formulation of the model are addressed where appropriate.

1.2.2 Quasi-non-hydrostatic (QNH) equations in p and σ-coordinates

a) The equation system in pressure coordinates

Following the notation of Miller and White (1984), we define the quantity

$$\varepsilon \equiv \frac{1}{g}\frac{dw}{dt} = g^{-2}\,\frac{d}{dt}\left(\frac{d\Phi}{dt}\right)$$

which is the ratio of the vertical acceleration to gravitational force where $\Phi = gh$, being the geopotential height. Equations (1.2.7)-(1.2.10) can then be transformed to pressure coordinates (x, p, t) as

$$\frac{du}{dt} = -(1+\varepsilon)\frac{\partial\Phi}{\partial x} \qquad (1.2.11)$$

$$\frac{RT}{p} = -(1+\varepsilon)\frac{\partial\Phi}{\partial p} \qquad (1.2.12)$$

$$\frac{\partial u}{\partial x} + \frac{\partial\omega}{\partial p} = \frac{d}{dt}[\ln(1+\varepsilon)] \qquad (1.2.13)$$

$$\frac{d\theta}{dt} = 0 \qquad (1.2.14)$$

Here,

$\omega = \frac{dp}{dt}$, is the velocity in p-coordinates, and

$$\frac{d}{dt} \equiv \frac{\partial}{\partial t} + u\frac{\partial}{\partial x} + \omega\frac{\partial}{\partial p}$$

is the substantial derivative in pressure coordinates. All the partial differentiations with respect to x and t are performed at constant p.

Equation (1.2.12) establishes an un-approximated relation between geometric height and pressure. This relation is used for the coordinate transformation. This relation also implies that the non-hydrostatic system is feasible in p-coordinates as far as $|\varepsilon| < 1$ holds so that pressure is always a monotonic function of height. The non-hydrostatic contribution comes in as merely a deviation from this function without violating the monotonicity. If $\varepsilon << 1$, and all terms multiplied by ε are neglected then the above equation set approximates to the usual hydrostatic pressure coordinate one.

The vertical coordinate σ is defined here as:

$$\sigma = \frac{p - p_t}{p_{surf} - p_t} = \frac{p-p_t}{p_*}$$

where p_{surf} is the surface pressure, p_t is the pressure at the top boundary which is a specified constant and p_* the pressure difference between the surface and top boundary. The equation set in σ-coordinates (x, σ, t) can be obtained by direct transformation form equations (1.2.7)-(1.2.10) or from (1.2.11)-(1.2.14),

$$\frac{du}{dt} = -(1+\varepsilon)\frac{\partial \Phi}{\partial x} - \frac{RT}{p_*}\frac{\partial p_*}{\partial x} \qquad (1.2.15)$$

$$\frac{RTp_*}{p} = -(1+\varepsilon)\frac{\partial \Phi}{\partial \sigma} \qquad (1.2.16)$$

$$\frac{\partial u}{\partial x} + \frac{\partial \dot{\sigma}}{\partial \sigma} = -\frac{d}{dt}(\ln p_*) + \frac{d}{dt}[\ln(1+\varepsilon)] \qquad (1.2.17)$$

$$\frac{d\theta}{dt} = 0 \qquad (1.2.18)$$

Here $\dot{\sigma} = d\sigma/dt$ is the vertical velocity in σ-coordinates. The substantial derivative is defined as

$$\frac{d}{dt} \equiv \frac{\partial}{\partial t} + u\frac{\partial}{\partial x} + \dot{\sigma}\frac{\partial}{\partial \sigma}$$

and all the partial differentiations with respect to x and t are carried out at constant σ.

The equation sets (1.2.11)-(1.2.14) and (1.2.15)-(1.2.18) are the exact transformations of the height coordinate equation set (1.2.7)-(1.2.10). They support all the physical wave modes including acoustic waves and are too cumbersome so that approximations must be made to them before they can be put into practical use.

Similar to the way in which the anelastic equation set was obtained by Ogura and Phillips (1962), Miller (1974) expanded equations (1.2.11)-(1.2.14) around a reference state of no motion, namely

$$\Phi = \Phi_s(p) + \Phi'(x, p, t) \qquad (1.2.19)$$

$$\theta = \theta_s(p) + \theta' (x, p, t) \quad .$$

Here the subscript 's' denotes the reference state while primed variables represent deviations from the reference state. The reference state should be in hydrostatic balance therefore

$$\frac{d\Phi_s}{dp} = - \frac{R\theta_s}{p} \left(\frac{p}{p_0} \right)^{\kappa} \qquad (1.2.20)$$

Substituting the above into the equations (1.2.11) - (1.2.14) and then neglecting various small terms a simplified equation set is obtained in which the vertical acceleration term

$$\frac{1}{g} \frac{dw}{dt}$$

is approximated by

$$\frac{d}{dt} \left(- \frac{\omega}{g\rho_s} \right)$$

where ρ_s is the reference state density. Miller and White (1984) formally justified these approximations by performing a systematic scaling and power series expansion in a small parameter they identified as

$$\alpha = \frac{p_0}{\theta_s} \frac{\partial \theta_s}{\partial p} = \frac{\Delta \theta_s}{\theta_s} \ , \qquad (1.2.21)$$

the fractional change of the potential temperature of reference state over a typical convective scale depth. For our applications the assumption that $\alpha << 1$ is almost always valid. The zero order balance of the equations expanded in small parameter α turns out to be exactly equivalent to that obtained by Miller (1974). These equations are:

$$\frac{du}{dt} = - \frac{\partial \Phi'}{\partial x} \qquad (1.2.22)$$

$$\frac{d\tilde{w}}{dt} = r_s \frac{\partial \Phi'}{\partial p} + g \frac{\theta'}{\theta_s} \qquad (1.2.23)$$

$$\frac{\partial u}{\partial x} + \frac{\partial \omega}{\partial p} = 0 \qquad (1.2.24)$$

$$\frac{d\theta'}{dt} = - \frac{\theta_s}{g} N_s^2 \tilde{w} \tag{1.2.25}$$

$$\tilde{w} \equiv - \omega \frac{RT_s}{gp} = - \frac{\omega}{r_s} \tag{1.2.26}$$

where

$$r_s \equiv g\rho_s = \frac{gp}{RT_s} \tag{1.2.27}$$

and

$$N_s^2 = - \frac{g\, r_s}{\theta_s} \frac{\partial \theta_s}{\partial p} \tag{1.2.28}$$

is the static stability of the reference state.

In the above equations potential temperature is used as a dependent variable instead of temperature as in the original equations. Notice here that the vertical acceleration term is retained only in the vertical momentum equation while its contribution is neglected elsewhere. This is analogous to the quasi-geostrophic theory in which the ageostrophic contribution only comes in through divergence term while geostrophy is assumed for all the other terms.

To integrate forward in time the equation system (1.2.22)-(1.2.25), a diagnostic equation for the geopotential perturbation Φ' is required. It can be readily obtained by applying a divergence operator on the momentum equations and making use of the continuity equation (1.2.24), that is, performing

$$\frac{\partial}{\partial x} \{ \text{ 1.2.22 } \} + \frac{\partial}{\partial p} \{ r_s \, (\text{ 1.2.23 }) \}$$

which results in

$$\frac{\partial^2 \Phi'}{\partial x^2} + \frac{\partial}{\partial p}\left(r_s^2 \frac{\partial \Phi'}{\partial p} \right) = 2 \boldsymbol{J}_{xp} (u, \omega) - \frac{\partial}{\partial p}\left[r_s g \frac{\theta'}{\theta_s} - \frac{\omega^2}{r_s} \frac{dr_s}{dp} \right] \tag{1.2.29}$$

in which $\boldsymbol{J}_{xp}$ is the Jacobian with respect to x and p,

$$J_{xp}(u, \omega) = \frac{\partial u}{\partial x}\frac{\partial \omega}{\partial p} - \frac{\partial u}{\partial p}\frac{\partial \omega}{\partial x} .$$

Equation (1.2.29) is elliptic and can be solved given appropriate boundary conditions.

b) The quasi-non-hydrostatic equations in σ-coordinates

The equivalent quasi-non-hydrostatic equation set in σ-coordinates can be obtained by directly transforming from equations in pressure coordinates. The resulting equations are:

$$\frac{du}{dt} = -\frac{\partial \Phi'}{\partial x} + \frac{\sigma}{p_*}\frac{\partial p_*}{\partial x}\frac{\partial \Phi'}{\partial \sigma} \qquad (1.2.30)$$

$$\frac{d\tilde{w}}{dt} = \frac{g}{RT_s}\frac{p}{p_*}\frac{\partial \Phi'}{\partial \sigma} + g\frac{\theta'}{\theta_s} \qquad (1.2.31)$$

$$\frac{d\ln p_*}{dt} + \frac{\partial u}{\partial x} + \frac{\partial \dot{\sigma}}{\partial \sigma} = 0 \qquad (1.2.32)$$

$$\frac{d\theta'}{dt} = -\frac{\theta_s}{g} N_s^2 \tilde{w} \qquad (1.2.33)$$

$$\tilde{w} \equiv -\left(p_* \dot{\sigma} + \sigma \frac{dp_*}{dt} \right) / r_s \qquad (1.2.34)$$

in which the static stability parameter

$$N_s^2 = -\frac{g r_s}{\theta_s p_*}\frac{\partial \theta_s}{\partial \sigma} \qquad (1.2.35)$$

and r_s is as defined before. All the partial differentiations are carried out at constant σ here. The quantity $\tilde{w}$, the same as that in equation (1.2.26), can be regarded as the approximated vertical velocity. As will be shown in next section $\tilde{w}$ contributes to the kinetic energy in a consistent manner.

It should be pointed out that the reference state is no longer only a function of the vertical coordinate σ, but also dependent on x. For the reference state to be in hydrostatic balance the following relations must be satisfied:

$$-\left(\frac{\partial \Phi_s}{\partial x}\right)_p = -\left(\frac{\partial \Phi_s}{\partial x}\right)_\sigma + \frac{\sigma}{p_*}\frac{\partial p_*}{\partial x}\frac{\partial \Phi_s}{\partial \sigma} = 0 \qquad (1.2.36)$$

$$\frac{\partial \Phi_s}{\partial \sigma} + \frac{RT_s p_*}{p} = 0 \qquad (1.2.37)$$

Here $\Phi_s = \Phi_s(p) = \Phi_s(x, \sigma, t)$.

These relations are used later to calculate Φ_s and Φ' at $\sigma=1$. i.e. at $p=p_{surf}(x, t)$, which are required as the lower boundary conditions for the diagnostic equation for Φ'.

The diagnostic equation for Φ' in σ-coordinates is obtained by transforming from the p-coordinate equation (1.2.29),

$$\frac{\partial^2 \Phi'}{\partial x^2} - \frac{2\sigma}{p_*}\frac{\partial p_*}{\partial x}\frac{\partial^2 \Phi'}{\partial x \partial \sigma} + \frac{\partial}{\partial \sigma}\left(S^2 \frac{\partial \Phi'}{\partial \sigma}\right) + \left(\frac{1}{p_*}\frac{\partial p_*}{\partial x}\right)^2 \frac{\partial}{\partial \sigma}\left(\sigma^2 \frac{\partial \Phi'}{\partial \sigma}\right)$$

$$-\frac{\sigma}{p_*}\frac{\partial^2 p_*}{\partial x^2}\frac{\partial \Phi'}{\partial \sigma} = 2\left[-\frac{\partial u}{\partial x}\frac{\partial (S\tilde{w})}{\partial \sigma} + \frac{1}{p_*}\frac{\partial (p_* S\tilde{w})}{\partial x}\frac{\partial u}{\partial \sigma}\right]$$

$$-\frac{\partial}{\partial \sigma}\left(Sg\frac{\theta'}{\theta_s} - p_* \tilde{w}^2 \frac{\partial S}{\partial \sigma}\right) \qquad (1.2.38)$$

Here $$S \equiv \frac{gp}{RT_s p_*} = \frac{r_s}{p_*}, \qquad (1.2.39)$$

and it has the dimension of H^{-1}, i.e. that of the inverse scale height. It can be shown that this equation is elliptic and in any case an equation should not change its property after transformation.

1.2.3 Solution procedure of the QNH equation system

In the set of equations (1.2.30)-(1.2.34), there are six variables: u, $\tilde{w}$, $\dot{\sigma}$, θ, Φ' and p_*, whereas we have only five equations as the diagnostic equation is merely a derived equation from equations (1.2.15), (1.2.16) and the continuity equation (1.2.32).

However it should noted that variable p_* is special because it is only a boundary variable. One more relation can be obtained by extracting information from the lower boundary conditions. We have

$$\dot{\sigma} = 0 \text{ at } \sigma = 0 \text{ and } \sigma = 1,$$

manipulating the continuity equation and integrating it from the surface to the top boundary results in

$$\frac{\partial p_*}{\partial t} = -\int_0^1 \frac{\partial p_* u}{\partial x}\, d\sigma \qquad (1.2.40)$$

which states that the surface pressure variation is a result of mass convergence/ divergence in the column directly above the surface. Without extra source and sink terms Eqs. (1.2.30)-(1.2.34) and (1.2.40) now constitute a closed equation set.

If at a time t_0, u, w, Φ', θ', and p_* are given, then the solution procedure would be:

1) integrate prognostic equations (1.2.30), (1.2.31), (1.2.33), (1.2.40) for u, w, θ' and p_* at time $t_0+\Delta t$,

2) calculate $\dot{\sigma}$ at time $t_0+\Delta t$ from diagnostic relation (1.2.34) in which term $\partial p_*/\partial t$ is substituted for using (1.2.40),

3) solve elliptic equation (1.2.38) for Φ' with the right hand side of the elliptic equation being known at $t=t_0+\Delta t$. Up to now the fields at the new time are all known, the same integration cycle can then be repeated.

Note that in the above procedure, the continuity equation is not explicitly solved but it is implicitly involved in the elliptic equation. The solution of the later should ensure mass continuity. In the numerical model a method after Harlow and Welch (1965) is adopted to improve the solution in this aspect.

A different procedure of solution can be taken which does not solve the vertical momentum equation explicitly but integrates the continuity equation (1.2.32) instead

for $\dot{\sigma}$. Vertical velocity $\tilde{w}$ is then calculated from (1.2.34). This approach is closer to the way the hydrostatic σ or p-coordinate equations are solved, and was used by Miller and Pearce (1974) as a first version of their 3-D pressure coordinate cloud model. The model described in this thesis follows the first procedure of solution as we feel that the vertical and horizontal components of momentum are better to be treated in a similar way, especially for small-to-mesoscale flows in which both components are comparable in magnitude.

The elliptic equation in σ-coordinates is complicated by the presence of cross-differentiation terms on the left hand side. It is therefore no longer a standard Poisson equation and can not be solved by direct methods. However, as will be show later, this equation can still be solved efficiently through combined use of direct methods and iterative techniques.

1.3 Some properties of the quasi-non-hydrostatic system

1.3.1 Introduction

We presented in the previous section the approximated quasi-non-hydrostatic equation sets in p and σ coordinates. It is worthwhile to look at their conservation properties in order to be certain of the dynamic consistency of these equation sets. In the subsections that are to follow, the conservation of the total energy is examined. Further more it is equally important to understand the physical wave modes that are supported by the system. In another subsection the results of the analysis of Miller and White (1984) on these wave modes are summarized and some discussion are included.

1.3.2 Energetics

In this section we examine the energy conservation of the equation system in σ-coordinates. The analysis of the conservation in p-coordinates is similar and is not

presented.

We define the quantity $\frac{1}{2}\tilde{w}^2$ as the contribution to the kinetic energy by the vertical component of motion. Performing operation

$$p_* u \cdot \text{eq.(1.47)} + p_* \tilde{w} \cdot \text{eq.(1.48)}$$

and incorporating eq.(1.2.32) results in the kinetic energy equation

$$p_* \frac{d}{dt}\left[\frac{1}{2}(u^2 + \tilde{w}^2)\right]$$

$$= -\left[\frac{\partial(p_* u\Phi')}{\partial x} + \frac{\partial(p_*\dot{\sigma}\Phi')}{\partial \sigma}\right] - \frac{\partial(\Phi'\sigma)}{\partial \sigma}\frac{\partial p_*}{\partial t} + p_* \tilde{w}\, g \frac{\theta'}{\theta_s} \qquad (1.3.1)$$

An equation for total perturbation potential energy (the sum of the internal energy and potential energy) can be derived from the thermodynamic equation, noting that from definitions $\theta' = T'/\Pi$ and $\theta_s = T_s/\Pi$,

$$p_* \frac{d}{dt}\left(C_p T'\right) = p_* C_p \Pi \frac{g}{r_s \theta_s} N_s^2 \omega + \frac{p_* RT'}{p}\omega$$

$$= -p_* C_p \Pi \frac{g}{\theta_s} N_s^2 \tilde{w} - p_* g \tilde{w} \frac{\theta'}{\theta_s}. \qquad (1.3.2)$$

The two terms on the right hand side represent respectively the extraction of total potential energy from the reference state and the conversion between the total potential energy and kinetic energy.

Adding (1.3.1) and (1.3.2) together yields

$$p_* \frac{d}{dt}\left[\frac{1}{2}(u^2 + \tilde{w}^2) + C_p T'\right] =$$

$$-\left[\frac{\partial(p_* u\Phi')}{\partial x} + \frac{\partial(p_*\dot{\sigma}\Phi')}{\partial \sigma}\right] - \frac{\partial \sigma\Phi'}{\partial \sigma}\frac{\partial p_*}{\partial t} - p_* C_p \Pi \frac{g}{\theta_s} N_s^2 \tilde{w} \qquad (1.3.3)$$

After a series of manipulations an equation for the total energy is derived from (1.3.3) as:

$$p_* \frac{d}{dt}\left[\frac{1}{2}\left(u^2+\tilde{w}^2\right)+C_pT\right]=$$

$$-\left[\frac{\partial(p_* u\Phi)}{\partial x}+\frac{\partial(p_*\dot{\sigma}\Phi)}{\partial\sigma}\right]-\frac{\partial\sigma\Phi}{\partial\sigma}\frac{\partial p_*}{\partial t} \qquad (1.3.4)$$

Equation (1.3.4) is the same as that in Miller and White (1984) and is similar to the total energy equation implied by the usual hydrostatic σ-coordinate equations except for the extra contribution of $\frac{1}{2}\tilde{w}^2$ to the kinetic energy.

Written in a flux form equation (1.3.4) becomes

$$\frac{\partial(p_* E)}{\partial t}=-\left[\frac{\partial p_* u(E+\Phi)}{\partial x}+\frac{\partial p_*\dot{\sigma}(E+\Phi)}{\partial\sigma}\right]-\frac{\partial\sigma\Phi}{\partial\sigma}\frac{\partial p_*}{\partial t} \qquad (1.3.5)$$

where the total energy

$$E \equiv \frac{1}{2}\left(u^2+\tilde{w}^2\right)+C_pT\ .$$

Upon integrating the total energy equation (1.3.5) over the whole domain of a model atmosphere we obtain an energy budget equation

$$\frac{\partial\hat{E}}{\partial t}=-\left[\int_0^1 p_* u\,(E+\Phi)\,d\sigma\right]_{x_1}^{x_2}-\int_{x_1}^{x_2}\left[\Phi\big|_{\sigma=1}\frac{\partial p_*}{\partial t}\right]dx \qquad (1.3.6)$$

Here $$\hat{E}=\int_0^1\int_0^1\int_{x_1}^{x_2}(p_* E)\,dx\,dy\,d\sigma$$

is the total energy of the air inside the integrated domain. In the y direction the integration range is chosen as unity since the flow is independent of y.

The above energy conservation suggests that the derived equation system is dynamically consistent. At the same time the energy budget calculation is a good diagnostic tool in checking the fidelity of the computer program.

1.3.3 Physical wave modes in the QNH system

The physical wave modes that are supported by an equation system are always of major concern to numerical modelers because meteorologically insignificant fast waves like acoustic waves impose a too strong limitation on the integration time steps that can be used without inducing numerical instability. However physically important waves should be treated properly by the model.Miller and White (1984) performed a detailed analysis of the quasi-non-hydrostatic (QNH) equations linearized around an isothermal reference state. It is found that the system supports no vertically propagating sound waves, either in pressure or in σ-coordinates.Gravity waves are (and should be) retained with no change of vertical structures and only a slight changes of phase speeds (the hydrostatic set produces much larger changes of gravity wave phase speeds). Lamb waves, i.e. the horizontally propagating sound waves, are present in the system, but can be eliminated in pressure coordinates by imposing the lower boundary condition $\omega=0$ at $p=p_0$. This is not difficult to understand because the Lamb waves have maximum amplitudes at the lower boundary but decay exponentially away from the boundary. The above-mentioned boundary condition suppresses any disturbances that could have existed. Lamb waves exist also in the σ-coordinate system but they can not be removed in the same way. The lower boundary condition is in this case applied at $\sigma=1$, i.e. at $p=p_{surf}$ hence the condition is non-linear and the surface pressure p_{surf} itself contains the ingredient of Lamb wave oscillations. It is important to note that Lamb waves exist in the hydrostatic σ-coordinate system as well, but their presence is sometimes overlooked as the limitation on the integration time steps is attributed to the fast external gravity waves. Implicit or semi-implicit techniques are usually employed to treat the fast waves in large scale models (e.g. Simmons and Hoskins (1975)) so that reasonably large time steps are permitted. The same techniques are difficult to implement with our equation system, however the problem is not as serious as it appears in the first instance because the Lamb wave modes found in the QNH system are significantly retarded! The phase speed of the Lamb waves

is given by Miller and White (1984) as:

$$C_L = \mp \sqrt{\gamma R T_0 \left(1 - G(b) \right)} \qquad (1.3.7)$$

where G(b) is the fractional reduction on phase speed, with $b=2\pi/kH_0$, k being the horizontal wave length and $\gamma=1.4$. It is found that the retardation of the Lamb waves is considerable. It is more than 50% for a wave of horizontal wave length $2H_0$ and 10% for a wave with $L=16H_0$. The numerical experiments in a later chapter confirm these results.

1.3.4 Other conservation properties of QNH system and discussions

Johnson (1978) studied the vorticity properties of the quasi-non-hydrostatic pressure-coordinate system. He found that there exists an analogue of Ertel's potential vorticity theorem. White (personal communication) extended the original Miller's equation system to include the horizontal mesoscale variations of the reference state and demonstrated the existence of the equivalent conservation theorem also in the extended system as long as the vorticity is suitably defined. These conservation properties are equally true of the σ-coordinate system as it is directly transformed from the p-coordinate equations. The existence of the equivalent Ertel's potential vorticity theorem again lends support to the dynamic consistency of the QNH system and it also consolidates the theoretical background for further development of numerical models based on this system of equations.

The QNH equation set (1.2.22)-(1.2.25) is the pressure coordinate counterpart of the anelastic equation set in height coordinates obtained by Ogura and Phillips (1962). They are both valid for describing small scale deep convection, however they are not exact transformations of each other. Their similarities and differences can be better understood by examining the approximations made to obtain them.

Equation (1.2.12) can be rewritten as:

$$\rho\delta z = \frac{1}{g\,(\,1+\varepsilon\,)}\,(\,-\,\delta p\,)\ ,$$

where (δz) and ($-\delta p$) are the vertical displacement in height and pressure coordinates respectively.

The quantity $1/g(1+\varepsilon)$ can be regarded as an analogue of density ρ in pressure coordinates since

$$\frac{1}{g\,(\,1+\varepsilon\,)} = \frac{\rho\delta z\,\delta x\delta y}{-\delta p\,\delta x\delta y} = \frac{\text{mass}}{\text{element volume}}\ .$$

From the continuity equation in height coordinates or from the first principle of mass continuity, the continuity equation in p-coordinates is obtained as:

$$-\frac{d}{dt}\ln(\,1+\varepsilon\,) + (\,\frac{\partial u}{\partial x} + \frac{\partial \omega}{\partial p}\,) = 0\ .$$

Since $\ln(1+\varepsilon)=\varepsilon+O(\varepsilon^2)$, then

$$-\frac{d\varepsilon}{dt} + (\,\frac{\partial u}{\partial x} + \frac{\partial \omega}{\partial p}\,) \approx 0.$$

The term $d\varepsilon/dt$, i.e. the change in the equivalent density due to vertical acceleration, is neglected in the QNH system, and it is the neglect of this term that rules out the possible acoustic oscillations in the vertical.

Recalling the derivation of the anelastic equations, the continuity equation before any approximation is

$$\frac{d}{dt}\ln(\,1+\frac{\rho'}{\rho_s}\,) + w\,\frac{\partial \ln\rho_s}{\partial z} + \frac{\partial u}{\partial x} + \frac{\partial v}{\partial y} \approx 0$$

where $\rho_s=\rho_s(z)$ is the density profile of the reference state while ρ' is the deviation from it. A similar approximation yields

$$\frac{d}{dt}\Big(\,\frac{\rho}{\rho_s}\,\Big) + w\,\frac{\partial \ln\rho_s}{\partial z} + \frac{\partial u}{\partial x} + \frac{\partial w}{\partial z} \approx 0$$

Scale analysis shows that the density perturbation can be neglected and it is this that renders the approximated set anelastic, i.e. sound proof. The contribution of perturbation density is neglected too in other equations except in the vertical momentum equation.

The above analysis illustrates that the approximations made to obtain the QNH system and the anelastic system are analogous, but they are not identical! The QNH system still supports Lamb waves because the horizontal motion of air (oscillation) is little affected by the approximations made in obtaining the system.

Chapter Two

Model Equations and Numerical Formulation of Dynamic Processes

2.1 Model equations

In chapter one a quasi-non-hydrostatic equation system in pressure or sigma-coordinates was established after Miller and White (1984). Equations (1.2.30), (1.2.31), (1.2.33), (1.2.34), (1.2.38), and (1.2.40) form a closed set for adiabatic and frictionless air motion. This equation set lays the foundation of our σ-coordinate numerical model and its general solution procedure was discussed in section 1.2.3. In this section we present a more complete equation set which includes the moist diabatic, frictional processes and the effect of earth rotation, and it is expressed in a form close to that of the numerical formulation of model. These equations are listed as follows:

$$\frac{\partial p_* u}{\partial t} = - \text{UFLUX} - p_* \frac{\partial \Phi'}{\partial x} + \sigma \frac{\partial p_*}{\partial x} \frac{\partial \Phi'}{\partial \sigma} + p_* fv + p_* D_u \qquad (2.1.1)$$

$$\frac{\partial p_* v}{\partial t} = - \text{VFLUX} - p_* fu + p_* D_v \qquad (2.1.2)$$

$$\frac{\partial p_* \tilde{w}}{\partial t} = - \text{WFLUX} + p_* S \frac{\partial \Phi'}{\partial \sigma} + p_* g \left[\frac{\theta'}{\theta_s} + 0.61 q_v' - q_c - q_r \right] + p_* D_w \qquad (2.1.3)$$

$$\frac{\partial p_* \theta'}{\partial t} = -\text{TFLUX} - p_* \theta_s N_s^2 \tilde{w} / g + p_* \dot{Q} / (C_p \Pi) + p_* M_\theta + p_* D_\theta \qquad (2.1.4)$$

$$\frac{\partial p_*}{\partial \tau} = -\int_0^1 \frac{\partial p_* u}{\partial x}\, d\sigma \qquad (2.1.5)$$

$$\frac{\partial p_* q_v}{\partial t} = -\,QVFLUX + p_* \left(M_{q_v} + D_{q_v} \right) \qquad (2.1.6)$$

$$\frac{\partial p_* q_c}{\partial t} = -\,QCFLUX + p_* \left(M_{q_c} + D_{q_c} \right) \qquad (2.1.7)$$

$$\frac{\partial p_* q_r}{\partial t} = -\,QRFLUX + p_* \left(M_{q_r} + D_{q_r} \right) \qquad (2.1.8)$$

$$\dot{\sigma} = -\,S\,\tilde{w} - \frac{\sigma}{p_*}\left[-\int_0^1 \frac{\partial p_* u}{\partial x}\, d\sigma + u \frac{\partial p_*}{\partial x} \right] \qquad (2.1.9)$$

$$p_* \Big[\frac{\partial^2 \Phi'}{\partial x^2} - \frac{2\sigma}{p_*} \frac{\partial p_*}{\partial x} \frac{\partial^2 \Phi'}{\partial x \partial \sigma} + \frac{\partial}{\partial \sigma}\Big(S^2 \frac{\partial \Phi'}{\partial \sigma} \Big) + \Big(\frac{\partial \ln p_*}{\partial x} \Big)^2 \frac{\partial}{\partial \sigma}\Big(\sigma^2 \frac{\partial \Phi'}{\partial \sigma} \Big)$$

$$- \frac{\sigma}{p_*} \frac{\partial^2 p_*}{\partial x^2} \frac{\partial \Phi'}{\partial \sigma} \Big] = F_\Phi \qquad (2.1.10)$$

Four additional equations are included in the above equation set. They are the equation for y-velocity v, and the equations for the conservation of water vapour, cloud water and rain water. Ice phase is not included in our model at the moment. Variables q_v, q_c and q_r are the specific humidity of water vapour, cloud water and rain water respectively. The momentum equations (2.1.1) to (2.1.3), the potential temperature equation (2.1.4) and those for the conservation of water quantities (2.1.6)-(2.1.8) are written in the flux form. Flux terms can be formally expressed as:

$$FFLUX = \frac{\partial p_* u\, \psi}{\partial x} + \frac{\partial p_* \dot{\sigma}\, \psi}{\partial \sigma}$$

where ψ denotes any of the quantities u, v, w, θ', q_v, q_c or q_r. Terms D_ψ in the equations represent subgrid-scale mixing processes and/or numerical diffusion. Hereafter these terms are usually referred to in general as the diffusion terms, the formulation of which will be given in next chapter. Terms M_ψ in the equations are the contributions of

cloud microphysics and their formulation will also be given later.

The equation of state of moist air is

$$p = \rho RT\,(1+0.61q_v)$$
$$= \rho RT_v \qquad (2.1.11)$$

where $T_v=T(1+0.61q_v)$ is the virtual temperature and ρ the density of the moist air, R is the gas constant for dry air. The potential temperature defined in terms of temperature will be referred to as the virtual potential temperature, which is

$$\theta_v = T_v/\Pi.$$

We split the specific humidity of water vapour also into two parts, one for the reference state and the other for the deviation from it.

$$q_v = q_{vs} + q_v',$$

and we require

$$p = \rho_s\, RT_s\,(\,1+0.61q_{vs}\,)$$
$$= \rho_s\, RT_{vs}\,. \qquad (2.1.12)$$

The hydrostatic relation that should be satisfied by the reference state is then

$$\frac{\partial \Phi_s}{\partial \sigma} + \frac{RT_{vs}\, p_*}{p} = 0 \quad . \qquad (2.1.13)$$

It can then be shown that

$$\frac{\theta_v'}{\theta_{vs}} \approx \frac{\theta'}{\theta_s} + 0.61\, q_v' \,,$$

and including the loading of liquid water (cloud water and rain water), the net buoyancy appears as the third term on the right hand side of the vertical momentum equation (2.1.3). In equation (2.1.4) the term $\dot{Q}$ represents the possible heat source or sink.

Apart from the prognostic equations for u, w, θ', p_*, q_v, q_c, and q_r there are two diagnostic equations for $\dot{\sigma}$ and Φ'. After the prognostic variables are predicted for the

new time, $\dot{\sigma}$ can be easily calculated from relation (2.1.9) and Φ' is solved for from the elliptic equation (2.1.10). This elliptic equation is obtained by directly applying a divergence operator on the momentum equations, i.e. by performing

$$\frac{\partial}{\partial x}\,[\ (2.1.1)\ ] + \frac{\partial}{\partial \sigma}\,[\ -\ S\ (2.1.3)\ ]$$

After a lengthy derivation we obtain equation (2.1.10), the right hand side of which is the forcing function F_Φ in the following,

$$\begin{aligned} p_* F_\Phi = &- \frac{\partial}{\partial x}\,(UFLUX - p_* D_u) + \frac{1}{p_*}\frac{\partial p_*}{\partial x}\,(1+\sigma\frac{\partial}{\partial \sigma})\,(UFLUX - p_* D_u) \\ &+ \frac{\partial}{\partial \sigma}\Big[S\,(WFLUX - p_* D_w)\Big] + (u+\sigma\frac{\partial u}{\partial \sigma})\Big(\frac{1}{p_*}\frac{\partial p_*}{\partial x} - \frac{\partial}{\partial x}\Big)\frac{\partial p_*}{\partial t} \\ &- p_* \frac{\partial}{\partial \sigma}\Big[gS\,(\frac{\theta'}{\theta_s} + 0.61 q_v' - q_c - q_v)\Big] \\ &+ p_t\Big[\,(p_*\dot{\sigma} + \sigma\frac{dp_*}{dt})/p^2 - \frac{1}{p_* p}\,(\frac{\partial p_*\dot{\sigma}}{\partial \sigma} + \sigma\frac{\partial u}{\partial \sigma}\frac{\partial p_*}{\partial x} + \frac{dp_*}{dt})\Big]\frac{\partial p_*}{\partial t} \\ &- \frac{\partial}{\partial t}\,(\frac{\partial p_*}{\partial t} + \frac{\partial p_* u}{\partial x} + \frac{\partial p_*\dot{\sigma}}{\partial \sigma})\,. \end{aligned} \qquad (2.1.14)$$

No further effort is made to simplify the above formulation, especially for the flux terms, as was done in equation (1.2.38). The current form is preferable because the advection or transport terms in the discretized form are better treated in the same way as they are in the momentum equations. The last term of F_Φ vanishes in a strict sense, however it is retained in the model formulation, because the continuity equation is not explicitly solved. The procedure after Harlow and Welch (1965) helps to improve the mass continuity in the model. If we define,

$$\delta D \equiv \frac{\partial p_*}{\partial t} + \frac{\partial p_* u}{\partial x} + \frac{\partial p_*\dot{\sigma}}{\partial \sigma}$$

i.e. the residual error in the mass continuity, and assume the current time is t (the time at

which F_φ is calculated), then

$$\left[\frac{\partial}{\partial t} \delta D \right]_t = \left[(\delta D)_{t+\Delta t} - (\delta D)_{t-\Delta t} \right] / (2\Delta t) .$$

Hoping that δD vanishes at the next time step, we demand that $(\delta D)_{t+\Delta t} = 0$, so that

$$\left[\frac{\partial}{\partial t} \delta D \right]_t = - (\delta D)_{t-\Delta t} / (2\Delta t) .$$

With term $\partial p_*/\partial t$ being substituted for using equation (2.1.8), the right hand side of the elliptic equation, F_Φ, can be calculated at the new time step. Given appropriate boundary conditions, it can then be solved. The details of the solution will be found in section 2.5 .

Suppose the terms representing the microphysics and subgrid scale processes are known or have functional relations with the other variables (as they are in our case), then equations (2.1.1) to (2.1.10) again form a closed set for the flow of moist air and it can be solved using a similar procedure to that discussed in section 1.2.3. The procedure is presented here in steps of the time integration:

1) *Initialize the model variables, for both the reference state and the perturbations. In the case when the initial fields are merely a function of p, iterations have to be performed in order to satisfy the given requirements (e.g. the hydrostatic balance).*
2) *Integrate equations (2.1.1), (2.1.2), (2.1.3) and (2.1.5) forward by one time step for* p_*^{n+1}, $(p_*u)^{n+1}$, $(p_*v)^{n+1}$, $(p_*w)^{n+1}$, *hence also* u^{n+1}, v^{n+1} *and* w^{n+1}, *where the superscripts denote the time levels.*
3) *As will be shown in the next chapter, the microphysics terms in equations (2.1.4) and (2.1.6)-(2.1.8) are implicitly dependent on the predicted quantities at the new time, therefore two steps have to be taken in the time integration of these equations, that is to:*
   a) *integrate equations (2.1.4) and (2.1.6) - (2.1.8) without the microphysics terms for a temporary value of each of the predicted*

variables,

b) adjust these temporary values according to the thermodynamic and microphysical constraints, to get the final updated values θ'^{n+1}, q_v^{n+1}, q_c^{n+1}, q_r^{n+1}. *This aspect of model will be described in next chapter.*

4) Calculate $\dot{\sigma}^{n+1}$,*the* σ*-coordinate vertical velocity, from equation (2.1.9).*

5) Compute the right hand side of equation (2.1.10) F_Φ *from the predicted values at time level n+1, and solve the elliptic equation for* Φ'^{n+1}.

6) Update the variables. When the reference state variables are dependent on the surface pressure, they should also be updated in principle.This effect is however minimal.

7) Finally go back to step 2), repeat cycle 2)-6).

In the rest of this chapter we will be concentrating on the numerical formulation and solution of the dynamic (dry) processes while leaving the microphysics and other processes to the next chapter.

2.2 Model grid and finite differencing

The model to be described is two-dimensional, hence we need only consider the grid in the vertical plane. Arakawa and Lamb (1977) studied a number of grids and showed the grid C, which is later on widely referred to as Arakawa C-grid, gave the best performance in terms of the internal gravity wave representation and some computational properties. We adapt this C-grid for use in the vertical plane. Fig. 2.1 illustrates a typical grid box and the staggering of grid variables.

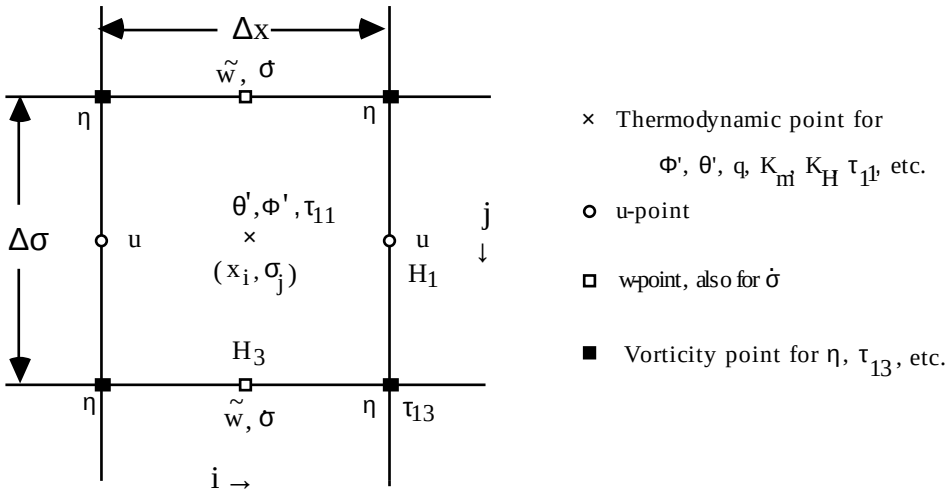

Fig. 2.1 Illustration of a typical grid box and the staggering of grid variables. The state variables θ', Φ', q, etc. locate at the centre of the box, and normal velocity components at the respective sides. The velocity in the third direction y is located at the same point as the temperature in two dimensional formulation.

The state variables θ', Φ' and variables of the water quantities are defined at the centre of the box, whereas the normal velocity components are defined on the corresponding sides of the box, i.e. u to the right and the left of the state variables and w, $\dot{\sigma}$ on the upper and lower sides of the box.The velocity in y-direction v coincides with θ'. Here i and j are indices of the grid vertices and Δx, $\Delta\sigma$ are constant grid intervals in x and σ directions respectively. The coordinates at the centre point of the box are

$$x_i = (i - 1/2)\,\Delta x, \quad \text{for } i = 0, NX + 1$$
$$\sigma_j = (j - 1/2)\,\Delta\sigma, \quad \text{for } j = 0, NS + 1 \qquad (2.2.1)$$

where $\Delta x = XL/NX$, $\Delta\sigma = 1/NS$, and XL is the horizontal length of the integration (physical) domain. u is defined at points $(i \pm 1/2, j)$ and w, $\dot{\sigma}$ at points $(i, j \pm 1/2)$, i.e.

$$u \equiv u(i \pm 1/2, j)$$
$$\tilde{w} \equiv \tilde{w}(i, j \pm 1/2) , \qquad (2.2.2)$$
$$\dot{\sigma} \equiv \dot{\sigma}(i, j \pm 1/2) ,$$

and

$$\psi = \psi(i, j)$$

where ψ represents any of the state variables θ', Φ', q_v, q_c, q_r and θ_s, Φ_s, and the y-velocity v. For the surface pressure,

$$p_{surf} , p_* \equiv p_{surf} , p_* (i) \qquad (2.2.3)$$

The second order centred difference scheme is used for all spatial finite differencing, except when the flux-corrected transport scheme is used, the latter is a weighted average of a lower order and a higher order scheme, in our case the first order upstream forward scheme and the second order leapfrog-centred difference scheme. In order to be able to apply the centred differencing also at the boundary, extra assumptions are made to extrapolate the variables to beyond the actual boundary.

Because implicit or semi-implicit time integration schemes are not practical for our equation system, we use the explicit leap-frog time differencing with respect to all but the diffusion terms, for which the explicit forward scheme is used for the diffusion terms because the leapfrog-forward scheme is absolutely unstable for parabolic equations.

We employ the Shuman type notation:

$$\begin{aligned} \delta_s \alpha &= (\alpha(s+\Delta s/2) - \alpha(s-\Delta s/2)) / \Delta s \\ \bar{\alpha}^{\,s} &= (\alpha(s+\Delta s/2) + \alpha(s-\Delta s/2)) / 2 \ , \end{aligned} \qquad (2.2.4)$$

from which we deduce that

$$\delta_s \bar{\alpha}^{\,s} = (\alpha(s+\Delta s) - \alpha(s-\Delta s)) / (2\Delta s)$$

where s could be any of x, σ or t .

The finite differencing of equations becomes straightforward based on the grid, and variables that are not available at required points due to grid staggering are linearly interpolated from their adjacent grid points. Using Shuman type notations the equations in finite difference approximations are:

$$\delta_t \overline{(\overline{p_*}^{x} u)}^{t} = - \text{UFLUX}^n - \overline{p_*}^{x} \delta_x \Phi' + \sigma \delta_x p_* \delta_\sigma \overline{\Phi'}^{x\sigma} + \overline{p_*}^{x} (D_u^{n-1} + f \bar{v}^{x}) \tag{2.2.5}$$

$$\delta_t \overline{(p_* v)}^{t} = - \text{VFLUX}^n - p_* f \bar{u}^{x} + p_* D_v^{n-1} \tag{2.2.6}$$

$$\delta_t \overline{(p_* w)}^{t} = - \text{WFLUX}^n + p_* \bar{S}^{\sigma} \delta_\sigma \Phi' + p_* g \left[\overline{\left(\frac{\theta'}{\theta_s}\right)}^{\sigma} + 0.61 \overline{q'_v}^{\sigma} - \overline{q_c}^{\sigma} - \overline{q_r}^{\sigma} \right] + p_* D_w^{n-1} \tag{2.2.7}$$

$$\delta_t \overline{(p_* \theta')}^{t} = - \text{TFLUX}^n - p_* \theta_s N_s^2 \overline{w}^{\sigma} / g + p_* M_\theta^n + p_* D_\theta^{n-1} + p_* \dot{Q} / (C_p \Pi) \tag{2.2.8}$$

$$\delta_t \overline{p_*}^{t} = - \sum_{j=1}^{NS} \delta_x (\overline{p_*}^{x} u) \Delta\sigma \tag{2.2.9}$$

$$\delta_t \overline{(p_* q)}^{t} = - \text{QFLUX}^n + p_* (M_q^n + D_q^{n-1}) \qquad (2.2.10),(2.2.11),(2.2.12)$$

$$\dot{\sigma} = - S w - \frac{\sigma}{p_*} \left[\bar{u}^{x\sigma} \delta_x p_* - \sum_{j=1}^{NS} \delta_x (\overline{p_*}^{x} u) \Delta\sigma \right] \tag{2.2.13}$$

where the water substance conservation equations are expressed in a single equation and q could be any of q_v, q_c, or q_r. In the above equations the 'tilde' over the approximated vertical velocity $\tilde{w}$ is omitted and will continue to be omitted for convenience of notation, since from now on we will be mostly looking at vertical velocity of the QNH system.

The right hand side of the elliptic equation F_Φ given by equation (2.1.14) can be differenced in a similarly straightforward fashion, and will therefore not be given here. One only has to note that the flux or advection term UFLUX or WFLUX is treated as a whole when being differenced and they are defined at the same point as u or w. The formulations of the advection terms for the momentum in flux form are

$$\mathrm{UFLUX}^n = \delta_x\left(\overline{\overline{p_*}^{\,x}}\, u\, u\right) + \delta_\sigma\left(\dot{\sigma}\overline{p_*}^{\,x}\,\bar{u}^{\sigma}\right)$$

$$\mathrm{VFLUX}^n = \delta_x\left(\overline{p_*}^{\,x}\, u\, \bar{v}^{x}\right) + \delta_\sigma\left(p_*\,\dot{\sigma}\,\bar{v}^{\sigma}\right) \qquad (2.2.14)$$

$$\mathrm{WFLUX}^n = \delta_x\left(\overline{p_*}^{\,x}\,\bar{u}^{\sigma}\,\overline{w}^{x}\right) + \delta_\sigma\left(p_*\,\dot{\sigma}\,\overline{w}^{\sigma}\right)$$

and the potential temperature advection is

$$\mathrm{TFLUX}^n = \delta_x\left(\overline{p_*}^{\,x}\, u\,\overline{\theta'}^{\,x}\right) + \delta_\sigma\left(p_*\,\dot{\sigma}\,\overline{\theta'}^{\,\sigma}\right)\ . \qquad (2.2.15)$$

A general form for the advection of water substances is

$$\mathrm{QFLUX}^n = \delta_x\left(\overline{p_*}^{\,x}\, u\,\bar{q}^{x}\right) + \delta_\sigma\left(p_*\,\dot{\sigma}\,\bar{q}^{\sigma}\right) \qquad (2.2.16)$$

which represents terms QVFLUX^n, QCFLUX^n or QRFLUX^n for water vapour, cloud water and rainwater respectively. In the above the thermodynamic and water quantity conservation equations are all differenced using the leapfrog-centred scheme. When the flux-corrected transport scheme is used to advect these scalar quantities, TFLUX and QFLUX would then be the corrected fluxes and Eqs. (2.2.8) and (2.2.10)-(2.2.12) would be replaced by the corresponding equations to be given in next chapter.

Lilly (1964) showed that the advection terms formulated as above conserve the quadratic quantities as well as the quantities being advected. Therefore the kinetic energy and the potential temperature variance will be conserved in the advective process. This conservation property rules out any spurious generation of energy and momentum and considerably suppresses the non-linear instability due to wave spectrum aliasing. (Haltiner and Williams, 1980). Numerical tests show that the model thus formulated is free of non-linear instability even without any numerical diffusion. The numerical formulations of the microphysics and diffusion terms in the above equations will be given in the next chapter.

2.3 Time filtering and stability requirements

It is commonly known that the solution of an advection equation obtained using the leapfrog finite differencing scheme contains two modes, one is the physical mode and the other is referred to as the computational mode. The latter arises from using a second order difference equation to approximate a first order equation. The computational mode shows itself as a two time step oscillation and travels in the opposite direction to the physical mode (Haltiner and Williams, 1980). Successive use of the leapfrog scheme will therefore cause time splitting i.e. the growing of two time step waves in the solution. This difficulty can be tackled by periodic use of another scheme, e.g. either the Euler backward or the Matsuno scheme, between a certain number of leapfrog steps. In our model it is required that the time differencing of the momentum equations and that employed in deriving the finite difference analogue of the diagnostic equations for Φ' should be consistent. Therefore we avoid using the above-mentioned technique, whereas we employ the Robert time filter (Robert 1966), which was discussed in detail by Asselin (1972), with a small parameter at every time step of integration in order to achieve a smooth filtering effect.

Assume ψ^{n-1} and ψ^{n} represent function ψ at time levels n-1 and n, where ψ^{n-1} has been averaged, i.e. has been applied with the time filter. Then from the prediction equation, ψ at next time level is obtained,

$$\psi^{n+1} = \bar{\psi}^{n-1} + 2\Delta t \left(\frac{\partial \psi}{\partial t} \right)^{n} .$$

The averaged value of ψ^{n} is then computed as follows,

$$\bar{\psi}^{n} = \psi^{n} + \alpha \left(\psi^{n+1} - 2\psi^{n} + \bar{\psi}^{n-1} \right) \qquad (2.3.1)$$

At the time of updating the variables, ψ^{n} is stored in place of ψ^{n-1} and ψ^{n+1} in place of ψ^{n} and the integration procedure is repeated.

The time filtering has an effect on the computational stability criterion; increasing α requires progressively smaller Δt, at the same time, repeated use of the time filter with relatively large α will strongly damp high frequency physical waves, therefore a small

value of α is preferable. A value of 0.05 is currently used in the model and the filter is applied to variables explicitly predicted by the leapfrog scheme.

The leapfrog scheme is conditionally stable for advection equations, but is absolutely unstable for parabolic equations. The forward time integration scheme instead is used for the diffusion terms. Formally the integration equations can be written as,

$$\psi^{n+1} = \psi^{n-1} + 2\Delta t \, [\, D_{\psi}^{n-1} + (\text{ other terms })^{n} \,]$$

where D_{ψ} represents the diffusion term.

Assume a simple formulation of a diffusion term in one dimension,

$$D_{\psi} = K \frac{\partial^2 \psi}{\partial x^2}$$

and use the centred scheme for the spatial differencing, the stability criterion required by the diffusion process is then (Pielke, 1984, page 285),

$$K \frac{2 \, \Delta t}{(\Delta x)^2} < \frac{1}{4} \, , \qquad (2.3.2)$$

note here the actual time step used for the diffusion term is $2\Delta t$. Despite the above requirement, the limitation on the length of time step by the diffusion process is generally much weaker than that by advection processes.

For an advection equation, the computational stability of the leapfrog scheme is subject to the well known Courant-Friedrichs-Levy (CFL) condition, which is

$$\left| \frac{C \, \Delta t}{\Delta x} \right| < 1 \, ,$$

where C is the speed of advective flow or the phase speed of propagating wave disturbances. This condition is modified when the wave equations are represented on a staggered grid. Suppose one dimensional gravity waves are governed by equations

$$\frac{\partial u}{\partial t} + U \frac{\partial u}{\partial x} + \frac{\partial \Phi}{\partial x} = 0$$

$$\Phi \frac{\partial u}{\partial x} + \frac{\partial \Phi}{\partial t} + U \frac{\partial \Phi}{\partial x} = 0 \qquad (2.3.3)$$

where Φ is the geopotential height, $\Phi^{1/2}$ gives the phase speed of the gravity waves. Haltiner and Williams (1980, page 142) showed that when the grid is staggered with u and Φ on alternate grid points, the stability criterion is

$$\left| \sin (k\Delta x/2) (U \cos(k\Delta x) \pm \Phi^{1/2}) (\Delta t / \Delta x) \right| \leq 1/2$$

or more strictly, $$\left| (U \pm \Phi^{1/2}) (\Delta t / \Delta x) \right| \leq 1/2 \qquad (2.3.4)$$

where Δx is the grid spacing between two points of the same variable. This condition implies the maximum time step is halved for the staggered case than the unstaggered, or alternatively the effective grid spacing is $\Delta x/2$ for the CFL condition of the gravity wave equations.

As was discussed in the previous chapter the fastest propagating wave in the QNH system are the Lamb waves. The stability condition for Lamb waves is similar to that for gravity waves; it is the same condition (2.3.4) except the gravity wave phase speed $\Phi^{1/2}$ there is replaced by C_L, the phase speed of Lamb wave. This point can be illustrated by considering a simple system of equations in height coordinates linearized around a reference state of no motion and of constant density ρ_0. They are

$$\frac{\partial u}{\partial t} + \frac{\partial \Phi}{\partial x} = 0 \qquad (2.3.5)$$

$$\frac{\partial \rho}{\partial t} + \frac{\partial u}{\partial x} + \frac{\partial w}{\partial z} = 0 \qquad (2.3.6)$$

$$\frac{\partial w}{\partial t} + \frac{\partial \Phi}{\partial z} + \rho g = 0 \qquad (2.3.7)$$

$$\frac{\partial \Phi}{\partial t} - w g = C^2 \frac{\partial \rho}{\partial t} \qquad (2.3.8)$$

where $\Phi \equiv p'/\rho_0$, $\rho \equiv \rho'/\rho_0$ and $C^2 = \gamma RT_0$, the others follow the convention.

Eliminating ρ from (2.3.6), (2.3.7) and (2.3.8), we obtain

$$\frac{\partial \Phi}{\partial t} - wg + C^2 \left(\frac{\partial u}{\partial x} + \frac{\partial w}{\partial z} \right) = 0$$

$$\left(\frac{\partial}{\partial t^2} - \frac{g^2}{C^2} \right) w + \frac{\partial}{\partial t} \left(\frac{\partial \Phi}{\partial x} + \frac{g}{C^2} \right) \Phi = 0$$

Since we are interested in Lamb waves that have no vertical motion, we set

$$w \equiv 0,$$

and obtain an equation set for Lamb waves,

$$\frac{\partial u}{\partial t} + \frac{\partial \Phi}{\partial x} = 0 \qquad (2.3.9)$$

$$\frac{\partial \Phi}{\partial t} + C^2 \frac{\partial u}{\partial x} = 0 \qquad (2.3.10)$$

$$\frac{\partial}{\partial t} \left(\frac{\partial \Phi}{\partial z} + \frac{g}{C^2} \right) = 0 \qquad (2.3.11)$$

From equation (2.3.11) we obtain the vertical structure distinguishing the Lamb waves,

$$\Phi(z) = \exp(- \Gamma z), \quad \Gamma \equiv g/C^2$$

It is clear that equations (2.3.9) and (2.3.10), which govern the horizontal structure of Lamb wave solution, are analogous to equations in (2.3.3) for gravity waves. The computational stability criterion is then equivalent to (2.3.4), that is

$$\left| (U \pm C_L) \Delta t / \Delta x \right| \leq 1/2 \qquad (2.3.12)$$

where U is a background advective flow speed if not zero.

The above analyses show the maximum time step that can be used is the one that satisfies conditions (2.3.2), (2.3.4) and (2.3.12).

2.4 Boundary conditions for the prognostic equations

Mesoscale models all have a limited domain, and therefore have to be artificially enclosed by boundaries. The values of variables on these boundaries, i.e. the boundary conditions, are required in order to solve the model equations in time. In our model only the lower boundary is physical while the top and lateral boundaries are required for purely computational reasons. The boundary conditions best suited to the physical problems that this model is designed to deal with will be discussed separately in the following sub-sections, and separately for the lateral boundary and the top and bottom boundaries.

2.4.1 Lateral boundary conditions

The boundary conditions on the lateral sides of a numerical model are usually the most difficult to specify, because it is frequently required that the disturbance propagate freely in and out of the boundary without generating spurious wave motions which would seriously contaminate the interior solutions. A solution to this is to remove the boundary as far as possible from the area of interest so that their fields are little affected by the erroneous disturbances reflected back from the boundary. Nevertheless this solution is obviously unnecessarily expensive and is often limited by computational resources available.

Several types of lateral boundary conditions are possible. The first is the specified inflow, gradient outflow condition, in which the value of dependent variables at the inflow boundary (defined in terms of the flow direction) are assumed unaffected by the downstream disturbances. The values at the outflow boundary are simply those passed on from the immediately interior grid points. This procedure, as we can expect, is incapable of correctly handling the disturbances propagating to and from the boundaries. Another type of condition is the periodic boundary condition, which implies that disturbances that propagate out of the model domain at one boundary will enter the domain again at the other boundary. This assumption is only acceptable for certain situations. The most

commonly used is the type usually referred to as the radiative boundary condition (RBC), which is designed to minimize the reflection of outward propagating disturbances back into the model domain. The radiative boundary conditions due to Orlanski (1976) are implemented in our model. Finally the sponge type boundary conditions are also often used, incorporating near the lateral boundary a region of enhanced filtering to damp out the disturbances propagating towards the boundary; in other words, to absorb the wavy disturbances that get into the sponge zone. Such an effect can be achieved either by increasing the coefficient of diffusion or by applying a Rayleigh friction type damping with a gradually increased coefficient. The former is effective in removing short scale waviness and the latter tends to relax the variable field towards a given state.

a) The radiative boundary conditions of Orlanski

The radiative boundary condition of Orlanski is based on the 'Sommerfeld' boundary condition. Assume the disturbance propagation is described by a simple one dimensional wave equation

$$\frac{\partial \psi}{\partial t} + c \frac{\partial \psi}{\partial x} = 0 \qquad (2.3.13)$$

where ψ could be any variables and c is a velocity which includes both wave propagation and advection. Several procedures have been introduced to implement this type of condition, including those of Orlanski (1976), Klemp and Lilly (1978). The following discussions closely follow Orlanski.

Without losing generality we consider the right boundary. Equation (2.3.13) is approximated by the finite difference equation

$$\psi_b^{n+1} = \psi_b^{n-1} - c \left(\psi_b^{n+1} + \psi_b^{n-1} - 2\psi_{b-1}^{n} \right) \Delta t / \Delta x \qquad (2.3.14)$$

where n denotes the time level and b the index of grid point at the boundary. Equation (2.3.14) employs the leapfrog scheme in time and one-sided difference in space with a time average on the boundary value of ψ to damp out the computational mode. The key of the problem is the proper estimation of speed c. If equation (2.3.14) is applied at the

immediately interior grid point b-1, for the previous time step, then

$$c = \frac{\psi_{b-1}^{n-2} - \psi_{b-1}^{n}}{\psi_{b-1}^{n} + \psi_{b-1}^{n-2} - 2\,\psi_{b-2}^{n-1}} \; \frac{\Delta x}{\Delta t} \qquad (2.3.15)$$

this value of phase speed is extrapolated to the current time level n and approximates the phase speed at the boundary b. For the right boundary, the inflow is defined as $c \leq 0$, for which the value of dependent variable ψ at the boundary is kept unchanged, i.e. $c = 0$ for prediction equation (2.3.14). When $c > 0$ the boundary is defined as outflow boundary, at which the boundary condition extracts information from the interior grid points. Since a too large value of c can results from the small gradient in ψ according to equation (2.3.15) and will cause computational instability, an upper bound is imposed on its value following Orlanski (1976). As a result the formula of c becomes

$$\hat{c} = \mathrm{Min}\left[\, \Delta x/\Delta t \,,\, \mathrm{Max}(\, 0 \,,\, c \,) \,\right]$$

and

$$\hat{c} = \mathrm{Max}\left[\, -\Delta x/\Delta t \,,\, \mathrm{Min}(\, 0 \,,\, c \,) \,\right] \qquad (2.3.16)$$

for the right and the left boundary respectively, with the c inside the brackets given by equation (2.3.15). Equation (2.3.14) is then the prediction equation for variable ψ at the boundary, with $\hat{c}$ calculated from (2.3.16).

A number of modifications are possible to the above procedure. For example it is sometime better to estimate $\hat{c}$ at further interior grid points where the solution is less sensitive the boundary condition specified. Klemp and Lilly (1978) simply choose $\hat{c}$ as a constant, with the value of a dominant internal gravity wave. Miller and Thorpe (1981) proposed possible improvements to the above procedure and tested a similar procedure using the upstream-forward scheme. We will not go into details here.

b) Implementation of radiative boundary conditions in the model

In this model, the radiative boundary condition is applied, in a similar way to Miller

and Thorpe (1981), to the normal velocity component u, y-velocity v, surface pressure p_* and potential temperature θ'. It is also applied to the variables of water substance, although this is not essential. Simple boundary conditions which, say, specify the value or gradient at inflow boundary and use one-sided advection at outflow boundary may be good enough and may have a better control over the moisture fields at the boundary. The vertical velocity is calculated from the continuity equation with u being known already. In order to conserve the total mass inside the model domain, the mass fluxes through two lateral boundaries are kept fixed with an initial value or made equal to each other. To do this the normal velocity determined by the radiative boundary conditions are adjusted accordingly: a constant velocity difference is added at all levels to the original values. There may be better ways of maintaining the total mass. A sponge type boundary zone may be included into the model with Newtonian type damping to relax the velocity profile near the boundary back to an initial profile. In this way both the mass flux and the velocity profile can be maintained.

Figure 2.2 illustrates the arrangement of variables in horizontal relative to, for example, the left boundary.

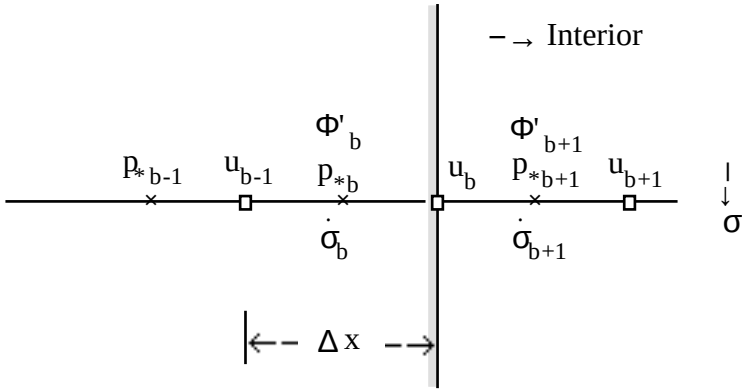

Left boundary

Fig. 2.2 Arrangement of variables relative to the physical boundary. The boundary for u is at the physical boundary but that for p_*, Φ', $\dot{\sigma}$ etc. is half a grid outside.

The boundary for normal velocity u coincides with the physical boundary while the boundary for state variable such as p_*, Φ' and $\dot{\sigma}$ is half a grid interval outside. As we can

see later the forcing function of the elliptic equation (2.1.14) is calculated up to grid point i=b+1 (i.e. half a grid inside the physical boundary), this requires the value of UFLUX at the u boundary. It is possible to calculate UFLUX using one-sided differencing but we decide to retain the standard formulation of centred differencing while introducing an extra grid point i=b-1 for u, at which u is also predicted by the radiative boundary condition (RBC). Similarly $p_{*,b-1}$ at the extra grid point is also calculated from the RBC.

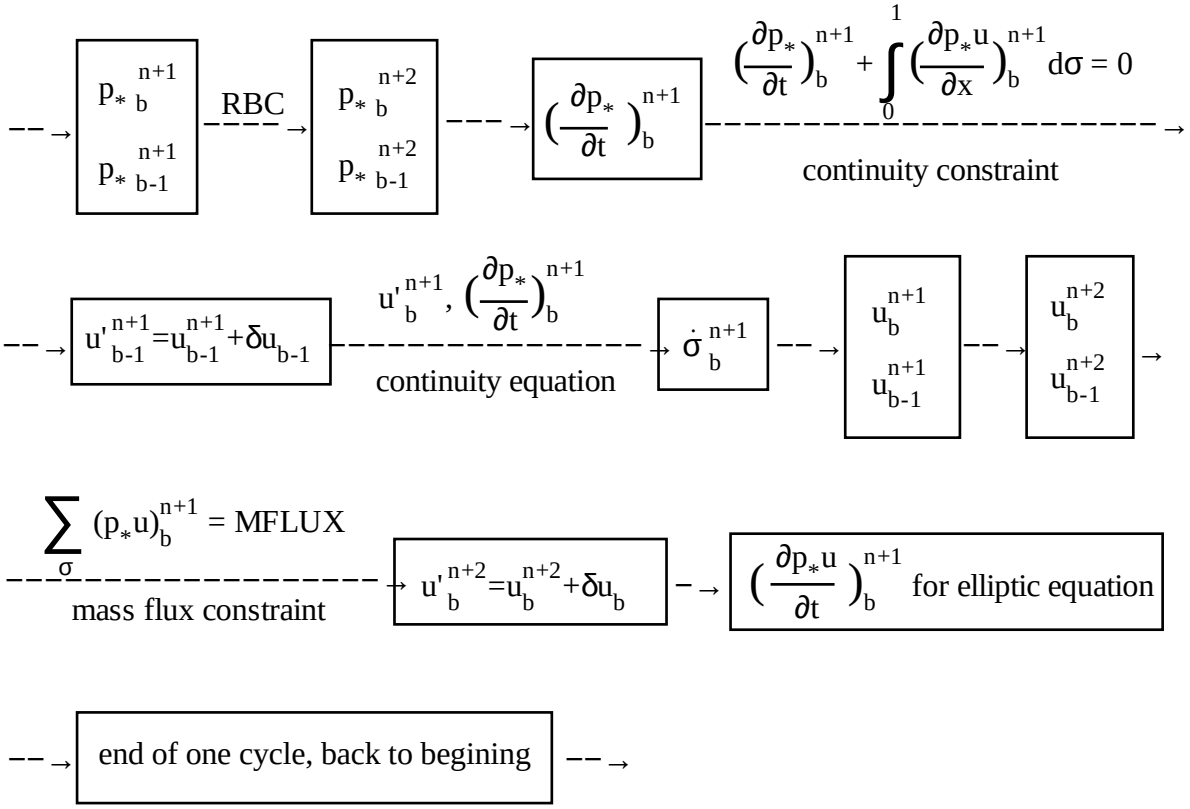

Fig. 2.3 The flow chart for the implementation of lateral boundary conditions. First the RBC is used to predict the surface pressure at and outside the physical boundary, therefore tendency of p_* is obtained. u at b-1 is then adjusted under continuity constraints. Next the vertical velocity at the boundary is diagnosed. RBC is again used to predict u at and outside the boundary, the former is adjusted immediately subject to the constraint.on the mass flux through the boundary. The tendency of p_*u can then be obtained for the elliptic equation and one cycle is ended.

The procedure for the implementation of boundary conditions is illustrated in Figure 2.3. This procedure is implemented when the values of dependent variables in the interior

have been obtained for time level n+1 from time integration of the prognostic equations and variables at the boundary have also been predicted by the R.B.C. at this time level. The vertical velocity is then diagnosed and the R.B.C. used to predict p_* and u for next time level n+2. The sensitivity tests in chapter four concerning mountain gravity wave problems show the lateral boundaries thereby formulated are reasonably transparent to wave disturbances and the interior solution is little affected by the boundary.

2.4.2 Top and bottom boundary conditions

The depth of the Earth atmosphere is large, whereas the model atmosphere has to be bounded at certain level. For mesoscale models, the domain seldom goes beyond the lower stratosphere. In some cases only the lower troposphere or even the planetary boundary layer is modeled. Therefore an artificial boundary is again needed at the top of the model. The top boundary of our model is a surface of constant pressure $p=p_t$, or a zero sigma surface ($\sigma=0$) in sigma-coordinates. The vertical velocity vanishes there by definition, but the height of the boundary varies. External gravity waves are supported at this free surface, but they are the 'deep water' approximation to the external waves, are therefore slower than the 'shallow water' waves (Miller 1974). The bottom boundary of the model is at $p=p_{surf}$, i.e. $\sigma=1$, which is a physical boundary. p_{surf} is the pressure at the ground surface z=h(x). Again due to staggering of the grid, some grid levels are located beneath the bottom or above the upper boundary. In Fig. 2.4 is a schema of the model domain with relative positions of grid points at the boundaries.

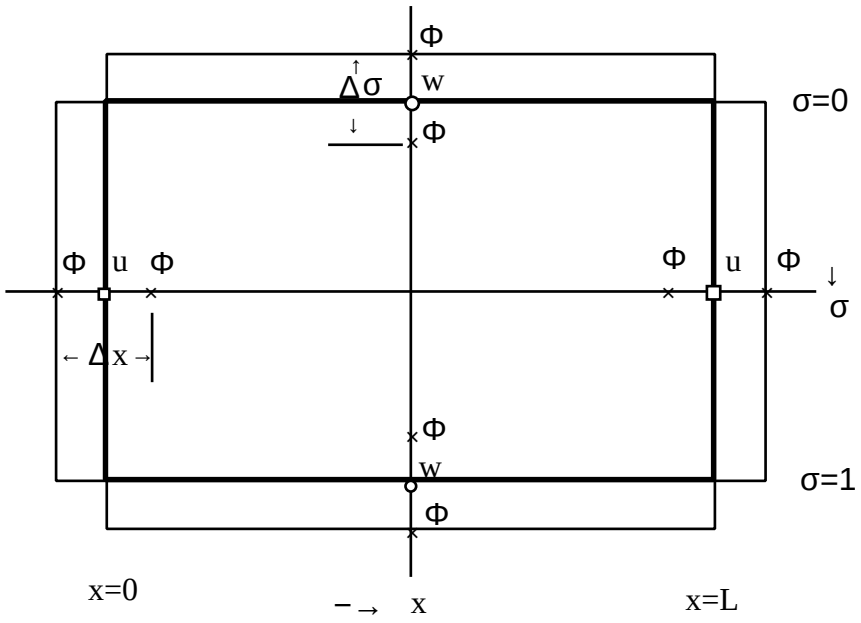

Fig. 2.4 The variable arrangement at the boundary. The bold box represents the boundary of physical domain. The u-points are at the lateral boundaries and w-points at the top and bottom boundary. At top and bottom boundaries the u and Φ-points are half a grid interval outside and so are the w and Φ-points at the lateral boundaries.

Free-slip boundary conditions are assumed at the top and bottom of the domain, i.e. the normal gradient of tangential velocity vanishes at the boundary. Based on the definition of velocity components and the above assumption, we can write the conditions as,

$$\begin{aligned} &\text{At } \sigma=0, \quad \dot{\sigma} = w = 0 \text{ and } \partial u/\partial\sigma = 0 \\ &\text{At } \sigma=1, \quad \dot{\sigma}=0, \quad w = -\frac{dp_*}{dt} \Big/ (p_* S) \quad \text{and } \partial u/\partial\sigma = 0 \ . \end{aligned} \tag{2.4.1}$$

In discrete form, they are

$$\begin{aligned} &\dot{\sigma}\Big|_{\sigma=0} = w\Big|_{\sigma=0} = 0, \quad u\Big|_{\sigma=-\Delta\sigma/2} = u\Big|_{\sigma=\Delta\sigma/2} \\ &\dot{\sigma}\Big|_{\sigma=1} = 0, \quad w\Big|_{\sigma=1} = -\left(\frac{1}{p_* S}\frac{dp_*}{dt}\right)_{\sigma=1}, \quad u\Big|_{\sigma=1+\Delta\sigma/2} = u\Big|_{\sigma=1-\Delta\sigma/2} \end{aligned} \tag{2.4.2}$$

At $\sigma=-\Delta\sigma$ and $\sigma=1+\Delta\sigma$, $\dot{\sigma}$ is diagnosed from the continuity equation and w from its definition given the value of $\dot{\sigma}$. This procedure will reduce to the mirror type symmetry

boundary conditions when the pressure at the boundary is constant.

For the potential temperature equation, we assume the zero gradient boundary (non-conductive) condition, i.e.

$$\frac{\partial \theta'}{\partial \sigma} = 0 \quad \text{at } \sigma=1 \quad \text{or} \quad \theta' \Big|_{\sigma=1+\Delta\sigma/2} = \theta' \Big|_{\sigma=1-\Delta\sigma/2}$$

$$\frac{\partial \theta'}{\partial \sigma} = 0 \quad \text{at } \sigma=0 \quad \text{or} \quad \theta' \Big|_{\sigma=-\Delta\sigma/2} = \theta' \Big|_{\sigma=\Delta\sigma/2} , \qquad (2.4.3)$$

but conditions as such are relevant only in the calculations of the turbulent heat fluxes through the boundaries, because the advective flux through the boundary would always vanish where $\dot{\sigma}=0$. For particular applications, the turbulent heat fluxes will have to be specified or parameterized using a selected scheme. Similarly the moisture fluxes at the ground are also set to zero for our experiments. The momentum drag (wind stress) at a flat ground surface is set to zero, but again a formula for it can be readily incorporated where required.

The boundary conditions of the elliptic equation for Φ' at both the lateral and the top and bottom boundaries need careful consideration, these will be found in next section, together with the method of solution for the equation.

2.5 Solution of the elliptic equation for Φ'

2.5.1 Methods of solution for elliptic equations

Elliptic partial differential equations frequently arise in geophysical fluid problems in connection with steady state solutions or diagnostic equations. Written in a general form, an elliptic equation is

$$G(P) = F$$

where G is an elliptic operator, F is a known forcing function and P is the dependent variable to be solved for. To solve this equation over a domain, either (1) the dependent

variable P, (2) its normal derivative, or (3) a combination of both must be known on the boundary enclosing the domain. These three boundary specifications are referred to as respectively the Dirichlet, Neumann and mixed condition.

A simple elliptic equation is a Poisson equation defined over a rectangular region

$$L(P) = F$$

where L is a 2-D or 3-D Laplacian operator ^{2}. A number of efficient direct methods have been introduced to solve discretized Poisson equations (e.g. Buzbee et al., 1970; Sweet, 1977; Swarstranber, 1977). These 'fast Poisson solvers' are based on cyclic reduction, matrix decomposition, or a combination of both; and many make use of the Fast Fourier Transform (FFT) algorithm. Although highly efficient for Poisson equations, they usually can not be extended to more complicated problems, such as equation (2.1.10) to be used here, in which the elliptic operator involves cross derivatives and variable coefficients. Iteration methods such as SOR (Successive Over Relaxation) and ADI (Alternating Direction Implicit) are generally more flexible and simple to use, however they suffer from progressively slow convergence with the increase in resolution and the increase in the number of data points that are involved in the discretized operator. Recognizing that the Fourier modes responsible for the slow convergence of a simple, say Gauss-Seidal relaxation, are the lowest wave-number modes; these modes could be adequately approximated on a coarser grid with much less work, the multi-grid methods (see review by Futton et al. 1986) are introduced, which use multiple overlapping grids of varying mesh sizes with cycling between them to accelerate the convergence of the overall relaxation. While able to solve more complicated problems and efficient in terms of operation counts, the optimal implementation of the multi-grid method is rather complex. Some general software has to be available at least.

The elliptic equation (equation (2.1.10)) in our model is complicated in its form, however a close look at it reveals that not all terms on the left hand side are equally important. The coefficients of all but two terms are proportional to the fractional variations in the surface pressure or accurately the pressure difference between the ground surface

and the top. Since generally

$$\frac{\delta p_*}{p_*} = O\left(\frac{\Delta p}{p}\right) << 1,$$

only terms

$$\frac{\partial^2 \Phi'}{\partial x^2} \quad \text{and} \quad \frac{\partial}{\partial \sigma}\left(S^2 \frac{\partial \Phi'}{\partial \sigma}\right)$$

are dominant! The other terms are present due to the variation in the surface pressure. Recognizing this fact we chose to move the less important terms to the right hand side of the equation and treat them explicitly. Then we will be solving a nearly standard Poisson equation. An acceptable accuracy can be reached by performing several iterations, each time the terms on the right hand side are updated using new value of Φ'. Furthermore noting the coefficient S^2 is only weakly dependent on x, again through the variation of pressure in horizontal, we approximate it using its horizontal average performed at constant σ. The averaged coefficient is now a function of σ only. Based on the above ideas equation (2.1.10) is formulated as

$$\left[\frac{\partial^2}{\partial x^2} + \frac{\partial}{\partial \sigma}\left(\overline{S^2}\,\frac{\partial}{\partial \sigma}\right)\right] \Phi^{p+1} = L_1(\Phi^p) + F_\Phi \qquad (2.5.1)$$

where L_1 is an operator representing terms 2, 4 and 5 of the left hand side of equation (2.1.10), the superscript 'p' denotes the p_{th} iteration. The prime of Φ' is omitted here and in the rest of this subsection for convenience of notation.

If we further write

$$\Phi^{p+1} = \Phi^p + \Delta\Phi^{p+1} \ , \qquad (2.5.2)$$

equation (2.5.1) then becomes

$$\left[\frac{\partial^2}{\partial x^2} + \frac{\partial}{\partial \sigma}\left(\overline{S^2}\,\frac{\partial}{\partial \sigma}\right)\right] \Delta\Phi^{p+1} = R^p \qquad (2.5.3)$$

where

$$R^p \equiv - L(\Phi^p) + F_\Phi$$

is the residual function of the elliptic equation with the p_{th} approximation of Φ, and L is the unapproximated full operator as in equation (2.1.10). It is clear that at the limit where the iteration converges, $\Delta\Phi^{p+1}$ and therefore R^p vanishes, then Φ^p is the true solution to elliptic equation (2.1.10). We will refer to (2.5.3) as the correction equation for Φ'.

Now assume the boundary condition is

$$L_B (\Phi) = F_B \qquad (2.5.4)$$

where L_B is a linear operator and F_B a linear function of Φ defined on the boundary.

If the first guess Φ^p (starting from p=0) satisfies the above condition, i.e

$$L_B (\Phi^p) = F_B$$

then by demanding that Φ^{p+1} satisfies the same condition we obtain a homogeneous condition for $\Delta\Phi^{p+1}$,

$$L_B (\Delta\Phi^{p+1}) = 0 \qquad (2.5.5)$$

The problem is then to solve equation (2.5.3) with a homogeneous boundary condition given by (2.5.5). Such an equation can be efficiently solved by a direct method making use of Fast Fourier Transform (FFT) and Guassian elimination algorithms. We will see more details on the solution method in section 2.5.3, while in the next section we will give the precise formulation of the boundary condition that is formally given by (2.5.4).

Finally the criterion of convergence of iterations is

$$\sum_{i,j} \left| \Delta\Phi^{p+1}_{i,j} \right| / \sum_{i,j} \left| \Phi^p_{i,j} \right| < \varepsilon$$

with $\varepsilon = 10^{-6}$ being used in the model. In the tests with dry convections, on average 2 iterations are sufficient without topography and a few more are otherwise required depending on the aspect ratio of the orography.

2.5.2 Boundary conditions for the equation for Φ'

At the lateral boundaries, the normal gradient of Φ' can be deduced from the horizontal momentum equation. Re-formulating equation (2.1.1) gives

$$\frac{\partial \Phi'}{\partial x} = -\frac{1}{p_*}\frac{\partial p_* u}{\partial t} - \mathrm{UFLUX}/p_* + \frac{\sigma}{p_*}\frac{\partial p_*}{\partial x}\frac{\partial \Phi'}{\partial \sigma} + fv + D_u \qquad (2.5.6)$$

This equation is applied at the left and right boundary. The first term on the R.H.S at the current time level is given in the boundary calculations shown in the flow chart in Fig. 2.3, the second and the fourth term can also be readily calculated. The contribution of the third term is relatively small and so for the same reason as before, this term is treated explicitly using the value of Φ' of previous iteration. With the right hand side known the conditions on the lateral boundaries are expressed as

$$\frac{\partial \Phi'}{\partial x}\Big|_B = F_B^{p-1}(\sigma) \qquad (2.5.7)$$

In discrete form, it becomes

$$\Phi'^{\,p+1}\Big|_{x=-\Delta x/2} = \Phi'^{\,p+1}\Big|_{x=\Delta x/2} - \Delta x\, F_B^p\Big|_{x=0}$$

$$\Phi'^{\,p+1}\Big|_{x=XL+\Delta x/2} = \Phi'^{\,p+1}\Big|_{x=XL-\Delta x/2} + \Delta x\, F_B^p\Big|_{x=XL} \qquad (2.5.8)$$

Obviously these are all Neumann boundary conditions.

On the top boundary, vertical velocity vanishes, we have from the vertical momentum equation (2.1.3) that

$$\frac{\partial \Phi'}{\partial \sigma}\Big|_{\sigma=0} = F_B\Big|_{\sigma=0} \qquad (2.5.9)$$

where

$$F_B\Big|_{\sigma=0} = \left\{ \left[\frac{\partial p_* \dot{\sigma} w}{\partial \sigma} - p_* g \left(\frac{\theta'}{\theta_s} + 0.61 q_v' - q_c - q_r \right) - p_* D_u \right] / (p_* S) \right\}_{\sigma=0}$$

and at the current time level it is readily calculated. Again expressed in a discrete form Eq.(2.5.9) becomes

$$\Phi'^{\,p+1}\Big|_{\sigma=-\Delta\sigma/2} = \Phi'^{\,p+1}\Big|_{\sigma=\Delta\sigma/2} - \Delta\sigma\, F_B\Big|_{\sigma=0} \qquad (2.5.10)$$

The bottom boundary is the only physical boundary of the model, where the geopotential height is related to the surface topography. Since the lower boundary of the model is the ground surface, which has a topography profile

$$z = h(x)$$

we have

$$\Phi\Big|_{\sigma=1} = \Phi_s\Big|_{p=p_{surf}} + \Phi'\Big|_{\sigma=1} = g\,h \ . \qquad (2.5.11)$$

However, the geopotential height of the reference state Φ_s is defined as a function of pressure p, its value at σ=1 has to be found. To do so, we notice that the reference state variables satisfy relations (1.2.36) and (1.2.37) in section 1.2.3. By substituting equation (1.2.37) into (1.2.36) and differentiating the resulting equation with respect to x at constant σ=1, we obtain

$$\frac{\partial \Phi_s}{\partial x^2}\Big|_{\sigma=1} = -\frac{\partial}{\partial x}\left(\frac{RT_s}{p_{surf}}\frac{\partial p_*}{\partial x}\right) \ . \qquad (2.5.12)$$

Assume Φ_s=0 at a reference pressure p=p_0, then from the hydrostatic relation

$$\Phi_s(\,p=p_{surf}\,) = -R\int_{p_0}^{p_{surf}} \frac{T_s}{p_*}\,dp \qquad (2.5.13)$$

and suppose (2.5.13) can be evaluated at boundary points x=0 and x=XL, then we have

$$\Phi_s\Big|_{\sigma=1,\,x=0} = \Phi_s[\,p_{surf}(0)\,]$$

$$\Phi_s\Big|_{\sigma=1,\,x=XL} = \Phi_s[\,p_{surf}(XL)\,] \ . \qquad (2.5.14)$$

The discrete approximation to equation (2.5.12) is a tridiagonal linear equation set,

and can be directly solved using Gaussian elimination, given the boundary values as in equation (2.5.12). In three dimensional case the corresponding equation is then a Poisson equation, though slightly complicated, it can still be directly solved using,say, the FFT techniques.

With Φ_s being known, the formula

$$\Phi' \Big|_{\sigma = 1} = gh - \Phi_s \Big|_{\sigma = 1} \qquad (2.5.15)$$

from (2.5.11) gives the value of Φ' at the ground surface.

Equation (2.5.15) is crucially important in the model. It builds up a direct relation between the geopotential height field (therefore the pressure gradient force field) and the surface pressure, which is a reflection of the mass convergence in the column above, and only by which can the pressure gradient force interact with the mass convergence field.

However, because of the grid staggering, relation (2.5.15) can not yet be directly used as the boundary condition for the Φ' equation. Extrapolation is required to obtain the value of Φ' at $\sigma=1+\Delta\sigma/2$. To do this we derive from the vertical momentum equation that

$$\frac{\partial \Phi'}{\partial \sigma}\Big|_{\sigma=1} = \{ [\frac{\partial p_* w}{\partial t} + \mathrm{WFLUX} - p_* g(\frac{\theta'}{\theta_s} + 0.61 q'_v + q_c + q_r) - p_* D_w] / (p_* S) \}\Big|_{\sigma=1} \qquad (2.5.16)$$

A simple but reasonable approximation is to assume the hydrostatic balance at the lower boundary by neglecting the vertical acceleration term, which is small anyway. Experiments with dry convection showed the above approximation was reasonable as far as the local solution is concerned, In (2.5.16) WFLUX is available but the local tendency term is unknown. It could possibly be calculated using backward time differencing or simply approximated by its value at early time step. However it is found the solution becomes unstable immediately after the local tendency term in equation (2.5.16) is included, but stable when excluded, unless w itself is approximated by

$$w\big|_{\sigma=1} = \left[-u \frac{\partial p_*}{\partial x} / (p_* S) \right]_{\sigma=1} \qquad (2.5.17)$$

i.e. the contribution of the time tendency of local variation in the surface pressure is neglected. Again this approximation involves neglecting a local time tendency term. The analysis and numerical experiments show that the term $\partial p_* w/\partial t$ is (2.5.16) is difficult to accurately calculate on the lower boundary but on the other hand the solution is extremely sensitive to the inherited error. Therefore we decided to omit this term, on the grounds that its magnitude is small and so will not affect the solution too much. No approximation is made to w at $\sigma=1$ as in (2.5.17). Now we have

$$\frac{\partial \Phi'}{\partial \sigma}\Big|_{\sigma=1} = F_B\big|_{\sigma=1} \qquad (2.5.18)$$

where

$$F_B\big|_{\sigma=1} = \left\{ \left[WFLUX - p_* g \left(\frac{\theta'}{\theta_s} + 0{,}61 q_v' - q_c - q_r \right) - p_* D_u \right] / (p_* S) \right\}_{\sigma=1} \qquad (2.5.19)$$

Finally the lower boundary condition of the elliptic equation for Φ' is the Dirichlet condition

$$\Phi'\big|_{\sigma=1+\Delta\sigma/2} = \Phi'\big|_{\sigma=1} + \frac{\Delta\sigma}{2} \frac{\partial \Phi'}{\partial \sigma}\Big|_{\sigma=1} \qquad (2.5.20)$$

in which $\Phi'\big|_{\sigma=1}$ and $\partial\Phi'/\partial\sigma\big|_{\sigma=1}$ are given respectively by (2.5.15) and (2.5.19).

In summary, the operator for boundary condition (2.5.4) is defined as

$$L_B \equiv \begin{cases} \dfrac{\partial}{\partial x} & 0 \le \sigma \le 1, \ x=0 \text{ and } x=XL \\ \dfrac{\partial}{\partial \sigma} & \sigma = 0, \quad 0 \le x \le 1 \\ 1 & \sigma = 1, \quad 0 \le x \le XL \end{cases} \qquad (2.5.21)$$

In the model calculation, the first guess of Φ' is naturally taken as its value of the previous time step, with its value on the boundary modified to satisfy (2.5.8) (2.5.10)

and (2.5.15). As was discussed in last section, the boundary conditions for the correction equation (2.5.3) are all homogeneous, of Dirichlet type at the lower boundary and of Neumann type at the other boundaries. An unique solution of this elliptic equation exists and can be found using FFT techniques presented in next section.

2.5.3 Direct solution of Poisson equation using Cosine Fourier Transform

In this section we pick up equation (2.5.3) from section 2.5.1 and try to solve it using FFT techniques. Equation (2.5.3) can be written as

$$\left[\frac{\partial^2}{\partial x^2} + \frac{\partial}{\partial \sigma}\left(\overline{S^2} \frac{\partial}{\partial \sigma} \right) \right] \psi = R \qquad (2.5.22)$$

in simplified notations, where $\psi \equiv \Delta\Phi^{p+1}$ and $R \equiv R^p$. The boundary condition for (2.5.22) is

$$L_B (\psi) = 0 \qquad (2.5.23)$$

with L_B defined by (2.5.21).

According to the definition of the model grid in section 2.2, variable ψ is defined at grid points x_i, σ_j, which are in turn defined by (2.1.5) in that section. That is

$$\psi_{i,j} \equiv \psi(i, j) \equiv \psi((i - 1/2)\,\Delta x, (j - 1/2)\,\Delta\sigma)$$
$$0 \le i \le NX+1, \quad 0 \le j \le NS+1 \; . \qquad (2.5.24)$$

Function ψ defined on the grid can be expanded in a finite eigenfunction series that satisfies condition (2.5.23). The boundary conditions in x-direction are homogeneous Neumann conditions (zero gradient), but defined in-between the respective two outermost grid points due to grid-staggering, that is

$$\psi_{0,j} = \psi_{1,j} \quad \text{and} \quad \psi_{NX+1,j} = \psi_{NX,j} \qquad (2.5.25)$$

Therefore we have a even data sequence for which the following holds,

$$\psi_{-i} = \psi_{i+1} \quad \text{and} \quad \psi_{NX-i} = \psi_{NX+i+1} \tag{2.5.26}$$

for i=0,1,...,NX-1 and a given j.

For a data sequence that has the above property, a non-standard Fourier cosine expansion as used by Williams (1969) has to be used here. As such ψ is expanded in a set of harmonics - the cosine functions, in another word data series $\psi_{i,j}$ is transformed from x-space to a spectrum space with the spectrum coefficients being Ψ_k. Hence we have:

$$\psi = \sqrt{\frac{2}{NX}} \sum_{\kappa=0}^{NX-1} \Psi_k \, H_k(i) \tag{2.5.27}$$

where the harmonics

$$H_k(i) = \beta_k \cos \frac{k\,(i - 1/2)\,\pi}{NX} \tag{2.5.28}$$

for k=0,1,...,NX-1, with $\beta_k=2^{-1/2}$ for k=0 and $\beta_k=1$ otherwise. H_k are actually the eigen-functions that satisfy boundary condition (2.5.25).

The period of this expansion is essentially 2NX Δx, with the other half of the series assumed to be the even symmetry of the given data that are defined on the grid. For such an expansion, no sine terms remain and the number of expansion (or spectral) coefficients equals the number of grid points so that the series uniquely matches the data. Similarly, the forcing function R is also expanded into such a series

$$R = \sqrt{\frac{2}{NX}} \sum_{\kappa=0}^{NX-1} Q_k \, H_k(i). \tag{2.5.29}$$

Substituting series (2.5.27) and (2.5.29) into the finite differenced equation of (2.5.22), we obtain

$$\delta_\sigma(\overline{S^2} \, \delta_\sigma \Psi_k) - \lambda_k \, \Psi_k = Q_k \tag{2.5.30}$$

for k=0,1,...,NX-1, where the difference operator is as defined before, and

$$\lambda_k = \left[\frac{2}{\Delta x} \sin\left(\frac{k\pi}{2\,NX} \right) \right]^2 \tag{2.5.31}$$

is the eigen-values of the discrete operator δ_{xx} corresponding to eigenfunction H_k, and they satisfy

$$\delta_{xx} H_k + \lambda_k H_k = 0 \qquad (2.5.32)$$

The boundary condition required by Eq.(2.5.30) for Ψ_k are obtained from (2.5.22) that

$$\frac{\partial \Psi_k}{\partial \sigma}\Big|_{\sigma=1} = 0 \quad \text{and} \quad \Psi_k\Big|_{\sigma=0} = 0 \ . \qquad (2.5.33)$$

Equation (2.5.30) is an ordinary difference equation in σ, which, when discretized, forms a tridiagonal linear system and a unique solution exists given the boundary conditions as in (2.5.33). An algorithm for solving this directly can be found in Richtmyer and Moton (1969), which is superior to the usual Gaussian elimination method because of better computational stability. With the coefficients Ψ_k already obtained, the synthesis of these spectral components is performed according to (2.5.27) for ψ, the solution of elliptic equation (2.5.22). In the actual model computation, the only transforms performed are this synthesis and the analysis of the forcing function R for the spectral coefficients Q_k

$$Q_k = \sqrt{\frac{2}{NX}} \sum_{i=0}^{NX-1} R_i \, H_k(i) \qquad (2.5.34)$$

Since the solution of the elliptic equation accounts for a considerable portion of the total model computations, the optimal computer coding of this part is of significance. Since standard FFT subroutines are usually for complex transforms, certain pre- and post-processing is necessary, in order to achieve a maximum efficiency. Cooley at. al. (1970) developed appropriate pre- and post-processing algorithms for data with three basic boundary conditions on non-staggered grid. In a way similar to Cooley et. al., Wilhelmson and Erichsen (1976) provided the formulae for real data on staggered grid with Neumann boundary conditions. These are implemented in the model so that a

maximum efficiency in the discrete Fourier transform is achieved.

Finally to mention briefly, for the three dimensional version of this model, $\partial^2/\partial x^2$ in equation (2.5.22) becomes a 2-D Laplacian. To solve this equation one only has to perform a further similar transform in y-direction. The resulting ordinary difference equation would appear exactly the same as equation (2.5.29) except that in which λ_k is replaced by,say, $\Lambda_{k,l,}$ the eigen-value of the full 2-D Laplacian.

Chapter Three

Thermodynamics, Cloud Microphysics and Subgrid Scale Mixing

In many mesoscale systems such as mesoscale convective rainbands and squall lines, phase changes of water occur as mesoscale and/or subgrid scale circulations lift air above its condensation level and when the condensed water falls out or detrains from the clouds and evaporates. The presence of these water phases and the conversion between them requires separate conservation equations such as (2.1.6), (2.1.7) and (2.1.8) for each phase and the source/sink terms in these equations to be properly represented. In this chapter the procedure to include the effects of these phase changes of water on both model resolvable scales and subgrid scales is discussed.

Due to computational constraints, it is usually not possible for mesoscale numerical models to resolve turbulence processes. The effects of subgrid scale turbulence can be taken into account through parameterization. The last section of this chapter will consider the formulations of the subgrid scale mixing terms. Some sensitivity experiments on the mixing processes can be found in later chapters.

Furthermore, the implementation of the Flux-Corrected Transport (FCT) advection scheme and the impact of its use on the solutions are also discussed in this chapter.

3.1 Moist thermodynamics and Microphysics parameterizations

The moist processes in a mesoscale model essentially consists of two parts: the explicit condensation and evaporation on model resolvable scales, and the cloud

microphysics that are of subgrid scales and have to be parameterized. In this model water is categorized into three parts: the water vapour, cloud droplets and rainwater. The raindrops differ from cloud water in that they sediment at a parameterized terminal speed. The fall-out of the rainwater from the cloud in which it forms is recognized as a major factor in the growth and decay of a cloud system as the cloud is thereby freed of liquid water loading and the evaporative cooling induced downdraught plays a key role in organizing long-lasting convection. Ice phase is currently not present in the model. The inclusion of it would in general change the distribution of the water quantities to some extent and the freezing and melting would provide an extra heat source and sink. However models without ice phase are still able to capture the essential dynamics of some convective systems (e.g. Thorpe et al. 1982, Klemp and Wilhelmson 1978).

a) Conservation equations

Equations (2.1.6), (2.1.7) and (2.1.8) are the conservation equations for the three water quantities. Symbolically they are written as

$$\frac{dq}{dt} = M_q + D_q \qquad (3.1.1)$$

with q representing either q_v, q_c or q_r. M_q represents parameterized microphysics and explicit condensation / evaporation. D_q denotes subgrid scale mixing. The heat source/sink due to phase changes of water in the thermodynamic equation (equation (2.1.4)) is represented by term M_θ. Rewritten here it is

$$\frac{d\theta'}{dt} = -\frac{\theta_s N_s^2}{g} w + M_\theta + D_\theta + \frac{\dot{Q}}{C_p \Pi} \qquad (3.1.2)$$

The last term represents all other diabatic sources / sinks. The presence of water has other effects including the modification to the air density by water vapour and the drag imposed upon the air by liquid water loading. These effects show themselves in the net buoyancy term in vertical momentum equation (2.1.3).

The microphysical processes can be briefly summarized in the following way. The small cloud droplets are formed when the air becomes saturated and condensation occurs. Raindrops are then formed in a conversion process (named auto-conversion) from these cloud droplets and are then allowed to collect smaller cloud droplets (accretion) as they fall through them at a terminal speed. When cloud droplets are present in unsaturated air they are evaporated until saturation of the air or until they are exhausted before saturation is reached. Raindrops will evaporate in a subsaturated environment at a rate depending on their amount and the saturation deficit. The microphysics terms in the conservation equations are expressed as

$$M_{q_v} = \frac{dq_s}{dt} + E_r \qquad (3.1.3)$$

$$M_{q_c} = - \frac{dq_s}{dt} - A_c - C_r \qquad (3.1.4)$$

$$M_{q_r} = - \frac{\partial}{\partial \sigma}(S V_t q_r) - E_r + A_r + C_r \qquad (3.1.5)$$

and the related diabatic heating in (3.1.2) is

$$M_\theta = - L (\frac{dq_s}{dt} + E_r) / (C_p \Pi) \qquad (3.1.6)$$

The above notation closely follows Klemp and Wilhelmson (1978). Here L is the latent heat of condensation, q_s the specific humidity of saturation. dq_s/dt is the rate of change in specific humidity of air due to condensation or evaporation from cloud water. Terms A_r, C_r and E_r represent respectively auto-conversion and accretion from cloud droplets to rain water and the evaporation of rain water. V_t is the terminal speed of rain water sedimentation.

b) Microphysics parameterizations

Kessler's parameterizations (Kessler, 1969) are used to determine the rates of auto-

conversion (A_r) and accretion (C_r), where C_r is based on the Marshall-Parmer distribution of cloud drop spectrum. The formulae are

$$A_r = k_1 (q_c - q_{crit}) \tag{3.1.7}$$

$$C_r = k_2 q_c q_r^{0.875} \tag{3.1.8}$$

where q_{crit} is a threshold for the auto-conversion to occur. The form of k_2 is complex and is in particular dependent on air density and collection efficiency. Constant values are chosen for these parameters after Soong and Ogura (1973). They are

$$k_1 = 10^{-3}\ s^{-1}, \qquad k_2 = 2.2\ s^{-1}$$

$$q_{crit} = 10^{-3}\ kg/kg\ . \tag{3.1.9}$$

The evaporation rate of rain water can be simply given by

$$E_r = \beta (q_s - q_v) \tag{3.1.10}$$

as was used by Miller and Pearce (1974), by which the rate is proportional to the saturation deficit. The typical value of β is $10^{-3}\ s^{-1}$, a value of $0.5\times10^{-3}\ s^{-1}$ was used by Miller and Pearce in their simulations. A more accurate formula was given by Ogura and Takahashi (1971) and is used in this model, which is

$$E_r = \frac{1}{\rho} \frac{(1 - q_v / q_s) C (\rho_s q_r)^{0.525}}{2.03\times10^4 + 9.58\times10^6 / (p\, q_s)} \tag{3.1.11}$$

where C is the ventilation factor given by

$$C = 1.6 + 30.39 (\rho_s q_r)^{0.2046}\ . \tag{3.1.12}$$

A formula for V_t (positive downwards) in equation (3.1.5) was derived by Soong and Ogura (1973) from an empirical formula relating the rainwater content and the rainfall intensity given by Marshall and Palymer (1948). It was later adjusted to take into account the mean density variation as discussed in Beard (1977),

$$V_t = 14.34(\rho_s\, q_r)^{0.1346} \left(\frac{\rho_s}{\rho_0} \right)^{-1/2} \quad \text{(m/s)} \qquad (3.1.13)$$

where ρ_0 is the reference state density at the ground. In equations (3.1.7)-(3.1.13), the SI unit system is used, namely V_t in m/s, specific humidity q in kg/kg, density ρ in kg/m^3, and pressure p in Pa.

A relatively simple formula of terminal speed was used by Miller and Pearce,

$$V_t = \beta\, q_r^{0.2} \quad \text{(m/s)} \qquad (3.1.14)$$

Here β= 5.32 s^{-1} typically. A modified value of 10 s^{-1} was used Miller (1978) in a simulation of a real cumulonimbus system, considering that the modification may reflect the weighted average of the fall speed of rain drops and hailstones. The timing of the rain falling onto the ground was improved with this modification. Formula (3.1.13) is being used here

c) Condensation and evaporation

The saturation vapour pressure can be obtained by integrating the Clausius-Clapeyron equation (see e.g. Wallace and Hobbs, 1977, page 95). For reasonable values of temperature and pressure within troposphere, the Teten's semi-empirical formula gives a good approximation, which is

$$e_s = 6.11 \exp\left(a\, \frac{\Pi\theta - 273}{\Pi\theta - b} \right)$$

where

$$a = 17.27 \quad \text{and} \quad b = 35.5 \quad \text{for} \quad \Pi\theta \geq 273 \text{ K},$$
$$a = 21.875 \quad \text{and} \quad b = 7.5 \quad \text{for} \quad \Pi\theta < 273 \text{ K} \qquad (3.1.15)$$

Here a and b take different values for temperature above or below freezing level since the saturation vapour pressure e_s is different with respect to water and ice. This difference originates from that between the latent heat of condensation and of freezing (sublimation).

In all the simulations to be discussed later, a and b take those values for positive temperature Celsius. This is thought to be consistent with the assumption that no effect of freezing is taken account of in absence of ice phase. The neglec of this effect generally tends to underestimate the total amount of latent heat released.

Making use of equation (3.1.15), the saturation specific humidity is then

$$q_s = \frac{3.8}{p - 0.378\, e_s} \exp\left(a \frac{\Pi\theta - 273}{\Pi\theta - b} \right) \qquad (3.1.16)$$

The condensation or evaporation is assumed to occur instantly or say within one time integration step, and the process is assumed to be isobaric. Let $\delta\theta$, δq_v be the change to θ and q_v respectively because of the phase changes between water vapour and cloud water. From thermodynamic equation,

$$- L\, \delta q_v = C_p\, \Pi\, \delta\theta \qquad (3.1.17)$$

Because the condensation or evaporation occurs to restore the exact saturation, we have

$$q_v + \delta q_v = q_s (\theta + \delta\theta, p) \qquad (3.1.18)$$

It is clear that the calculation of q_v involves the pressure. In models using height as the vertical coordinate, the determination of pressure demands knowledge of temperature which is related to the rate of latent heat release, therefore to q_s again. The relations between the thermodynamic variables are therefore implicit, as was first pointed out by Ogura and Phillips (1962). However Wilhelmson and Ogura (1972) showed by comparison tests that the pressure p in the equation can be justifiably approximated by its reference state value. Despite this argument, models using pressure or pressure based coordinates still have the advantage of eliminating the problem completely.

To solve equations (3.1.17) and (3.1.18), q_s given by (3.1.16) is expanded into a Tayler's series in $\delta\theta$ around the current state (θ, p). Only terms up to second order in $\delta\theta$ are retained and a quadratic algebraic equation is solved for $\delta\theta$, following Miller and Pearce (1974). The solution is

$$\delta\theta = [- a_1 + (a_1^2 - 4 a_0 a_2)^{1/2}] / (2 a_2) \qquad (3.1.19)$$

in which

$$a_0 \equiv q_s - q_v , \quad a_1 \equiv \frac{C_p \Pi}{L} + q_s x, \quad a_2 \equiv \frac{1}{2} q_s x (x - \frac{2\Pi}{\Pi\theta - b})$$

and $$x \equiv \frac{a (273 - b)}{(\Pi\theta - b)^2}$$

with a and b being given in (3.1.15). Finally from equation (3.1.17), we have

$$\delta q_v = - \frac{C_p \Pi}{L} \delta\theta \qquad (3.1.20)$$

where $\Pi = (\frac{p}{p_0})^{\kappa}$.

The solutions can be checked against equation (3.1.18) for accuracy, and where not satisfactory, iterations are performed using the updated values. In the vectorized computer code of the model, this calculation is carried out at all the grid points with two iterations.

d) Adjustment procedure

The numerical integration of the conservation equations for water quantities follows the commonly used adjustment procedure, which can be divided into two stages. First, temporary values of θ and q are obtained by integrating the conservation equations without the terms relating to the phase changes, then these terms are evaluated using the obtained values according to equations (3.1.3)-(3.1.6), with A_r, C_r, E_r and δq_v in them given respectively by (3.1.7), (3.1.8), (3.1.10) and (3.1.20). The temperature and specific humidity for water quantities are then adjusted by the amount calculated.

3.2 Flux-Corrected Transport advection scheme and its application in the model

It is well known that 'negative water' is constantly generated in numerical models using conventional high order advection schemes (e.g. the leapfrog or Lax-Wendroff scheme) to solve conservation equations. This problem can be avoided by resorting to the first order upstream-forward (one-sided) scheme, but suffers from excessive implicit numerical diffusion. This drawback makes the scheme unsuitable for use especially when sharp gradients in the fields are to be maintained. Clark and Hall (1979) introduced a hybrid-type scheme using a Crowley advection scheme (Crowley, 1978) as a higher-order scheme and an upstream scheme as the low-order scheme. The negative values produced by this scheme is reasonably small but the numerical diffusion is still relatively strong. In this model we apply the flux-corrected transport scheme (FCT) that was first developed by Boris and Book (1973) and generalized by Zalesak (1978) to multi-dimensions. This is applied to the conservation equations for water quantities and to the thermodynamic equation as an option. In addition to the mass conservation property of conventional algorithms, the FCT scheme strictly maintains the positivity of actual mass density being transported (advected), and is particularly capable of handling steep gradients and inviscid shock solutions.

Fig. 3.1 is taken from Boris and Book (1973) and shows the solutions of tests performed on density square waves traveling with a constant speed c using four different schemes. A small amount of diffusion was used in the leapfrog and Lax-Wendroff tests to reduce overshooting. No undershoots are visible in the one-sided (upstream-forward) calculation because of the massive diffusion. The one-dimensional FCT calculation (SHASTA) shows remarkably good agreement with the exact solution and is clearly far superior to the other three basic methods shown in Fig. 3.1.

Fig. 3.1 Square wave test comparisons at two times during the calculation (time step $\Delta t=0.2\Delta x/c$). The solid line is the analytic solution, the dots are computed values. It is clear the solution of FCT scheme is superior to all the others. (Reproduced from Boris and Book,1973).

a) Flux-corrected transport algorithm

The following gives a brief account of FCT as defined by Zalesak (1978).

Consider a simple transport equation in one dimension,

$$\frac{\partial r}{\partial t} + \frac{\partial f}{\partial x} = 0 \qquad (3.2.1)$$

(For water substance conservation equations in this model $r=p*q$, $f=p*qu$, $g=p*q\dot{\sigma}$, g here is the flux in the other dimension).

The finite difference approximation to equation (3.2.1) in flux form can be written as

$$r_i^{n+1} = r_i^n - [\, F_{i+1/2} - F_{i-1/2} \,] \Delta t / \Delta x_i \qquad (3.2.2)$$

Here r and f are defined at the spatial grid points x_i and temporal points t^n and $\Delta x_i=(x_{i+1}$

$-x_{i-1})/2$. The $F_{i+1/2}$ are called transportive fluxes. The functional dependence of F on f defines the integration scheme. In its simplest terms, FCT constructs the net transportive flux point by point (nonlinearly) as a weighted average of a flux computed by a low-order scheme and a flux computed by a high-order scheme. The weighting is done to ensure that the high order flux is used to the greatest extent possible without introducing ripples in the solution. The weighting procedure is referred to as "flux-correction" or "flux-limiting". Formally the procedure is as follows,

1) Compute $F^L_{i+1/2}$, the transportive flux given by some low order scheme guaranteed to give monotonic (ripple free) solutions;

2) Compute $F^H_{i+1/2}$, the transportive flux given by some high order scheme;

3) Define the "anti-diffusive flux"

$$A_{i+1/2} \equiv F^H_{i+1/2} - F^L_{i+1/2} \qquad (3.2.3)$$

4) Compute the updated low order ("transported and diffused") solution:

$$r^{td}_i = r^n_i - [\, F^L_{i+1/2} - F^L_{i-1/2} \,]\, \Delta t / \Delta x_i \qquad (3.2.4)$$

5) Limit the $A_{i+1/2}$ in a manner such that r^{n+1} as computed in step 6) below is free of extrema not found in r^{td} or r^n:

$$A^C_{i+1/2} = C_{i+1/2}\, A_{i+1/2}, \qquad 0 \le C_{i+1/2} \le 1 \qquad (3.2.5)$$

6) Apply the limited anti-diffusive fluxes:

$$r^{n+1}_i = r^{td}_i - [\, A^C_{i+1/2} - A^C_{i-1/2} \,]\, \Delta t / \Delta x_i \qquad (3.2.6)$$

The crucial step in the above is obviously step 5). It is clear that in absence of the flux limiting step, i.e $c_{i+1/2} \equiv 1$, then r^{n+1} would be simply a high order solution, whereas if $c_{i+1/2} \equiv 0$, then the scheme would reduce to the lower order one. This flux-correcting step is pursued under the requirements that the anti-diffusive stage should generate no new maxima or minima in the solution nor should it accentuate already existing extrema.

More specifically, the anti-diffusive flux $A_{i+1/2}$ is limited such that $A^C_{i+1/2}$ acting in concert with $A^C_{i-1/2}$ will not allow r_i^{n+1} calculated by (3.2.6) to exceed some maximum value r_i^{max} nor fall below some minimum value r_i^{min}. These maximum and minimum values are chosen in our calculations as

$$
\begin{aligned}
r_i^a &= \max (r_i^n, r_i^{td}) \\
r_i^{max} &= \max (r_{i-1}^a , \ r_i^a , \ r_{i+1}^a \ ) \\
r_i^b &= \min (r_i^n, r_i^{td}) \\
r_i^{min} &= \min (r_{i-1}^b , \ r_i^b , \ r_{i+1}^b \ )
\end{aligned}
\qquad (3.2.7)
$$

This choice looks back to the previous time step as well as at the transported and diffused solution for upper and lower bounds on r_i^{n+1}. We will not give further details of the formulation of flux limiter, but they can be found in Zalesak (1979).

The high-order scheme used for the FCT in this model is a leapfrog-trapezoidal scheme of second order in both space and time. The low order scheme is the upstream (or the donor cell as is referred to sometimes) scheme plus a zero order diffusion term with coefficient 1/8 (see appendix A for details).

b) Implementation of FCT in the model

With the leapfrog-centred scheme replaced by the FCT Scheme, equations (2.2.7) and (2.2.9)-(2.2.11) are replaced by

$$\delta_{t+\Delta t/2} (p_* \theta') = - TFLUX^{n,C} - \frac{p_* \theta_s N_s^2}{g} \bar{w}^{\sigma} + p_* (M_\theta^n + D_\theta^n) + p_* \dot{Q}/(C_p \Pi) \qquad (3.2.8)$$

$$\delta_{t+\Delta t/2} (p_* \, q) = - QFLUX^{n,C} + p_* (M_q^n + D_q^n) \qquad (3.2.9)\text{-}(3.2.11)$$

where $\delta_{t+\Delta t/2} \, \alpha = [\alpha(t+\Delta t) - \alpha(t)]/\Delta t$ by definition. $TFLUX^{n,C}$ and $QFLUX^{n,C}$ are the fluxes corrected according to the procedure described in the early part of this section.

When FCT is used the diffusion terms are evaluated at the current time level. As is pointed out in appendix A, the second step of the leapfrog-trapezoidal scheme strongly damps the computational mode generated in the leapfrog step, the time filtering discussed in section 2.3 is therefore unnecessary for the variables thus predicted.

The flux correcting procedure [step 5) of the FCT algorithm in part a)] in this model implements Zalesak's multidimensional flux limiter (Zalesak, 1978) in 2 dimensions (x and σ), and it incorporates a 'pre-limiter' step utilizing the strong 1-D limiter of Boris and Book (1973).

Apart from the advection term, the rainwater sedimentation in the rainwater conservation equation is also treated by the FCT scheme, for which the 1-D algorithm of Boris and Book (1973) is used.

The restriction on the time step by the FCT scheme is from the speed of the advective flow, which is however smaller than the phase speed of the fastest wave in the system.

It will be shown in chapter 5 that the use of the FCT scheme significantly improves the conservation of thermodynamic quantities along an air parcel, therefore improves also the simulated circulation of, for example, a moist thermal convection, whose development relies on the buoyancy of the rising air, in excessive of its environment.

In principle, the FCT scheme can also be applied to momentum equations. In the model, velocity is predicted before advecting the thermal and moisture variables, so that a trapezoidal step can be included in the high order scheme for FCT (see Appendix A). The same is certainly not true when advecting velocities. However 1-D calculations show that with a single leapfrog step in the high order scheme the FCT scheme can perform as well, and the time splitting is well suppressed in the flux-correcting process. The FCT scheme has been implemented in the numerical model but has not been fully tested. The potential impact of its use is an improvement in the model accuracy, especially when predicting fields containing sharp velocity gradients, such as those in an intense frontal zone.

3.3 Subgrid scale mixing and numerical diffusion

As was pointed out at the beginning of this chapter, the turbulence processes in models for mesoscale flows are usually not negligible. The turbulence acts on subgrid scales to transfer momentum, heat, and other quantities, and their effects can only be parameterized. Although a number of formulations of parameterization have been devised and some of them have even become more or less standard, problems as to the dependency of turbulent activities on the grid resolution and the extent to which the turbulent processes influence the solution on model resolvable scales are still not very well understood. The extensive investigation of this aspect is beyond the scope of the current work of model development, we only outline here the formulations of these mixing terms and possible variations from them for particular problems.

3.3.1 Deformation and Richardson number dependent formulation

Smagorinsky (1963) suggested a formulation for the subgrid scale mixing coefficient in a two-dimensional general circulation model that depends on the amplitude of deformation tensor and the grid interval. Lilly (1962) extended this for use in his two-dimensional convection model to take into account the contribution of the convective available potential energy through the dependency of the coefficient on Richardson number. This formulation is since used by quite a number of modelers including Clark (1976), Durran and Klemp (1983). According to this, the terms representing turbulent momentum transfer are expressed in terms of a Reynolds stress tensor which is then parameterized by a first order closure method. The two-dimensional formulation of the mixing terms in height z coordinates is as

$$D_u = \frac{\partial \tau_{11}}{\partial x} + \frac{\partial \tau_{13}}{\partial z}$$

$$D_w = \frac{\partial \tau_{31}}{\partial x} + \frac{\partial \tau_{11}}{\partial z} \qquad (3.3.12)$$

The stress tensor is symmetric, i.e. $\tau_{ij}=\tau_{ji}$ and it is related to the deformation tensor D_{ij}

through momentum diffusion coefficient K_m such that

$$\tau_{ij} = K_m D_{ij} \tag{3.3.13}$$

and in two dimensions the elements of the deformation tensor are

$$D_{11} = - D_{33} = \frac{\partial u}{\partial x} - \frac{\partial w}{\partial z} \equiv A$$

$$D_{13} = D_{31} = \frac{\partial u}{\partial z} + \frac{\partial w}{\partial x} \equiv B \tag{3.3.14}$$

where the subscripts 1 and 3 denote x and z coordinate respectively.

The formulation of the first order closure scheme for K_m suggested by Lilly (1962) is

$$K_m = k^2 \Delta x \, \Delta z \, | Def | \times [\, Max(\, 1 - \frac{K_H}{K_m} Ri \, , \, 0 \,) \,]^{1/2} \tag{3.3.15}$$

where

$$| Def | \equiv \frac{1}{2} \, (D_{11}^2 + D_{33}^2) + D_{13}^2 = A^2 + B^2 \tag{3.3.16}$$

is the magnitude of deformation and R_i is the Richardson number defined as

$$R_i = \begin{cases} g \dfrac{\partial \ln \theta}{\partial z} \Big/ |Def|^2 & \text{for } q_v < q_s \\ g \dfrac{\partial \ln \theta_e}{\partial z} \Big/ |Def|^2 & \text{for } q_v \geq q_s \end{cases} \tag{3.3.17}$$

in which the moist Richardson number is used in regions of saturation. k=0.21 as suggested by Deardorff (1971).

The thermal mixing term in the thermodynamic equation is

$$D_\theta = \frac{\partial}{\partial x} (K_H \frac{\partial \theta}{\partial x}) + \frac{\partial}{\partial z} (K_H \frac{\partial \theta}{\partial z}) \tag{3.3.18}$$

and similarly those for the water contents q_v, q_c, q_r are as

$$D_q = \frac{\partial}{\partial x} (K_q \frac{\partial q}{\partial x}) + \frac{\partial}{\partial z} (K_q \frac{\partial q}{\partial z}) \tag{3.3.19}$$

Generally $K_q=K_H$. $K_H/K_m=Pr^{-1}$, Pr is the turbulence Prandtl number−the ratio of eddy viscosity to the eddy conductivity. Deardorff (1972) suggested $K_H/K_m=3$, which allows the turbulence to set in when Ri falls belows 1/3, a value slightly greater than the commonly accepted critical value Ri=1/4. Other values are assumed sometimes by different modelers such as $K_H/K_m=1$ was used by Clark (1976) in the mountain gravity wave experiments. We leave this parameter to be determined in later simulations.

3.3.2 The model implementation

In our model the formulations presented in the proceeding section are transformed into (x,σ) coordinates with approximations in the transformation consistent with those made to obtain the quasi-non-hydrostatic system, that is, the non-hydrostatic contribution is only retained when the vertical acceleration is concerned and the variables as the coefficients in the equations are approximated by their reference state values. The formulae for transformation are

$$\left(\frac{\partial f}{\partial x}\right)_{z=const.} \approx \left(\frac{\partial f}{\partial x}\right)_{\sigma=const.} - \frac{\sigma}{p_*}\frac{\partial p_*}{\partial x}\frac{\partial f}{\partial \sigma}$$

$$\frac{\partial f}{\partial z} \approx -S\frac{\partial f}{\partial \sigma} \qquad (3.3.20)$$

and f is any dependent variable. The hydrostatic relation for the reference state gives

$$\delta z \approx -\frac{p_* R T_s}{pg}\delta\sigma = -S^{-1}\delta\sigma\,, \qquad (3.3.21)$$

therefore $\Delta z=\Delta\sigma/S$ is substituted for in (3.2.15) where $\Delta\sigma$ is the grid interval.

The mixing terms of the second order derivatives are rather complicated after the transformation. We calculate A defined in (3.3.14) at the temperature grid points and B at the vorticity grid points shown as the corners of the grid box in Fig. 2.1. Then

$$A = \delta_x u - \sigma\,\delta_x\overline{p_*}^{x}/p_*\,\delta_\sigma\overline{u}^{x\sigma} + S\,\delta_\sigma w$$

$$B = \delta_x W - \sigma\,\delta_x p_*/\overline{p_*}^{x}\,\delta_\sigma\overline{w}^{x\sigma} - \overline{S}^{x}\,\delta_\sigma u \qquad (3.3.22)$$

Coefficient K_m is evaluated at the same grid points as A. i.e. the temperature grid points, at which

$$R_i = - gS \, \delta_\sigma \bar{\theta}^\sigma \, / [\, \theta_s \, (A^2 + \bar{B}^{x\sigma \, 2}) \,] \qquad (3.3.23)$$

Here $\theta=\theta_e$ when $q_c>0$, i.e. saturation is reached at all points involved in calculation of static stability, K_m is calculated according to (3.3.15) and $K_H=K_m/Pr$. Finally the mixing (diffusion) terms are calculated as follows

$$D_u = \delta_x (K_m A) - \sigma(\delta_x p_* / \bar{p}_*^{\,x}) \, \delta_\sigma (\bar{K}_m^{x\sigma} \; \bar{A}^{x\sigma}) - \bar{S}^{x} \, \delta_\sigma (\bar{K}_m^{x\sigma} B)$$

$$D_w = \delta_x (\bar{K}_m^{x\sigma} B) - \sigma(\delta_x \bar{p}_*^{\,x} / p_*) \, \delta_\sigma (K_m \, \bar{B}^{x\sigma}) + \bar{S}^{\sigma} \, \delta_\sigma (K_m A) \qquad (3.3.24)$$

Note that in a finite difference form, the above formulations are not exactly conservative since they are not in the flux form. These terms can therefore introduce spurious source or sink in the interior of model domain. However, in the case where the diffusion / mixing terms are of secondary importance and the spatial resolution is reasonably high, this effect should be unnoticable. The fact that the isentropes represent very well the flow trajectories in later experiments of e.g. dry mountain waves lends support to the above argument. Meanwhile, there may be formulations that are more accurate to be found out.

For the turbulent mixing of heat, we evaluated

$$E = \delta_x \theta \; - \sigma (\delta_x p_* / \bar{p}_*^{\,x}) \, \delta_\sigma \bar{\theta}^{x\sigma} \qquad (3.3.25)$$

at u-points and

$$G = - \bar{S}^{\sigma} \, \delta_\sigma \theta \qquad (3.3.26)$$

at w-points. And we refer to $H_1=K_H \, E$ as the horizontal and $H_3=K_H \, G$ as the vertical turbulent heat flux. Then the thermal mixing is

$$D_\theta = \delta_x (\bar{K}_H^{x} \, E) - \sigma(\delta_x \bar{p}_*^{\,x} / p_*) \, \delta_\sigma (\bar{K}_H^{\sigma} \, \bar{E}^{x\sigma}) - S \, \delta_\sigma (\bar{K}_H^{\sigma} \, G) \qquad (3.3.27)$$

The mixing terms for water substances are calculated exactly the same as for temperature, so that

$$D_q = \delta_x(\overline{K}_q^x \, E_q) - \sigma(\delta_x \bar{p}_*^x / p_*) \, \delta_\sigma(\overline{K}_q^\sigma \, \overline{E}_q^{x\sigma}) - S \, \delta_\sigma(\overline{K}_q^\sigma \, G_q) \qquad (3.3.28)$$

where E_q and G_q are defined for water quantities corresponding to the E and G for temperature.

As we can see, an average over grid points is frequently required in the above calculations. If K_m is evaluated also at the vorticity points, many of these averages can be removed, but this is achieved in the cost of more computations. In viewing that these averages are not necessarily harmful to the solution, we chose to use the current formulations.

Since the mixing terms are of second order derivatives, boundary conditions are required for the momentum stress and turbulent fluxes of heat and water quantities. A proper treatment of these conditions is necessary since the turbulent fluxes are acting together with the advection terms at the boundary to change the budget of momentum, heat and water quantities in the model domain.

At the top boundary σ=0 the momentum stress and heat flux are assumed zero, i.e

$$\begin{aligned} \overline{\tau}_{11}^{\sigma} \Big|_{\sigma=0} &= \tau_{13} \Big|_{\sigma=0} = 0 \\ \overline{H}_1^{\sigma} \Big|_{\sigma=0} &= H_3 \Big|_{\sigma=0} = 0 \end{aligned} \qquad (3.3.29)$$

The same is true for the fluxes of other scalar quantities.

At the bottom boundary σ=1, assume there is a surface drag which acts to exchange momentum with the ground surface, then

$$\tau_{13} \Big|_{\sigma=1} = \tau_x \quad \text{but} \quad \overline{\tau}_{11}^{\sigma} \Big|_{\sigma=1} = 0 \qquad (3.3.30)$$

and for the turbulent heat flux, we have

$$\overline{H}_1^{\sigma} \Big|_{\sigma=1} = 0 \quad \text{and} \quad H_3 = H_{surf} \qquad (3.3.31)$$

Here τ_x and H_{surf} are either specified or related to other dependent variables. The surface heat and moisture fluxes have important contributions in problems such as those in relation to the land/see breeze and boundary layer processes, only that they are not the main interests of the current research. If no surface drag is included and no heat flux exists at the surface, then $\tau_x=H_{surf}=0$. The boundary conditions for the moisture flux is similar to (3.3.31). $\tau_x=H_{surf}=0$ is to be assumed in all of our later experiments.

On the lateral boundaries, velocities outside the boundary are known from the boundary conditions discussed in Section 2.4.1, the stress terms can therefore be calculated as usual up to the boundary, but we need to specify

$$\tau_{11}\Big|_{x=-\Delta x/2} = \tau_{11}\Big|_{x=\Delta x/2}$$
$$\tau_{11}\Big|_{x=XL+\Delta x/2} = \tau_{11}\Big|_{x=XL-\Delta x/2} \qquad (3.3.32)$$

The turbulent fluxes (different from the advective fluxes) of heat and water quantities through the lateral boundaries are set to zero, at least for our purposes. Therefore

$$H_1\Big|_{x=0} = H_1\Big|_{x=XL} = 0 \quad . \qquad (3.3.33)$$

Furthermore because the forcing function of the elliptic equation for geopotential [F_Φ in (2.1.14)] involves derivatives of even higher order, momentum mixing terms D_u and D_w are required outside the boundary. The following assumptions are made,

$$D_u\Big|_{\sigma=-\Delta\sigma/2} = D_u\Big|_{\sigma=\Delta\sigma/2}, \quad D_u\Big|_{\sigma=1+\Delta\sigma/2} = D_u\Big|_{\sigma=1-\Delta\sigma/2}$$
$$D_w\Big|_{x=-\Delta x/2} = D_w\Big|_{x=\Delta x/2}, \quad D_w\Big|_{x=XL+\Delta x/2} = D_w\Big|_{x=XL-\Delta x/2} \qquad (3.3.34)$$

so that the normal gradient of mixing vanishes at the boundaries. And also the mixing terms on the boundary is set to equal their values on the immediately interior grid points.

$$D_w\Big|_{\sigma=0} = D_w\Big|_{\sigma=\Delta\sigma}, \quad D_w\Big|_{\sigma=1} = D_w\Big|_{\sigma=1-\Delta\sigma}$$
$$D_u\Big|_{x=0} = D_u\Big|_{x=\Delta x}, \quad D_u\Big|_{x=XL} = D_u\Big|_{x=XL-\Delta x} \quad . \qquad (3.3.35)$$

3.3.3 An alternative formulation of subgrid mixing

In the proceeding sections, we discussed the deformation and Richardson number dependent formulation of subgrid scale mixing after Lilly (1962). Although it is comprehensive and can be regarded as a reasonable parameterization of subgrid scale turbulences, there are circumstances to which this formulation is not best suited. According to this formulation, very strong mixing will occur in regions of strong shear, but such mixing might be unwanted for a particular problem. In such cases one may wish to specify the mixing coefficients to suit his purpose. Therefore we incorporate in this model as an option another formulation of mixing (to be referred to as formulation two while the previous one as formulation one), while the second can be considered a reduced version of the previous one.

The momentum mixing terms in z-coordinates are then

$$D_u = \frac{\partial}{\partial x}\left(K_m \frac{\partial u}{\partial x}\right) + \frac{\partial}{\partial z}\left(K_m \frac{\partial u}{\partial z}\right)$$

$$D_w = \frac{\partial}{\partial x}\left(K_m \frac{\partial w}{\partial x}\right) + \frac{\partial}{\partial z}\left(K_m \frac{\partial w}{\partial z}\right) \qquad (3.3.36)$$

and those for scalar quantities are of the same form

$$D_\theta = \frac{\partial}{\partial x}\left(K_H \frac{\partial \theta}{\partial x}\right) + \frac{\partial}{\partial z}\left(K_H \frac{\partial \theta}{\partial z}\right) \qquad (3.3.37)$$

$$D_q = \frac{\partial}{\partial x}\left(K_q \frac{\partial q}{\partial x}\right) + \frac{\partial}{\partial z}\left(K_q \frac{\partial q}{\partial z}\right). \qquad (3.3.38)\text{-}(3.3.40)$$

Here the coefficients K_m, K_H and K_q are usually constant or specified function of independent variables, and the ratio K_H/K_m is the inverse Prandtl number Pr^{-1} as before. The formulae for the scalars are unchanged from those of formulation one while momentum mixing terms in (3.3.36) are the reduced version of (3.3.12) when K_m is constant. By this formulation the components of momentum are treated in the mixing process relatively independent of each other and in a way more like scalars are, which follows the rule of down-gradient transport. This formulation provides only a crude

representation of subgrid scale turbulent mixing, but it enjoys the simplicity in computation and offers greater flexibility for numerical experiments. A number of sensitivity experiments concerning the squall lines were conducted and will be reported in later chapters.

In this model, formulae (3.3.36)-(3.3.40) are as before transformed into the (x,σ) coordinates and are implemented in largely the same way as those of formulation one. The same boundary conditions are specified for these mixing terms only that here the definition of stress tensor is different, e.g. now $\tau_{11}=K_m \partial u/\partial z$.

3.3.4 Some computational considerations of diffusion / damping

As was pointed out in Section 2.2, the conservative formulation of this model effectively suppresses the non-linear numerical instability due to wave spectrum aliasing. In most circumstances such as the simulation of free convection and mountain gravity waves, the model can be run stably without any artificial diffusion or turbulence mixing parameterization. However in practice the numerical diffusion is required in order to remove the roughness that is almost inevitable in numerical solutions (see Fig 3.1, for example, ripples are produced by the second order finite difference schemes in the solutions of a simple square wave advection, although they are nearly absent in the FCT solution) as well as to combat with other artifacts of the model such as the false reflection from the boundary. Such diffusion is either added separately to the model equations or included in the mixing terms. In fact, the mixing terms also to some extent play a similar role as the numerical diffusion.

Both formulations imply the mixing on full quantities like momentum, full potential temperature and specific humidities. The mixing has therefore a tendency to destroy non-constant fields specified for the ambient or reference state, which in many model experiments is to be maintained during the time integration. For these reasons, we incorporate in the the model an option for the mixing to operate either on the full variables

or the perturbations only, and include an additional term that represents background diffusion. This term has a same formulation as the mixing term, only that its coefficient is usually a small constant, and it always operates on perturbations only.

Let $D(\psi;K)$ represent a mixing term of either formulation given in preceding sections which operates on variable ψ with parameter K being the diffusion coefficient, then the actual diffusion term D_ψ in the model is expressed as

$$D_\psi = D\ (\alpha_K\psi+(1-\alpha_K)\psi' ;\ K_\psi) + D\ (\psi' ;\ K_B) \qquad (3.3.41)$$

where ψ' is the deviation of full variable ψ (being u, v, w, θ, q, etc.) from a reference state, α_K is a switching parameter which takes value 1 or 0 for mixing on full or perturbations. K_ψ is the coefficient for turbulent mixing while K_B ($\geq$0) is a coefficient for a background diffusion.

It should be noted that when D represents momentum mixing of formulation one [see Eq.(3.3.12)], more than one momentum components are involved in the stress calculations, and ψ here then symbolizes several momentum components.

The top of the model is an artificial boundary that reflects wave disturbances approaching it. The removal of such reflection is essential, especially for problems concerning gravity waves. An absorbing layer is included near the top boundary, with enhanced damping gradually increased from a certain height to the top. Two types of damping are possible, one takes a form of viscous friction whereas the other is in the form of Rayleigh friction. The friction in both cases is applied in the absorbing layer to the perturbations of variable and is added to the right hand side of the equations for u, v, w, θ', q_v, q_c, and q_r.. The damping terms of the viscous friction type before being transformed into σ-coordinates are expressed in a general form:

$$D'_\psi = \frac{\partial}{\partial x}\left(K_D \frac{\partial \psi'}{\partial x}\right) + \frac{\partial}{\partial z}\left(K_D \frac{\partial \psi}{\partial z}\right) \qquad (3.3.42)$$

where ψ' is any of the variables u', v, w', θ', q'_v, q_c and q_r while the damping coefficient profile is specified after Klemp and Lilly (1978) as

$$K_D = \begin{cases} \alpha_D \cos^2\left(\frac{\pi}{2}\frac{z - z_t}{z - z_m}\right) & \text{for } z_m \le z \le z_t \\ 0 & \text{otherwise} \end{cases} \qquad (3.3.43)$$

where z_t is the average height of the top boundary and z_m the height of the bottom of the absorbing layer. $z=\Phi_s/g$ and $\pi=3.14159$. α_D is chosen in the actual simulations so that the dominant wave modes are absorbed most effectively. Klemp and Lilly (1978) suggested that, for linear hydrostatic waves, the minimum depth of the absorbing layer is approximately one vertical wavenumber. In this σ-coordinate model the vertical levels are stretched with height, the model levels in an absorbing layer of a given depth are therefore relatively fewer, this makes the model calculation relatively economic.

Alternatively, Rayleigh friction can be used in the absorbing layer (e.g. Clark 1977), and it is given as

$$D'_\psi = - K_R \psi' \qquad (3.3.44)$$

where the inverse of K_R ($1/K_R$) is the e-folding time of damping. K_R is specified to have a same profile as K_D given in (3.3.43), only that α_D is replaced be α_R.

The viscous friction damps disturbances by redistributing anomalies in the fields, while maintaining the overall conservation (not exactly on certain irregular grid) and it is more selective than Rayleigh friction. However the calculation of the former is much more complicated than that of the latter, especially in transformed coordinates. Moreover, the Rayleigh friction has the tendency of relaxing the fields back to a given reference state, and often appears more effective in removing disturbances of whatever scales in the solution. In the later experiments, Rayleigh type damping is more frequently used.

Different from the approach of absorbing layer, Klemp and Durran (1983) designed a new type of radiation upper boundary condition, which determines the pressure at the upper boundary of a compressible model from the Fourier transformed vertical velocity. The applicability of such a condition to the current model seems worth exploring.

Chapter Four

Dry and Moist Flow over 2-D Orography -Mountain gravity waves and severe downslope winds

In this chapter, a number of problems relating to air flow over two dimensional mountain ridges are studied, using the numerical model developed in the previous chapters. In the first two sections, fundamental theories (mainly linear) on mountain gravity waves are briefly reviewed, this provides the materials for the model verifications in the next section and the general background towards the understanding of gravity wave dynamics. Readers who are already familiar with mountain wave problems may skip these two sections, but may refer back occasionally while reading subsequent text. Section 4.3 contains a set experiments of mountain waves in various wave regimes (corresponding to various mountain scales). The results are compared with analytical solutions presented in section 4.2 and very satisfactory agreement is found. A hydrostatic version of the model is also tested. The section that follows is devoted to a further modeling study of the 11 January 1972 Boulder severe downslope windstorm. The results of our model simulation are presented after a brief review of existing theories. Our simulations are extended beyond the time reported in previous studies, and show that the surface pressure drag triples once more after this time. The resulting flow pattern suggests strongly that the mechanism of flow transition below a region of wave breaking as suggested by Smith is the one responsible for the flow acceleration on the lee slope. Other aspects of the greatly amplified wave system are also addressed. Finally in section 4.5 we describe a series of experiments of dry and moist lee waves based on two

observed soundings. Problems on the formation of lee waves and the effects of moist condensation on them are studied and a number of informative results are obtained. The details will be found in the appropriate sections.

4.1 Internal gravity waves in a stratified rotational flow

In this section, the general solutions of linear internal gravity waves are briefly reviewed, the application of these solutions to mountain gravity wave problems will be discussed in next section.

a) The governing equations

The anelastic set of equations in height coordinates (Ogura and Phillips 1972) is used on a f-plane to describe the flow in two dimensions, i.e. the perturbations are independent of coordinate y. The dependent variables are expressed as the sum of the reference state value and the perturbation part, with the reference state being in hydrostatic and the thermal wind balance. This set consists of the horizontal and vertical momentum equations, and the equations for thermodynamics and mass continuity. When linearized around the reference state with a balanced basic flow $\bar{U}(z)$, these equations are written as

$$(\frac{\partial}{\partial t} + \bar{U}\frac{\partial}{\partial x})u + w\frac{d\bar{U}}{dz} - fv = -\frac{1}{\bar{\rho}}\frac{\partial p}{\partial x} \qquad (4.1.1a)$$

$$(\frac{\partial}{\partial t} + \bar{U}\frac{\partial}{\partial x})v + fu = 0 \qquad (4.1.1b)$$

$$(\frac{\partial}{\partial t} + \bar{U}\frac{\partial}{\partial x})w = -\frac{1}{\bar{\rho}}\frac{\partial p}{\partial z} - \frac{\rho}{\bar{\rho}}g \qquad (4.1.1c)$$

$$(\frac{\partial}{\partial t} + \bar{U}\frac{\partial}{\partial x})\rho = -\bar{\rho}N^2 w/g \qquad (4.1.1d)$$

$$\frac{\partial u}{\partial x} + \frac{\partial w}{\partial z} = -\frac{1}{\bar{\rho}}\frac{d\bar{\rho}}{dz}w \qquad (4.1.1e)$$

with the basic state satisfying

$$f\bar{U} = -\frac{1}{\bar{\rho}}\frac{\partial \bar{p}}{\partial y}$$

and $$\frac{d\bar{p}}{dz} = -\bar{\rho}\, g,$$

where $$N^2 = -g\left(\frac{d\ln\bar{\rho}}{dz} + \frac{g}{\bar{C}^2}\right) = \frac{g}{\bar{\theta}}\frac{d\bar{\theta}}{dz}$$

is the Brunt-Vaisala frequency of the reference state and $\bar{C}^2=R\bar{T}\gamma$, $\gamma=C_p/C_v$. All variables are in conventional notation and the over-barred variables represent the reference state whereas the others represent the deviations from that state. On obtaining the above equations, a term representing the contribution from acoustic waves to the density changes is neglected.

If the Boussinesq approximation is made, the dependence of equations on the density of the reference state is eliminated. However this approximation is not justified for deep flows. This difficulty is circumvented by introducing new variables

$$(U,V,W) \equiv (\bar{\rho}/\rho_0)^{1/2}\,(u,v,w)$$

$$P \equiv (\bar{\rho}/\rho_0)^{-1/2}\,p$$

where ρ_0 is the constant density at the ground surface. The square of the transformed velocity is proportional to the wave kinetic energy. In terms of these new variables equations in (4.1.1) become

$$\left(\frac{\partial}{\partial t} + \bar{U}\frac{\partial}{\partial x}\right)U + W\frac{d\bar{U}}{dz} - fV + \frac{1}{\rho_0}\frac{\partial P}{\partial x} = 0 \qquad (4.1.2a)$$

$$\left(\frac{\partial}{\partial t} + \bar{U}\frac{\partial}{\partial x}\right)V + fU = 0 \qquad (4.1.2b)$$

$$\left(\frac{\partial}{\partial t} + \bar{U}\frac{\partial}{\partial x}\right)^2 W + N^2 W + \frac{1}{\rho_0}\left(\frac{\partial}{\partial z} - \Gamma\right)\frac{\partial P}{\partial t} = 0 \qquad (4.1.2c)$$

$$\frac{\partial u}{\partial x} + \frac{\partial w}{\partial z} + \Gamma w = 0 \qquad (4.1.2d)$$

Equation (4.1.2c) is obtained by combining Eqs. (4.1.1c) and (4.1.1d) so as to eliminated ρ from the system. In the above $\Gamma \equiv \frac{1}{2}\frac{d\ln\bar{\rho}}{dz}$ is a stratification parameter. When

the Boussinesq approximation is made, $\Gamma = 0$.

A single equation for vertical velocity W is derived from equations in (4.1.2) as:

$$\left(\frac{\partial}{\partial t} + \bar{U}\frac{\partial}{\partial x}\right)^2\left(\frac{\partial^2}{\partial x^2} + \frac{\partial^2}{\partial z^2} - \Gamma^2\right)W + f^2\left(\frac{\partial^2}{\partial z^2} - \Gamma^2\right)W + N^2\frac{\partial^2 W}{\partial x^2}$$

$$+ \left(\frac{\partial}{\partial z} - \Gamma\right)\frac{d\bar{U}}{dz}\left(\frac{\partial}{\partial t} + \bar{U}\frac{\partial}{\partial x}\right)\frac{\partial W}{\partial x} = 0 \quad . \quad (4.1.3)$$

This equation, and its variations, will play a central role in the analysis of free and forced mountain gravity waves.

b) The dispersion relation

We consider here an atmosphere with a uniform basic flow and stratification, i.e. $\bar{U}$, N^2 and Γ are all constant. The last term in equation (4.1.3) then disappears. We can then write one of the Fourier components of the wave solution as

$$W = W_0 \exp[i(kx+mz-\omega t)] \quad (4.1.4)$$

where k, m are the wavenumbers and ω the frequency.

Substitution of the solution into equation (4.1.3) gives us a dispersion relation for internal gravity waves in rotating fluid,

$$(\omega - \bar{U}k)^2 = [f^2(m^2+\Gamma^2) + N^2k^2]/(k^2+m^2+\Gamma^2). \quad (4.1.5)$$

Various assumptions can be made depending on the relative magnitude of each term to simplify this relation. When considering steady waves in a fixed frame of reference, $\omega=0$; when the vertical scale of the waves is much smaller than the density scale height, the Boussinesq approximation can be made, i.e. $m^2 \gg \Gamma^2$ so that Γ^2 is neglected; furthermore, non-rotating, hydrostatic assumptions can be made in appropriate wave regimes.

The phase speed and group velocity can be worked out easily from the dispersion relation, and they are very useful in understanding the properties of each individual wave mode. We will not going further into details but the discussions on these can be found in Gill (1984).

4.2 Mountain gravity waves

4.2.1 Linear solutions of mountain gravity waves

Mountain gravity waves have attracted much attention because they have both local and far-reaching effects on the atmospheric flow. Large amplitude waves can produce severe downslope winds of destructive force, turbulence can be generated as a result of mountain wave breaking, low-level trapped lee waves can reach considerable amplitudes and produce spectacular lee wave clouds. The transport of momentum by mountain waves to high levels and the subsequent feeding of such energy into the atmosphere has been known to have an important effect on the atmospheric momentum distribution, even a rather crude representation of the drag in association with the mountain wave breaking has resulted in noticeable improvement in the performance of general circulation models. Linear analyses of mountain gravity waves have been carried out by many authors and excellent reviews were made by Alaka (1960) and Smith (1979). We will here give only a brief account of the most relevant parts of these theories.

Following Queney (1948), we consider a semi-infinite, uniformly stratified (N^2=const.) two dimensional flow with a unperturbed speed of $\bar{U}$. The steady state solution is sought, therefore $\partial/\partial t=0$. In this case equation (4.1.3) reduces to

$$\frac{\partial^2}{\partial x^2}(W_{xx}+W_{zz}) + \frac{f^2}{\bar{U}^2}(W_{zz} - \Gamma^2 W) + \left(\frac{N^2}{\bar{U}^2} - \Gamma^2\right) W_{xx} = 0 \ . \qquad (4.2.1)$$

An even simpler equation is obtained when f=0, i.e. rotation is negligible, by integrating equation (4.2.2) with respect to x twice, so that

$$W_{xx} + W_{zz} + l^2 W = 0 \qquad (4.2.2)$$

where

$$l^2(z) \equiv \frac{N^2}{\bar{U}^2} - \Gamma^2, \qquad (4.2.3)$$

with l being known as the Scorer parameter for constant flow. This is an important

parameter which determines whether a wave of a particular wavenumber can propagate in the vertical. As the flow at the ground level is required to follow the lower boundary at z=h(x), the linearized lower boundary condition is written as

$$W(x,0) = \bar{U} \frac{dh}{dx} \qquad \text{at} \qquad z = 0. \tag{4.2.4}$$

Since the system is linear, the solution is a Fourier synthesis of the wave components as given in equation (4.1.4) (here ω=0 for steady waves), i.e.,

$$W(x,z) = \mathrm{Re} \int_0^\infty \tilde{W}(k,m) \exp[\, i\,(kx+mz)\,]\, dk \tag{4.2.5}$$

in which the wave amplitude $\tilde{W}$ is determined from lower boundary condition

$$\tilde{W}(k,m) = \tilde{W}(k) = i\,\bar{U}\,k\,\tilde{h}(k) \quad . \tag{4.2.6}$$

Here $\tilde{h}(k)$ is the Fourier transform of the mountain profile h(x),

$$\tilde{h}(k) = \frac{1}{\pi} \int_{-\infty}^{\infty} h(x) \exp(-ikx)\, dx. \tag{4.2.7}$$

It is more convenient to look at the problem in terms of the displacement of the air-stream due to wave motion. Let η be the streamline displacement, since

$$w = \bar{U} \frac{\partial \eta}{\partial x}\,, \tag{4.2.8}$$

using equations (4.2.5), (4.2.6), (4.2.7) and (4.2.8), we have the solution:

$$\eta(x,z) = \left[\frac{\rho_0}{\bar{\rho}} \right]^{1/2} \mathrm{Re} \int_0^\infty \tilde{h}(k) \exp[\, i\,(kx+mz)\,]\, dk. \tag{4.2.9}$$

The dispersion relation (4.1.5) is now written as

$$m^2 = \frac{(N^2 - k^2\bar{U}^2)\,k^2 + (f^2 - \bar{U}^2k^2)\,\Gamma^2}{k^2\bar{U}^2 - f^2} = \frac{(l^2 - k^2)\,k^2 + \Gamma^2 f^2/\bar{U}^2}{k^2 - f^2/\bar{U}^2} \qquad (4.2.10)$$

where l^2 is as defined in (4.2.3). This relation can also be obtained directly by substituting solution (4.2.5) into equation (4.2.1). The particular case of the solutions of gravity waves forced by a bell shaped mountain of various horizontal scales will be examined in section 4.2.3.

4.2.2 Momentum and energy flux in linear mountain waves

We consider here the steady state , non-rotating, waves forced by an isolated mountain ridges, therefore the wave disturbances would tend to zero as $x \to \pm\infty$ if the solution is not resonant.

The vertical flux of wave energy is defined as

$$F_e = \int_{-\infty}^{\infty} pw \; dx \,. \qquad (4.2.11)$$

For non-rotating, steady state flow, the linearized horizontal momentum equation (4.1.1a) becomes

$$\bar{\rho}\,\bar{U}\frac{\partial u}{\partial x} + \bar{\rho}\,w\frac{d\bar{U}}{dz} = -\frac{\partial p}{\partial x}\,. \qquad (4.2.12)$$

By performing integral $\int_{-\infty}^{\infty} dx$ on this equation and making use of the remote conditions one obtains

$$p = \bar{\rho}\,\bar{U}\,(u + \eta\,\bar{U}_z) \qquad (4.2.13)$$

in which $w = \bar{U}\frac{\partial \eta}{\partial x}$ is used. Substituting this into the energy flux yields

$$\int_{-\infty}^{\infty} pw\,dx = -\,\bar{\rho}\,\bar{U}\int_{-\infty}^{\infty} uw\,dx\,, \qquad (4.2.14)$$

in which $$F_m = \bar{\rho} \int_{-\infty}^{\infty} uw \, dx \qquad (4.2.15)$$

is the vertical flux of horizontal momentum. It is clear that in a layer where $\bar{U}$ is everywhere positive, the vertical flux of wave energy and of momentum are of opposite sign, i.e. if wave energy is transferred upwards, the momentum is transferred downwards. This is actually the case of mountain waves in which the mountain is a source of wave energy but a sink of wave momentum, the latter is due to the mountain pressure drag acting on the flow.

At the mountain surface the pressure drag is defined as

$$D = \bar{\rho} \int_{-\infty}^{\infty} p(x,z=h) \frac{dh}{dx} \, dx \, . \qquad (4.2.16)$$

By using (4.2.13), D can be written as

$$D = -\bar{\rho} \int_{-\infty}^{\infty} uw \, dx \, , \qquad (4.2.17)$$

which is exactly the amount of momentum lost by the flow at the mountain surface.

It is shown by Eliassen and Palm (1961) that the vertical flux of horizontal momentum is constant with height for linear mountain waves, except at levels where $\bar{U}$ =0, this can be expressed as

$$\bar{\rho} \int_{-\infty}^{\infty} uw \, dx = \text{constant when } \bar{U} \neq 0.$$

4.2.3 Flow over a bell shaped mountain in various regimes

It has now become a standard practice (after Queney,1947) to consider a bell-shaped mountain (Witch of Agnesi) given by

$$h(x)= h_m/(1+x^2/a^2) \qquad (4.2.18)$$

Here h_m is the height of the mountain and a is a scale parameter, commonly known as the

half-width of the mountain. This profile has a simple Fourier transform

$$\tilde{h}(k)=h_m\, e^{-ka}. \qquad (4.2.19)$$

Substituting (4.2.19) into (4.2.9), one can see that parameter $k_0=1/a$ represents the characteristic wavenumber in the solution because waves are rapidly damped when their wavelength falls shorter than $2\pi/k_0=2\pi a$.

For convenience of analysis, the Boussinesq approximation is made in the following, so that $\Gamma=0$, and the Scorer parameter is $l=N/\bar{U}$. Three scale parameters can be identified in the system, they are

$k_s = N/\bar{U} = l$, the Scorer parameter representing the intrinsic vertical scale of the given flow,

$k_f = f/\bar{U}$, the inertial scale of the flow, and

$k_0 = 1/a$, an external scale given as the half width of the bell-shaped mountain that determines the characteristic horizontal wave number in the system.

The dispersion relation (4.2.10) is now simply

$$m^2 = \frac{(k_s^2 - k^2)\, k^2}{k^2 - k_f^2} \quad . \qquad (4.2.20)$$

If N is large (typically of the order $10^{-2}s^{-1}$) relative to f ($\sim 10^{-4}s^{-1}$), five wave regimes can be distinguished (Queney 1948), they are discussed in the following.

a) Potential Flow Regime

When $a \ll \bar{U}/N$, then for characteristic wave number $k \sim k_0$, $k \gg k_s \gg k_f$, so that $m=i\sqrt{k^2 - l^2}$ from (4.2.20), here the positive sign is chosen for the square root to avoid $\eta \to 0$ when $z \to \infty$. The solution is then

$$\eta(x,z) = \left[\frac{\rho_0}{\bar{\rho}}\right]^{1/2} \mathrm{Re} \int_0^{\infty} h_m \exp\left[-ka - \sqrt{(k^2 - l^2)}\, z \right] dk$$
$$= \left[\frac{\rho_0}{\bar{\rho}}\right]^{1/2} \frac{h_m a\,(a+z)}{(a+z)^2 + x^2} \quad . \qquad (4.2.21)$$

The disturbance in this type of flow is evanescent in vertical and symmetric around the mountain peak. Stratification has little effect on the flow and the solution is irrotational, like the solution of a potential flow in a homogeneous fluid. No net work is done by the mountain on the flow, and no energy is transported vertically by the disturbance.

b) Nonhydrostatic Wave Regime

In the case that $a \sim \bar{U}/N = 1/l$, i.e. $k_0 \sim k_s$, rotational effects are usually small, i.e. $k_f \ll k_0$. Therefore

$$m = \sqrt{l^2 - k^2} \qquad \text{when } k^2 \ll l^2,$$

and,
$$m = i\sqrt{k^2 - l^2} \qquad \text{when } k^2 \gg l^2. \qquad (4.2.22)$$

Here the signs of the square roots are chosen to ensure wave energy is directed upwards and be away from the mountain forcing source for the former situation and to remain finite in the non-propagating case.

The evaluation of the integral (4.2.9) is not straight forward in this case. Queney (1947) presented the results using the asymptotic properties of Bessel functions whereas Sawyer (1960) evaluated this by numerical integrations. The far-field characteristics of the waves were discussed by Smith (1979) by employing the asymptotic techniques of the stationary phase. The example solution given by Queney (1947) is reproduced here in Fig.4.1(a), in which $a = \bar{U}/N = 1$km and $h_m = 1$km. The vertical scale (wavelength) of the waves are shown in the figure as related to scale parameter $\bar{U}/N$ to be $L_s = 2\pi\bar{U}/N = 6.28$km.

Fig. 4.1. Waves generated by flow with uniform velocity (U=10m/s) of a uniformly stratified ($N=0.01s^{-1}$) fluid over bell-shaped ridges of various half-widths a [form Queney (1948)]. The mountain profile is given by (4.2.18) and the solutions are based on linear theory. Case (a) is for a=U/N=1km and typifies the nonhydrostatic wave regime. Case (b) is for a=10km and typifies the hydrostatic wave regime in which rotation is not important. Case (c) is for a=U/f=100km and typifies the wave regime in which rotation is important. The upper part of each diagram shows the vertical displacements of air particles, i.e., their trajectories in the vertical plane normal to the ridge. the dashed lines show where the vertical displacement is zero. The scale L_S is defined by $L_S=2\pi U/N$ and is a good measure of the vertical wavelength found in all three cases. The scale L_f is defined by $L_f=2\pi U/|f|$, where f is the Coriolis parameter, which is given the value of $10^{-4}s^{-1}$. The lower panels of (a) and (b) show the ground-level pressure and wind variations associated with the waves. The lower panel of (c) shows a plan view of the particle trajectory and of an isobar at ground level. Amplitudes are based on a maximum height of the ridge of 1km.

A distinguishing feature in this solution is the existence of the "trailing waves" at the upper levels to the lee of the mountain. This is due to the dispersive effect of the nonhydrostatic wave components. A clear physical interpretation in terms of the group velocity can be found in Smith (1979). As can be seen the phase lines tilt upstream, which allows the energy to propagate upwards, but the tilt decreases as we move downstream for shorter waves. The wave amplitude decreases with the height because of

the progressive dispersion of wave energy into a wider horizontal area.

The ground level wind and pressure are also shown in the figure. The wind is a maximum at the crest of the mountain ridge whereas the pressure has a minimum there. The asymmetry in the surface pressure indicates a net force asserted on the mountain, the general formulation of this drag will be given later.

c) Hydrostatic Non-rotational Wave Regime

If $a \gg \bar{U}/N = 1/l$, the mountain is broad compared with the intrinsic vertical scale of the flow, then the flow can be treated as hydrostatic. Given the typical values in the atmosphere, $N=10^{-2}s^{-1}$, $f=10^{-4}s^{-1}$,$\bar{U}=10m/s$, and the mountain half width a=10km, we have $k_0 \ll k_f$, but $k_0 \gg k_f$. This is the case in which the horizontal scale is large for the flow to be hydrostatic but not large enough for rotation to important. In fact this scale is most typical of the mountains in the atmosphere.

In this case we have

$$m = k_s = l \qquad (4.2.23)$$

from relation (4.2.21). The sign here is determined for the same reasons as before. Integral (4.2.9) is readily evaluated in this case for a bell-shaped mountain, which turns out to be

$$\eta(x,z) = \left[\frac{\rho_0}{\bar{\rho}}\right]^{1/2} h_m a \frac{a\cos(l z) - x\sin(l z)}{a^2 + x^2} \quad , \qquad (4.2.24)$$

The corresponding vertical and horizontal velocity are

$$w = \bar{U}\frac{\partial \eta}{\partial x} = \left[\frac{\rho_0}{\bar{\rho}}\right]^{1/2} \bar{U} h_m a \frac{-2ax\cos(l z) - (a^2 - x^2)\sin(l z)}{(a^2 + x^2)^2} \qquad (4.2.25)$$

and

$$u = -\frac{\bar{U}}{\bar{\rho}}\frac{\partial \bar{\rho}\eta}{\partial z} = \bar{U} h_m a \left[\frac{\rho_0}{\bar{\rho}}\right]^{1/2} \frac{(ga / 2R\bar{T} + xl)\cos(l z) - (xg / 2R\bar{T} - al)\sin(l z)}{a^2 + x^2}$$

. (4.2.26)

Solution (4.2.24) shows clearly that the disturbances have a vertical wavelength of $2\pi/l$,

while in the horizontal there is no wave solution and the disturbances decays away from the mountain peak at a rate proportional to 1/k. And due to the scaling by density the wave amplitude grows infinitely large at high levels as the density of the atmosphere approaches zero.

Fig.4.1(b) shows an example solution of (4.2.24) with a=10km, $\bar{U}/N$=1km and h_m=1km, and with Boussinesq approximation made. These mountain waves are hydrostatic and non-dispersive, and have a group velocity component only in the vertical. They are clearly seen in the picture as purely vertically propagating waves and their amplitudes fall off quickly up- and down-stream of the mountain peak. The vertical wavelength is as predicted [see (4.2.24)] $L_s=2\pi\bar{U}/N$ =6.28km and wave amplitudes are constant here without the density scaling (the Boussinesq approximation is made in the solution shown). The figure of the ground level pressure and wind speed shows minimum pressure and maximum wind on the lee slope, indicating a net pressure force acting on the mountain (or in another word a momentum drag acting on the atmosphere) and suggesting a possible explanation for strong downslope winds (Klemp and Lilly 1975).

The net pressure force on the mountain is written as

$$D = \int_{-\infty}^{\infty} p(x, z=0) \frac{dh}{dx} dx \qquad (4.2.27)$$

which can also be expressed in terms of the vertical flux of horizontal momentum in the wave motion,

$$D = \rho(z) \int_{-\infty}^{\infty} u'w' \, dx \; . \qquad (4.2.28)$$

In the hydrostatic wave regime and for a bell-shaped mountain, the drag per unit length of y-direction is calculated to be

$$D = \frac{\pi}{4} \rho_0 N \bar{U} h_m^2 . \qquad (4.2.29)$$

This flux is as seen non-divergent, i.e. constant with height (cf. Eliassen and Palm 1961).

d) Hydrostatic Rotating Wave Regime

This is a case in which $a \sim \bar{U}/f$. i.e. $k_0 \sim k_f$, therefore $k_0 \ll k_s$. The solution is as before given by (4.2.9), but with

$$m = k k_s / \sqrt{k^2 - k_f^2}. \qquad (4.2.30)$$

Fig.4.1(c) shows the solution for $a=\bar{U}/f=100$km after Queney (1948). The wave energy is seen to propagate upward and downwind. The vertical scale is of the order of $\bar{U}$)/N as in the previous cases, whereas the horizontal scale is of the order $\bar{U}/f$. The wave motion is again asymmetric about the mountain peak.

A general formulation of the pressure drag is given in Bretherton (1979), which takes account of both the rotation and the nonhydrostatic effects,

$$D = \pi \rho_0 \int_{|f|/\bar{U}}^{N/\bar{U}} |\tilde{h}(k)|^2 \, [\, (N^2 - \bar{U}^2 k^2)(\bar{U}^2 k^2 - f^2) \,]^{1/2} \, dk \, . \qquad (4.2.31)$$

The lower and upper bounds of the integral reflect that the contribution comes only from vertical propagating wave regimes.

In the hydrostatic rotating wave regime,

$$D = \pi \rho_0 N h_m^2 a^2 \int_{|f|/\bar{U}}^{\infty} (\bar{U}^2 k^2 - f^2)^{1/2} \exp(-2ka) \, dk \qquad (4.2.32)$$

In case (b), i.e. for the nonhydrostatic waves,

$$D = \pi \rho_0 \bar{U}^2 h_m^2 a^2 \int_0^{N/\bar{U}} k \, [\, (N/\bar{U})^2 - k^2 \,]^{1/2} \exp(-2ka) \, dk \qquad (4.2.33)$$

and clearly in non-rotating hydrostatic wave regime formula (4.2.31) gives the same result as equation (4.2.29).

The pressure drag given in formulation (4.2.31) is plotted for a bell-shaped mountain as a function of the half-width a and is shown in Fig.4.2. The drag is seen to increase as a increases up to a limit $\pi/4 \, \rho_0 N \bar{U} h_m^2$, the value for hydrostatic waves, it then falls off with further increase in scale a. i.e. the non-rotating, hydrostatic mountain waves have a maximum drag, with the other parameters being the same.

Fig.4.2. Wave drag per unit span in y-direction on a bell-shaped ridge of the form $h=h_m/[1+(x/L)^2]$. The Brunt-Vaisala frequency N and flow speed U are uniform and the Coriolis parameter f is chosen to have a value of 0.01N (Reproduced from Gill 1984).

e) Quasi-geostrophic Flow Regime

When $a \gg \bar{U}/f$, i.e., $a \sim 10^3$km for typical atmospheric values, the solutions are again evanescent in the vertical. The streamline displacement can be shown to be

$$\eta = \frac{h_m a\,(a + z_s)}{(a+z_s)^2 + x^2} \tag{4.2.34}$$

which is in exactly the same form as that for the potential flow in case (a), except z there is replaced here by z_s, where $z_s \equiv N_z/|f|$. The flow is also symmetric around the mountain peak so that the net pressure drag vanishes.

4.3 Model simulations of linear mountain waves and comparison with analytical solutions

4.3.1 Model set up

The model formulation has been described in the previous chapters (chapter 2 and 3 mainly). As was pointed out in chapter one, the reference state of the model atmosphere is in hydrostatic balance, hence the reference state is, in the absence of baroclinicity, a

function of pressure only. In this σ-coordinate model, the pressure at a σ-level is related to surface pressure, which in turn is dependent through the hydrostatic relation on the (virtual) temperature in the air column directly above. In the presence of irregular orography, the state variables on σ-levels are generally functions of height or pressure. For our experiments the temperature and humidity variables of the initial (or reference) state is specified as a function of height z. To initialize the model, the temperature and humidity are first given an initial guess on the model grid (σ-levels) and then iterations are performed based on the hydrostatic relation until the difference between the values after two consecutive iterations become negligible. A similar initializing procedure to this was used by Anthes and Warner (1978) in their hydrostatic σ-coordinate model.

Different methods have been used in the literature to set up cross-mountain flow. For our mountain wave and orographic convection experiments to be described, the initial flow is directly specified as a function of height, the geopotential height is diagnosed with all initial time tendencies set to zero. The flow is then allowed to evolve as the time integration proceeds and such a starting up procedure is found adequate enough, even in some severe situations (e.g. when the mountain is rather steep) and the initial adjustment seems to be no slower than that using the 'grow-mountain' technique.

4.3.2 Model verification with linear mountain waves: Control experiments

In this section, three control runs of gravity waves forced by a small amplitude bell-shaped mountain with various horizontal scales are described and detailed comparisons are made between the model results and the corresponding analytical solutions that have been discussed in the previous section.

In all of the three runs, the atmosphere is isothermal with T=250K, and a constant wind of U=20m/s. The Brunt-Vaisala frequency N and parameter Γ are therefore constant, given by

$$N^2 = \frac{g^2}{C_p \bar{T}}, \qquad \Gamma = \frac{g}{2R\bar{T}}.$$

In the model runs, we do not make the Boussinesq approximation, but because the contribution from Γ is relatively small, we can still compare qualitatively the model solutions with the example solutions given in section 4.3.1. Table 4.1 summarizes the parameters of the three control experiments.

Table 4.1 Summary of parameters for the control experiments of linear mountain waves in different wave regimes

Experiment	Wave regime	Scale a(km)	h_m(m)	(NX,NS)	Δx(km)	Δt(s)	f(s^{-1})
LMW1	Non-hydro.	2.0	1.0	(257,41)	0.4	3.0	0.0
LMW2	Hydro.,NR	10.0	1.0	(129,41)	2.0	8.0	0.0
LMW3	Rotating,Hydro.	100.0	10.0	(129,41)	20.0	25.0	10^{-4}

The mountain height is chosen so that $h_m/a \ll 1$, the model solutions are therefore effectively linear. Clearly, for experiment LMW1 al ~1, fa/$\bar{U} \ll 1$; for LMW2 al »1, fa/$\bar{U}$)«1; and for LMW3 fa/$\bar{U}$~1, al »1, with the given parameter values so that they fall into the nonhydrostatic, hydrostatic-non-rotating and the rotating hydrostatic wave regimes respectively, and the characteristic wave patterns were shown previously in Fig. 4.1 (a), (b) and (c).

The solutions for these experiments are rather smooth, the conventional leapfrog-centred differencing is accurate enough for the time integration, which is therefore used here for the temperature equation instead of the more expensive FCT scheme. The model domain is (NX-1)Δx by 900mb, with the pressure at the top boundary at p=100mb. 41 (NS) levels are used in vertical with $\Delta\sigma$=1.0/(NS-1). The time step for each run is listed in Table 4.1 and is close to the maximum possible time step under the criterion discussed in section 2.3.

It is seen from table 4.1 that the relation between the Δt used and Δx is not linear, with relatively large time step for small Δx. According to the CFL condition [see

(2.3.12)], the speed of fastest propagating waves in the system is less that 100m/s when Δx=0.4km, whereas for Δx=20.0km, the corresponding speed is slightly greater than 300m/s which is roughly the speed of isothermal acoustic waves. These results confirm the analysis by Miller and White (1984) [(see also Eq.(1.3.7)] which shows that the nonhydrostatic Lamb waves are significantly retarded. When the horizontal grid length is large so that the Lamb wave modes are rendered hydrostatic, their speed then approaches that of the normal sound waves accordingly.

The experiments described includes a weak background diffusion to remove numerical noise with the deformation and Richardson number dependent diffusion having no effect since the Richardson number is also large. These experiments also incorporate a sponge layer from 12km to 18km height with the Rayleigh type damping as described in section 3.3. The damping coefficient profile is as given in (3.3.38) and the e-folding time of damping at the top of the sponge layer (z=18km) is 60s, 300s and 3000s respectively for LMW1, LMW2 and LMW3. It is found this sponge layer effectively simulates the radiative upper boundary condition at a reasonable cost.

The fields from the experiments are plotted on a non-dimensional horizontal scale (X=x/a) from -5 to 10, and are shown at non-dimensional time that is scaled by the advective time scale $a/\bar{U}$. For the display purpose, the fields are multiplied by a certain factor so that they correspond to the linear solutions for a 500m height mountain, the mountain profile shown is also amplified accordingly.

Fig.4.3 depicts the fields of u, w, θ' and θ from LMW1 at several model time. The waves are forced by a narrow ridge with half width a=2km. The solution in the figures shows clearly the typical trailing dispersive nonhydrostatic wave trains to the lee of the mountain, with larger amplitudes higher up. The time sequence of u and w fields signifies the propagation of wave energy in the upwards-downstream direction in the cross section, and the energy flux is clearly convergent at early times until a steady state solution is reached. The solution at T=30 is quasi-steady, the isentrope fields in Fig.4.3(h) displays a wave pattern agreeing very well with the analytical solution in Fig.4.1(a).

Fig.4.3. Fields in x-z plane from experiment LMW1. In (a), (c) and (e) are the perturbation x-velocity u' at non-dimensional time T=tU/a=10, 20 and 30 respectively. In (b), (d) and (f) are the vertical velocity w at T=10, 20 and 30. In (g) the perturbation potential temperature θ' and (h) the total potential temperature θ at T=30. Dimensional parameters a=2km, U=20m/s and $N \approx 10^{-2} s^{-1}$, therefore al ~1, the flow falls into the nonhydrostatic wave regime. The wave pattern depicted in (h) can be compared with the analytical solution of streamline displacement in Fig.4.1(a).

Fig.4.4. As in Fig.4.3 except they are fields for experiment LMW2. In this experiment, the dimensional parameters a=10km, U=20m/s and $N \approx 10^{-2} s^{-1}$, hence al»1 while the Coriolis effect is negligible. The flow is then in the hydrostatic wave regime. The solution shows the mountain waves are non-dispersive, vertically propagating, with phase lines tilting upstream, and have a constant vertical wave length of about 6.6km. The isentropes in (h) are to be compared with the analytical solution in Fig.4.1(b).

Fig.4.5. As in Fig.4.3 except (g) is the field of v, the velocity in y direction and the fields are for experiment LMW3. The mountain is broad in this case with a=100km, the other parameters are U=20m/s, $N \approx 10^{-2} s^{-1}$ and $f=10^{-4} s^{-1}$, hence fa/U~1, a*l* »1, the waves are in the hydrostatic rotating regime. The trailing inertial wave trains to the lee of mountain ridge are evident in the solution. The air trajectories depicted by (h) are to be compared with Fig.4.1.(c).

The solutions of waves in the non-rotating hydrostatic regime from LMW2 are shown in Fig.4.4. The waves are seen in the pictures as pure, vertically propagating, with phase lines tilting upstream. The vertical wavelength is determined from the solution (see e.g. w field at T=30) to be approximately 6.6km, which is rather close to the predicted value $L_z=2\pi/l \approx 6.45$km, given the fact that the model does not make the Boussinesq approximation. The magnitudes of the waves are seen to increase with height, due to the scaling by density. Such an amplification would eventually induce wave breaking at very high levels in the real atmosphere therefore affecting the basic flow. The wave patterns shown in Fig.4.4(h) is to be compared with the streamlines shown in Fig.4.1(b).

The experiment with rotating hydrostatic mountain waves (LMW3) is shown in Fig.4.5. The mountain half-width in this case is 100km. Apart from the vertical propagation of the wave energy as in the pure hydrostatic case, the wave energy is also dispersed downstream due to rotation, generating a trailing wave train downstream of the mountain range. The horizontal wavelength of the inertial oscillation at the downstream surface are shown in the v-field to be again close to the prediction $L_x=2\pi\bar{U}/f\approx 1256$Km. The wave amplitude does not increase with height as much as in LMW2 since much of the wave energy is dispersed downstream. The wave patterns shown by the isentropes in Fig.4.5(h) qualitatively agree with the analytical solution shown in Fig.4.1(c).

The vertical transport of horizontal momentum by the mountain waves is defined in Eq.(4.2.17), and its value is given in (4.2.31). The flux is non-divergent in the vertical for non-dissipating waves as long as the wave amplitudes are small (Eliassen and Palm 1960). We plot in Fig.4.6(a) the profiles of the momentum flux calculated according to (4.2.17) for LMW2, at ND-time from 10 to 50 with an interval of 10. The profile of flux calculated in the same way but using the analytical solution of u and w in Eqs.(4.2.25) and (4.2.26) is also plotted (in bold) and the average of which over one vertical wavelength ($2\pi/l$) is used to normalize the numerical values afore-mentioned. Using this average instead of that directly given by (4.2.29) (although both values are rather close)

will focus any possible discrepancy onto the time integration aspects of the model, without including possible source of error as that due to the Boussinesq approximation and that in the evaluation of integral (4.2.17). The time sequence of profiles in Fig.4.6a shows the flux at higher levels gradually converges towards the analytical value, and reaches about 95% at the height of one vertical wave length (~6.4km) by T=40. A similar converging rate was reported by Durran and Klemp (1983) in their tests with a compressible mountain wave model. In summary, the model solution of linear mountain waves are on the whole very satisfactory, given the fact that the momentum flux is a high order quantity, and is therefore more sensitive to possible inaccuracies.

Fig. 4.6. The profiles of the vertical flux of horizontal momentum transported by hydrostatic mountain waves, at ND-time T=10 to 50 with an interval of 10. The fluxes are normalized by the analytical values shown by the profile in bold. (a) the results from experiment LMW1, in which the mountain waves in hydrostatic regime are simulated using the nonhydrostatic version of model. (b) the results from LMW2, which uses the reduced hydrostatic version of model.

4.3.3 Model verification with linear mountain waves: Sensitivity tests.

a) Direct comparison between analytical and numerical solutions

For the purpose of comparison, the analytical solution of hydrostatic waves over a bell-shaped mountain given in (4.2.25)-(4.2.26) are calculated on the same grid and using the same parameters as in LMW2. The solutions of u' and w are plotted in Fig.4.7 as (a)

and (b). In the same figure, pictures (c) and (d) are the numerical solutions of u' and w from LMW2. The comparison shows the two sets of solution match each other very well, although the maxima and minima in the numerical solution are slightly underestimated. The damping of the upward-propagating wave energy due to numerical diffusion is suspected to be the main source of error.

b) Hydrostatic formulation of model

One of the special features of this model is that it can be easily switched to its hydrostatic version. In the hydrostatic case the vertical acceleration is omitted from the vertical momentum equation which then degenerates to a hydrostatic relation. The elliptic equation (2.1.10) is then redundant and the Φ' is calculated directly from the hydrostatic relation (a ballance between terms two and three on the right hand side of Eq.(2.1.3)). In doing so, the value of Φ' at the lower boundary is obtained in the same way as in the nonhydrostatic version of model, i.e. Φ' at $\sigma=1$ is calculated according to Eq.(2.5.15). For the vertical velocity, $\dot{\sigma}$ is first obtained by integrating the continuity equation in the σ direction and then $\tilde{w}$ is diagnosed from relation (2.1.9). This procedure of solution is similar to the one employed in hydrostatic σ-coordinate models and is considerably simpler than that for the nonhydrostatic version. On the other hand, the time step required by the hydrostatic version of model is usually smaller (especially when the grid length is small) than that required by the nonhydrostatic counterpart because hydrostatic Lamb wave modes propagate at a normal speed of sound. In hydrostic case, averaging of the pressure gradient terms in momentum equations over three time levels of integration can be made which will permit larger time steps. This technique is used by Anthes and Warner (1978) in their hydrostatic σ-coordinate mesoscale model and can be easily implemented in our model. It is not used here since we are performing only a very limited number of experiments using the hydrostatic version.

Fig. 4.7. Fields of u' and w of hydrostatic mountain waves. (a) and (b) are the analytical solutions given by (4.2.25) and (4.2.26). (c) and (d) are solutions from experiment LMW2, and (e), (f) for experiment LMW4.

Experiment LMW4 (see table 4.2 for list of parameters used) is conducted with all others the same as in LMW2, except the hydrostatic version of model is used. The time step is 3s. The u' and w fields at time T=30 are shown in Fig.4.7(e), (f). It can be seen that the difference in the solutions from experiment LMW4 and LMW2 is very small, reflecting that the waves themselves are effectively hydrostatic, and the nonhydrostatic contributions in the model are consistently negligible.

Table 4.2 Summary of parameters in experiments LMW4, LMW5 and LMW6. Hydrostatic version of model is used for LMW4 and LMW5.

Experiment	Wave regime	Scale(km)	h_m(m)	(NX,NS)	Δx(km)	Δt(s)	Model version
LMW4	Hydro.,NR	10.0	1.0	(129,41)	2.0	3.0	Hydro.
LMW5	Non-hydro.	2.0	1.0	(257,41)	0.4	0.5	Hydro.
LMW6	Non-hydro.	2.0	500	(257,41)	0.4	3.0	Non-hydro.

The profiles of the vertical flux of horizontal momentum from LMW4 are plotted in Fig.4.6 (b), which can be compared with those in the left panel (a) for LMW2. It can be seen the profiles of both experiments have a similar convergence rate towards the steady state which has a zero divergence of the horizontal momentum flux in the vertical. The profiles at T=40 for both runs are almost exactly the same.

However when the hydrostatic version of model is used to simulate waves of smaller scales, i.e waves which are nonhydrostatic in nature, they are distorted. Shown in Fig.4.8 are the u', w, θ' and θ fields at T=30 from experiment LMW5, which solves for the steady state for a flow over a narrow mountain just as in experiment LMW1, but using the hydrostatic version of model. Mathematically, making the hydrostatic approximation is to distort the waves by neglecting term k^2 (relative to m^2) in the dispersion relation $k^2+m^2=k_s^2$ [deduced from (4.2.19)] so that $m=l$, which is essentially the dispersion relation for hydrostatic waves. As a result the mountain waves given in the solution are purely vertically propagating. The distortion of the waves are evident in the

numerical solution in that the dispersive wave trains to the lee side visible in the solution from nonhydrostatic calculation LMW1 disappear completely, and the wave energy is forced to propagate completely in vertical, resulting a wave pattern just like that of hydrostatic mountain waves.

Fig.4.8. Fields of u', w, θ' and θ from experiment LMW5, at a nearly steady state. The solutions shown are those of distorted nonhydrostatic mountain waves, due to the use of a hydrostatic model.

Fig. 4.9 shows the vertical flux of horizontal momentum as a function of height from experiments LMW1 (a) and LMW5 (b). It can be seen that the undistorted nonhydrostatic mountain waves transport only three quarters of the horizontal momentum in the vertical (a) as the equivalent hydrostatic mountain waves do. This result is consistent with the analytical result depicted in Fig.4.2. On the other hand, the distorted nonhydrostatic waves transport in an exactly the same way as the hydrostatic waves [compare (b) with Fig.4.6(a)].

Fig. 4.9. The profiles of the vertical flux of horizontal momentum transported by nonhydrostatic mountain waves, at ND-time T=10 to 50 with an interval of 10. The fluxes are normalized by the that for corresponding hydrostatic waves (shown in bold). (a) the results from experiment LMW1, which uses the fully nonhydrostatic version of model. (b) the results from LMW2, which uses the reduced hydrostatic version of model.

c) Mountain waves of finite amplitudes

Experiment LMW1 is re-run but using a 500m height mountain (named as LMW6). With a mountain of such a height, the small amplitude assumption is no longer valid. However, in case that $\bar{U}$ and N are constant and the flow is steady, Long (1953) found that the equation for the streamline displacement is linear in form, which , for a Boussinesq fluid, is

$$\eta_{xx} + \eta_{zz} + N^2/\bar{U}\,\eta = 0 \qquad (4.3.1)$$

This equation appears exactly the same as that for the linear small amplitude wave motion [see Eq.(4.2.2)]. Nevertheless, the lower boundary condition

$$\eta(x,h) = h(x) \qquad (4.3.2)$$

is still nonlinear and is applied at z=h(x). This gives rise to an implicit relation between the boundary condition and the interior solution. Long circumvented this problem by solving (4.3.1) first with a linearized boundary condition and then determine the finite

amplitude mountain profile by solving (4.3.2) for h. The maximum height the mountain thus obtained is lower than the prescribed height, implying that the effective forcing by a mountain in linearized solution is less than the actual nonlinear forcing, i.e. the linearization of lower boundary condition tends to underestimate the height of mountain. Fig.4.10 shows fields at time T=30 of u', w, θ' and θ from LMW6. The linear solution is weaker than the corresponding nonlinear one; in fact, the lowest streamline in the linear solution [see Fig.4.3(h)] cuts through the topography profile, indicating that the air stream is being forced by a mountain lower than the prescribed one.

Fig.4.10. Fields of u', w, θ' and θ form experiment LMW6, at a nearly steady state. The solutions shown are those of finite-amplitude nonhydrostatic mountain waves.

4.4 Large amplitude mountain waves and severe downslope winds

4.4.1 Introduction to severe downslope winds

Severe downslope windstorms are generally related to particular geophysical locations. During the occurrence of such events wave disturbances in an air stream over a mountain range greatly amplify to produce a downslope flow of damaging force. After many years of active research in this area, many insights have been gained on the dynamics of severe downslope winds, but the mechanism of their development is still not thoroughly understood.

One of the best documented and well studied severe downslope windstorms occurred over the Continental Divide of the Rocky Range on 11 January 1972, which is know as the 1972 Boulder Windstorm [Lilly and Zipser (1972), Lilly (1978)]. On this day Boulder, Colorado, experienced one of its most severe downslope windstorms with surface winds gusting as high as 55m/s. Two periods of several hours each contained frequent gusts over 45m/s. Fig. 4.11 [reproduced from Lilly (1978)] shows the isentrope field and the isopleths of constant horizontal velocity observed by instrumented aircraft during the course of the windstorm. The isentropes can be considered equivalent to streamlines as long as dissipation in the wave system is weak. It can be seen clearly from the isentropes in Fig.4.11(a) that the waves are of enormous amplitude - the vertical deflection of isentropes is on the order of 3 times of the maximum mountain height! The oscillating streamlines to the lee of the mountain peak at low levels indicate the presence of trapped waves that are nonhydrostatic in nature. Fig.4.11(b) shows that the horizontal wind has a maximum speed of as high as 60m/s located at about 1km above the lee slope, with the speed on the slope exceeding 50m/s. The picture shows also the presence of a region of nearly stagnant air directly above the lee slope from mid-troposphere to the tropopause, this stagnation region is understood to have been caused by the breaking of greatly amplified waves there.

Fig. 4.11. (a) Isentrope and (b) horizontal wind field observed for the 11 January 1972 Boulder severe windstorm (after Lilly, 1978). The heavy dashed line in (a) is a line separating the observations made a few hours apart.

Many studies have been carried out on this particular event, among them the numerical simulation performed by Peltier and Clark (1979) is particularly worth noting. A two dimensional, nonhydrostatic, nonlinear numerical model formulated in terrain-following coordinates was used in the study. The sounding profile of Grand Junction, Colorado, about 300km west of Boulder at the time of the event was used as the model input [as was used by Klemp and Lilly (1975), (1978)], the potential temperature and wind profiles are depicted in Fig.4.13. The isentrope and u-velocity fields at 8000s of their time dependent simulation are reproduced here in Fig.4.12, they bear a close resemblance to the observed fields - the deflection of isentropes is as large as 5km and the horizontal wind maximum on the lee slope is in excess of 60m/s. Similar results were also obtained by Durran and Klemp (1983) using a 2-D compressible model in terrain-following coordinates.

Fig. 4.12. Results of the nonlinear nonhydrostatic numerical simulation of the Jan. 1972 Boulder severe windstorm from Peltier and Clark (1979). a) Potential temperature contours (interval 5K) and b) horizontal velocity contours (interval 8m/s) at 8000 seconds of simulation. The maximum wind in the lee is in excess of 60m/s.

In spite of the considerable success in reproducing such a spectacular event, a full understanding of the dynamics of severe downslope winds is not a easy task. Klemp and Lilly (1975) proposed, based on linear analyses of hydrostatic waves, that large amplitude waves may result from constructive reinforcement of vertically propagating

modes which are partially reflected owing to variations of stability and winds of the ambient flow. Analysis of the optimal structure for a simple, multi-layer atmosphere emphasize the importance of a low-level stable layer (as that existing in the upstream sounding of the Boulder storm) and indicated the large amplitude waves are generated when the phase shift of the waves across the tropopause is close to one half wavelength. When the sounding profile for the Boulder storm was used as input, a considerably strong response was predicted. The linear approach has the advantage that it can easily accommodate realistic sounding profiles, but its validity is obviously limited by the small amplitude assumption when applied to finite amplitude mountain problems. In fact linear theory can under certain circumstances seriously under-predict the flow response to mountain forcing, even when the mountain height is rather low. One of the numerical experiments of Durran (1986) showed the nonlinear response of an atmosphere with a two-layered structure was 3 times as strong as that of equivalent linear prediction when Nh_m/U was only 0.3.

Given the enormous amplitude of disturbances that are observed, nonlinearity is almost certain to have an important role to play. To explore this aspect, one would either resort to a numerical model or rely on simplified analytical model like that described by Long's equation. Klemp and Lilly (1978) first performed nonlinear simulations of the 1972 Boulder windstorm using a hydrostatic model in isentropic coordinates. A large response was again found in the solution, with maximum surface velocity in the lee reaching 55m/s. However due to the incapability of the model in dealing with isentrope overturning, the simulation did not capture the important stage of amplification subsequent to wave breaking at the tropopause, the wave structure obtained was rather similar to the linear solution in Klemp and Lilly (1975). The crucial role of wave breaking was first identified by Peltier and Clark (1979), who showed through nonlinear, time dependent numerical experiments that, although the surface wave drag is already well in excess of linear prediction, it is the additional nonlinear effects which occur when the wave breaks that transforms the wave fields completely and thereby leads to the formation

of an intense downslope windstorm. The wave breaking occurs in the Boulder case at the level of the first supercritical overturning of isentropes, specifically at the height z_c such that the integral phase shift between it and the ground is $3\pi/2$ in accordance with the WKB theory of linear analysis ($Z_c \approx 11$km in this case, i.e. roughly at the height of tropopause). Peltier and Clark (1979) proposed a mechanism that leads to the amplification after wavebreaking. The region of wave breakdown (where the Richardson number is small) is thought to act as a self-induced critical level that reflects waves incident onto it from below, forming a cavity between it and the ground in which wave disturbances amplify by wave resonance. Clark and Peltier (1984) further explored the resonance hypothesis by studying numerical solutions of mountain waves propagating in an ambient flow that has a pre-specified zero wind line. They found the drag induced by the wave, or in another word the flow response, is a sensitive function of the height of the imposed critical level, with high-drag states occurring in the vicinity of a discrete set of preferred values of critical level height. The selective response is explained as the resonance associated with the total wave reflection from the critical level. This would leads to linear theory singularities at $Z_c m=(1/2+n)\pi$, n=0,1,2, (m being the vertical wavenumber in the flow beneath Z_c), if the reflection is from a 'free' constant pressure boundary with a reflection phase shift of π. The experiments of Clark and Peltier (1984) predicted strong responses at $Z_c m=3\pi/2$ and $7\pi/2$, but weak response at $Z_c m=5\pi/2$. $Z_c m=\pi/2$ was not examined there. The disagreement of the response found for certain Z_c implies an objection to the resonance amplification mechanism. The assumptions on how the waves are reflected also need further justification.

Different from the theory of Klemp and Lilly and that of Clark and Peltier, who all attribute the amplification process to wave resonance associated with the wave reflection in one way or another, Smith (1985) explained this based on steady-state solutions to Long's equation for flow beneath a stagnant well-mixed layer. Smith's results suggested that amplification is possible over the entire range of critical layer heights between (1/4+n) to (3/4+n) vertical wavelength [i.e. $(1/2+2n)\pi \leq Z_c m \leq (3/2+2n)\pi$]. To clarify

this question, Durran and Klemp (1987) performed a set of experiments over a wide range of parameters and found that the response of the flow to changes in the height of mountain and in the height of critical level of zero ambient wind were in good agreement with the nonlinear analytical solution of Smith, but not always consistent with the resonance mechanism by Peltier and Clark. By comparing Smith's solution with shallow water theory Durran and Klemp were able to demonstrate that the strong downslope winds associated with wave overturning are caused by a continuously stratified analog to the transition from subcritical to supercritical flow in the conventional hydraulic theory.

The theory of Smith and the numerical experiments of Durran and Klemp all emphasize the essential ingredient of a well mixed region related to wave breaking. Such wave breaking can either be induced by a pre-existing critical level (environmental critical level) in the ambient flow or be caused by the supercritical overturning of isentropes (self-induced critical level) when forced by a mountain whose maximum height is over a critical value. However, transition from subcritical to supercritical flow can also occur in the absence of wave breaking, when the atmosphere has a layered structure with higher stability in the lower layer and lower stability above. Durran (1986) showed that a set of numerical experiments in which either the depth of lower layer or the height of mountain was varied while keeping the others fixed, produced results which were qualitatively identical to the flow of water over an obstacle. The mechanism of flow transition was found again analogous to the hydraulic jump theory of shallow water, except the role played by the surface gravity waves in the latter case is played by vertically propagating internal waves in the continuously stratified atmosphere. The layer interface plays an analogous role as does the free wave surface. The reduction in static stability above the interface decreases the ability of flow in producing a strong enough pressure gradient force by deflecting the flow interface. When nonlinear advection can not be balanced by the pressure gradient force, the flow would then continue to accelerate on the downslope of the mountain, the transition from subcritical to supercritical flow then occurs.

Durran (1986) simulated the 1972 Boulder windstorm using exactly the same

sounding as Peltier and Clark (1979). The time evolution of the simulated event was very similar to that of Peltier and Clark. Two additional simulations, in one of which the low-level strong stability layer was removed and in the other the stratosphere stability and wind speed were replaced with those at the top of troposphere, identified that the transition from subcritical to supercritical flow at the low-levels in association with the low-level strong stability layer (see sounding in Fig.4.13) was responsible for the nonlinear amplification at the initial stage which induced the wave breaking at the tropopause later on. This amplification mechanism alone was able to produce a surface pressure drag well in excess of the prediction of linear theory while the amplification after wavebreaking was explained in terms of Smith's theory, which is again closely related to the mechanism analogous to the hydraulic jump.

In the section to follow, a simulation of the same Boulder storm will be presented, together with the results of sensitivity experiments. These simulations are carried out for a longer time than those reported by previous authors. A maximum intensity in terms of the downslope wind speed is believed to have been achieved by the wave system during the final phase of our simulations. The surface pressure drag is nearly three times of that at the time when the simulations of previous investigators were terminated (see Fig.4.20 and Fig.4.21). Our simulations suggest that the time evolution of this severe wind storm can be divided into four stages, the waves amplify in the first three stages by different mechanisms until finally the breakdown of the whole wave system occurs due to the on-setting of Kelvin-Holmholtz type instability.

4.4.2 Numerical simulations of the 11 January Boulder severe windstorm: Time evolution and mechanism of amplification

The upstream sounding used to initialize the model is the same as that used in Peltier and Clark (1979). It is the sounding taken at Grand Junction, upstream of Boulder on 11 January 1972. The profiles of the potential temperature and the wind normal to mountain ridge are plotted in Fig. 4.13, together with the profiles of the Brunt-Vaisala frequency

and the Scorer parameter calculated for the given sounding. The atmospheric structure is characterized by an unusually strong upper tropospheric jet and a relatively weak static stability, with a layer of high stability (isothermal) sitting just over the mountain peak. The profile of the Scorer parameter shows a rapid decrease from the ground level upwards to much smaller values above 4km height, except for an increase in the layer of strong stability. In an atmosphere with the given structure, short waves can not propagate to high levels and tend to be trapped at low levels to form lee waves. For longer hydrostatic mountain waves, this atmosphere will produce a phase shift of 3/4 vertical wavelength across the depth of troposphere. The first overturning of isentropes or streamlines will then occur at the tropopause, that is at a height of about 10km above the ground, provided that the air flow is sufficiently forced at the ground level.

Fig. 4.13. Upstream potential temperature (a) and wind (b) profiles for the 11 Jan. 1972 Boulder windstorm. In (c) and (d) are respectively the Brunt-Vaisala frequency and the Scorer parameter squared corresponding to the given sounding.

The control simulation of the Boulder Severe Windstorm is named as SDW1. It uses 193 points in horizontal with grid length Δx=1km, and 41 levels in the vertical with p_{surf}=850HPa and p_{top}=30HPa. The 850HPa surface pressure is chosen to roughly match the ground level pressure to the east of the mountain ridge, the Continental Divide of the Rocky mountains. The time step Δt used is 4s. Following previous investigators, a symmetric bell-shaped mountain ($h(x)=h_m/[1+(x/a)^2]$) with half-width a=10km is used (the solution should not be very sensitive to the upstream topography profile since the actual upstream flow below the level of mountain peak is to a certain degree blocked) and is located at the centre of the model domain. The maximum mountain height h_m is 2km. The top of the model domain (30HPa constant pressure surface) is about 22km above the ground level, from which a sponge layer extends down to 15km height. The Rayleigh type damping described in section 3.3.4 is employed within this sponge layer, with the shortest e-folding time of damping being 5 minutes at the top of the domain. A full formulation of turbulence mixing with the deformation and Richardson number dependent mixing coefficients is used (see section 3.3). The eddy Prantl number $P_r=K_m/K_H$ is assumed to one where K_m and K_H are respectively the mixing coefficient for momentum and heat. Therefore $K_H=K_m$ and the turbulent mixing is invoked when the Richardson number falls below one, i.e. when $R_i \leq 1$. The starting up procedure of the model simulation is the same as that used for linear gravity wave experiments described in section 4.2, that is, the initial state (the temperature and wind) is specified as a function of height or pressure based on the hydrostatic relation, and then the model atmosphere is allowed to evolve from this state. Radiative conditions are applied on the lateral boundaries, together with a mass flux adjustment procedure as described in chapter 2.

Fig.4.14. The isentrope fields at various time of the model simulations of the 11 Jan. 1972, Boulder severe downslope windstorm.

Fig.4.15. As in Fig.4.14, but at later time of the simulation. The fields show a continuous acceleration of the downslope flow and an increase in the steepness of the flow jump. The isentrope field at 240 min is to be compared with both the observation (Fig.4.11a) and the theoretical results of Smith (Fig.4.22).

Fig.4.16. The fields of horizontal velocity at various time of the simulation of the Boulder windstorm.

Fig.4.17. As in Fig.4.16, but at later time. The fields show the maximum horizontal winds descend gradually down to the surface and to the foot of the lee slope, exceeding 72 m/s at 420 minutes.

Fig. 4.18. The perturbation horizontal velocity (deviation from the upstream) fields. The pattern (e.g. at 180 min) indicates the presence of interaction between the upward propagating and the downward reflected wave components (cf. Fig.4.24).

Fig.4.19. The fields of the vertical velocity. The establishment of the trapped waves below the breaking tropopause is most evident in these fields.

Since the turbulence parameterization is in effect only in regions of low Richardson number, a weak constant background diffusion is found necessary to remove small scale roughness in the highly nonlinear flow. This background diffusion, as was discussed before, operates only on the deviations from the initial state, it therefore helps to maintain the ambient flow to a certain extent. The coefficient of background diffusion $K_{BG}=200m^2/s$ is used for control run SDW1.

Unlike in the previous studies (Peltier and Clark 1979, and Durran 1987), our time dependent simulation is extended to the point where the waves in the entire troposphere are amplified to a maximum intensity and start to breakdown; this does not happen until over 7 hours of model integration. Shown in Fig. 4.14 and 4.15 are the isentrope fields at various time of simulation, and in Fig. 4.16 and 4.17 are the fields of horizontal velocity. The deviation of horizontal velocity from its upstream value (u') is contoured in Fig. 4.18, and the vertical velocity w in Fig. 4.19. The time evolution of the surface pressure drag [defined in (4.2.17)] is depicted in Fig.4.20, in which the dashed line is the drag for linear mountain waves evaluated at the surface. The time evolution of the maximum surface u-velocity is also shown in the same figure.

It will be seen that the evolution of the simulated wave system can be divided into four phases or stages. They are 1) the initial amplification stage due to low-level flow transition, 2) the stage of amplification of the disturbances in the entire tropospheric flow following the wave breaking at the tropopause directly over the mountain, 3) the stage of further amplification until the wave disturbances reach a full strength, together with the occurrence of successive wave breaking at the tropopause downstream and the formation of deep trapped lee waves, 4) finally the stage of breakdown of the entire tropospheric wave system. These stages are cleared reflected in the evolution of both the pressure drag and maximum wind speed at the surface (Fig. 4.20). The time evolutions of the surface pressure drag reported by Peltier and Clark (1979) (dashed line) and by Durran (1987) (solid line) are shown in Fig.4.21. It can be seen that the magnitudes of drag obtained in three different simulations agree fairly well within the period in which the results from all the three are available.

Fig.4.20. The time evolution of (a) the surface pressure drag (10^6 kg/s^2) and (b) the maximum horizontal velocity at the surface, for the simulation (LMW1) of the 1971 Boulder windstorm .

Fig.4.21. The time evolution of the surface pressure drag obtained by Peltier and Clark (dashed line) and by Durran (solid line) in their simulations of the 1971 Boulder windstorm, [picture reproduce from Durran (1987)].

As is recognized by Durran (1987), the initial stage of amplification manifests itself as the transition from a subcritical to a supercritical state of the flow immediately above the mountain top level. During this period, the interface between the layer of strong stability and the layer of weaker stability higher up plays a crucial role. This stage of low

level flow transition is evident in the flow patterns shown in Fig. 4.14 and covers the initial 1.5 hours of integration. The flow at lower levels, when passing the mountain peak, continues to be accelerated downslope to reach a maximum speed 36 m/s at about one third the maximum mountain height (see u field at t=90mins in Fig. 4.16). This state is in fact established rather quickly (whin the initial one hour) and the resultant surface pressure drag is nearly three times that of linear waves. The flow amplification at the low levels is very important, it is this process that provides the necessary low level forcing that is required to induce the wave breaking at the tropopause (note that the vertical flux of wave energy is proportional to the pressure drag / momentum flux at the surface, this was discussed in section 4.2.2). Negative values of u-velocity have appeared by 90 minutes over the mountain peak at about 10km height, correspondingly the isentropes display a flow overturning at that level. Durran (1987) has shown that this upper-level flow overturning can not occur if the strong stability layer at the lower levels is removed. Initially the vertical velocity maximum is associated with the low level flow jump, but at 90 minutes it is shifted to 8km height level to be related to the deepening waves there.

By 120 minutes, the flow has changed into another flow regime (stage two of the development) in which the entire air stream beneath the expanding wave breaking region starts to accelerate over the lee slope of the mountain. The role played by the flow interface in connection with the low level flow transition now gives place to the one between the well-mixed air at the upper levels and the laminar flow underneath it. The change in the low level flow pattern is particularly evident by comparing the u-field at t=90 and t=120 minutes. The change is signified by the disappearance at t=120mins of the flow transition on the lee slope and the shift in position of the maximum surface wind (Figs. 4.16d and 4.18b), which is now at about 2/3 the height of the mountain peak, rather than the 1/3 at 90mins.

Fig. 4.20 shows that the wind and pressure drag at the surface increase rapidly during the first half of the second stage (from 90mins to 240mins). They reach their local peak values at about 3 hours and then level off slightly to a temporary minimum at 4

hours, indicting the point where the the third amplification phase begins. The time dependence of the surface pressure drag as well as its magnitude predicted by our model during the early stages agrees very well with both the result of Peltier and Clark (1979) and that of Durran and Klemp (1983). The former also recognized the different stages of development, only they offered a different explanation. However the simulations described in both papers all stopped at about 2.5 hours of integration, presumably under the assumption that a maximum amplitude had been reached by the wave system. Our extended simulation shows clearly that the wave system at the time of 2.5 hours is far from being mature, i.e. being at its maximum amplitude. In fact, the wave drag triples once more during the following 5 hours of development, reaching a value that is one order of magnitude greater than that of linear mountain waves (3.8×10^6 kg/s^2 versus 3.04×10^5 kg/s^2). This value is however very close to the drag (4.136×10^6 kg/s^2) obtained by Smith (1985) for the nonlinear solution to Long's equation depicted in Fig.4.22.

As was discussed in the earlier introduction, Smith's theory based on Long's equation explains the severe downslope winds as a result of the flow transition to a supercritical state in the presence of a well mixed stagnant region. It will be seen that this mechanism is well supported by our numerical simulations. During stage three of the development in simulation SDW1 which covers approximately the period from hour 4 to 7, the surface wind and pressure drag exhibit a linear increase with time. The isentropes over the mountain are increasingly deflected downwards - the one originating at 10 km height is now as low as 4 km above ground level. The entire tropospheric air is now channelled into the layer of less than 4 km deep, and is accelerated right down to the mountain foot at the end of this development phase. The flow pattern depicted by the isentropes at t=420mins can be compared with the nonlinear solution of Smith in Fig. 4.22. The resemblance between them in the transition part of the flow is striking although the hydrolic jump is not present in Smith's solution. The limitations of Smith's solution will be discussed later. Our solution shows that while the surface supercritical flow pushed its way ahead towards the mountain foot, the jumping flow becomes increasingly

upright and the vertical velocity inside the jump also increases greatly, which implies that the isentropes become more and more vertically oriented and the wind shear is getting stronger. As a result the dynamical stability in the jump flow is significantly reduced. The onset of the dynamical instability is evident already at t=390 as shown in the isentrope fields , and is even more clear at t=450. The slope of isentropes in the jump flow has a direct relevance to the low level flow too, since as soon as the overturning of these isentropes occurs, the hydrostatic pressure gradient associated with the sloping isentropes vanishes. The resulting situation is then obvious - the deep wave system quickly breaks down as the flow becomes convective unstable, and this is what happened after 450mins in the model simulation. Fig. 4.20 shows a even more rapid increase in the maximum surface wind speed after 420mins whereas the increase in the pressure drag slows down. Therefore we call the period after 420mins a final stage of wave breakdown. The maximum surface wind speed at the end of stage three is about 80m/s, again very close to the value in Smith's solution (83m/s, see Fig.4.22).

Fig. 4.22. Nonlinear steady state solution to Long's equations obtained by Smith (1985) for a case in which U=20m/s, N=0.01s^{-1},h_m=1km. The solution shows the air flow beneath a well mixed region transitions from a subcritical flow to supercritical flow across the mountain ridge, such that the flow continues to accelerate greatly downslope to reach a maximum speed at the mountain foot.

Smith's theory also has certain limitations. It does not give us the time evolution of the amplification processes, nor does it predict the behaviour of the supercritical flow downstream. The nonhydrostatic effects are not taken into account either in Smith's theory, which in reality may cause a significant amount of wave energy dispersion away from the mountain forcing. Our simulation has shown that the flow jump does occur and it occurs rather quickly, typically before the downslope flow reaches the foot of mountain. In contrast to the case in which the flow transition is caused by an uniform flow interface at a given level (e.g. the case of shallow water or layered atmosphere), the position of the flow jump is closely linked to or interlocked with the right edge of the upper level wavebreaking region - the low level flow acceleration stops at the point where the hydrostatic pressure gradient force produced by the upper level flow interface reverses direction. As a result, the jump is seen to migrate gradually down slope toward the mountain foot as the area of upper level wave breaking progressively expands. A series of waves are indeed triggered downstream by the jump flow, and the amplification of them induces further wave breaking at the tropopause, which turn the tropopause into an effective reflecting lid. A resonant wave train then forms between the tropopause and the ground, which clearly has a tendency of propagating infinitely downstream. This implies a considerable amount of wave energy is being transported downstream by these waves, essentially through nonhydrostatic dispersion. The relative importance of its impact on the flow amplification on the lee slope, however, still needs quantifying before a thorough understanding is obtained.

On the other hand, the simulated disturbances can also to a certain degree be interpreted in terms of the internal gravity waves that develop in a spatially varying medium - a flow that has spatial variations in speed and stratification, and may also contain critical lines away from which the impinging waves will be reflected. The areas of waves breaking in the simulated system form such a line of reflection, which is called by Peltier and Clark the self-induced critical line. The ray-tracing technique is very helpful in understanding the behaviour of waves in such a varying medium.

The propagation of the wave energy and the reflection of the energy at the reflection level are schematically illustrated in Fig.4.23. In the figure, C_{gx} and C_{gz} represent the horizontal and vertical component of the group velocity respectively.

When the wave is initiated at the mountain forcing source (x=0, z=0 in the figure), it propagates in both the vertical and the horizontal direction. The latter occurs because of the nonhydrostatic effects. As the wave propagates upwards into a region of well mixed air where both the static stability and the flow speed are nearly zero, it can no longer propagate further upwards and is reflected downwards. Assume the horizontal group velocity is little changed during the process while the vertical group velocity decreases gradually as the wave approaches the reflection level, the energy ray of the wave can then be sketched as in Fig.4.23. When the reflected wave hits the ground, it is reflected upwards again. If the wave energy is little lost in the reflective processes, it will carry on propagating downstream between the cavity formed between the ground and the reflection level.

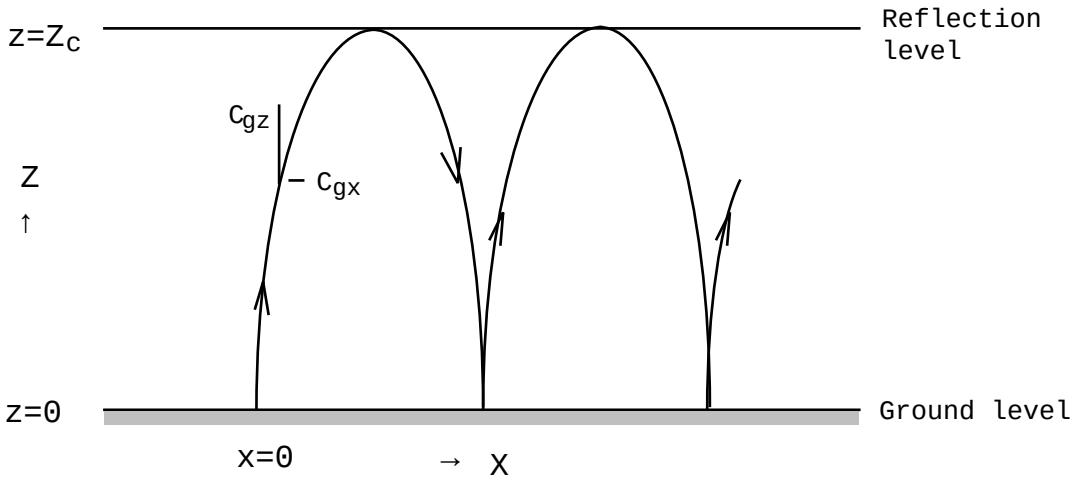

Fig. 4.23. A schematic illustration of the ray of energy showing the propagation of nonhydrostatic gravity waves in an atmosphere containing a reflective line.

The downstream propagation of the wave energy in the way illustrated above is

evident in the model solution (e.g. the u, or u', w and θ fields at t=420mins). This process on the one hand would cause leakage of wave energy downstream of the mountain, presumably slowing down the amplification of the disturbances on the mountain slope; on the other hand, the interaction between the upward and downward waves can cause enhancement or cancellation of disturbances in certain regions.

The positive and negative anomalies in the field of horizontal velocity perturbation u' (see u' field at t=180mins in Fig.4.18) show clear evidence of the interactions (or wave interference). The presence of downward fluxes of wave energy is also implied by the downstream titling of phase lines indicated by the positive anomalies in the w fields. To further demonstrate the presence of such wave interactions in the model solutions, we construct a field by super-positioning two solutions of the hydrostatic mountain waves propagating in opposite directions. It is written as [see the hydrostatic mountain wave solutions in (4.2.25) and (4.2.26), and they are given in the following in a nondimensional space; x is scaled by mountain half width a, z by vertical wavelength L_z, u' scaled by $Uh_m a$ and w by $Nh_m a$],

$$u = u^{+} + r\,u^{-} = \frac{(x-x_1)\cos(2\pi z)+\sin(2\pi z)}{1+(x-x_1)^2} + r\,\frac{(x-x_2)\cos[2\pi(z_c-z)]+\sin[2\pi(z_c-z)]}{1+(x-x_2)^2} \tag{4.4.1}$$

and

$$w = w^{+} + r\,w^{-} = -\frac{2(x-x_1)\cos(2\pi z) + [1-(x-x_1)^2]\sin(2\pi z)}{[\,1+(x-x_1)^2\,]^2} - r\,\frac{2(x-x_2)\cos[\,2\pi(\,z_c-z)] + [1-(x-x_2)^2]\sin[\,2\pi(\,z_c-z)]}{[\,1+(x-x_2)^2\,]^2} \tag{4.4.2}$$

where z_c is the height at which the upward propagating waves are reflected.

u^+, w^+ and u^-, w^- are respectively the solutions of the upward and downward propagating hydrostatic gravity waves centred at $x=x_1$ or x_2, where x_1 and x_2 are constant horizontal coordinates. In order to mimic the dispersive effects that are not included in the simple hydrostatic solutions, we modify the solutions by shifting the horizontal

coordinates x_1 and x_2, so as to reflect the bending of energy ray in the varying medium. A parabolic trajectory of energy ray is assumed, therefore

$$x_1 = d\,[\,1 - \sqrt{1 - z/z_c}\,], \qquad x_2 = d\,[\,1 + \sqrt{1 - z/z_c}\,].$$

Where 2d is equal to the distance between the two branches of energy ray at ground level (see the illustration in Fig.4.23), and r is the reflection index. The origin of the frame of reference is located at the centre of the mountain base line.

Choosing the level of the reflection at z_c=3/4, i.e. at a height of three quarters the vertical wavelength, the downstream shift distance 2d=2.0, and assuming the reflection index r=1, we plot the constructed fields of u and w in Fig.4.24.

Fig.4.24. The constructed wave fields. (a) horizontal velocity given by (4.4.1) and (b) the vertical velocity given by (4.4.2).

The wave pattern in the constructed solution fits nicely with the pattern in the model solution (e.g. the u' and w fields at t=180mins), in particular at the lower levels. The solutions near the reflection level can not be expected to compare much better, since the waves there in the model solution are already broken. Particularly worth noticing in the constructed solutions are the large anomalies directly over the mountain lee slope, which closely resembles those in the the model solution. It is therefore suggested that before the wave disturbances attain a large amplitude, the mechanism of the critical layer reflection

and resonant growth advocated by Peltier and Clark does seem to be feasible, but when the wave amplitude is very large, it becomes hard to interpret the solution in terms of linear arguments. Since the basic state would have been greatly modified by the wave disturbances the linear arguments have only local meaning by then. The effect of the downward wave energy fluxes on the downslope winds is difficult to generalize. In fact at time t=240mins of the model simulation, the downward energy fluxes are at a peak in association with the appearance of the first secondary wave breaking at the tropopause (compare the θ and u' fields at 240mins to those 180mins), the corresponding vertical velocity perturbation is however weaker than at t=180mins, the surface pressure drag and wind speed are also at a minimum at this time, indicating the wave disturbances on the downslope are weakened rather than enhanced by the downward wave energy fluxes. The curve of the surface maximum wind in Fig.4.20 shows two more nearly periodic oscillations at later times, these seems to be also related to the wave interactions between the upward and downward components. But at the later times, the contributions from them are no longer large enough as to alter the trend of the downslope wind amplification.

In summary, the 11 January 1972 Boulder severe downslope windstorm is simulated using a nonhydrostatic sigma-coordinate model. The initial development agrees remarkably well with the results of previous investigators. Moreover, our simulation is extended to the stages of flow development that are beyond the effective influence of the explicit downward reflected waves. It is these further results that demonstrate to a full extent the mechanism of flow amplification. The amplification is clearly seen as the result of the fully nonlinear transition of the flow in the entire troposphere, from a subcritical state into a supercritical state after a well mixed stagnant region is produced by wavebreaking. The final flow pattern is very similar to the steady state solution of Smith (1985) and is very close to the observed pattern too. The downslope flow exhibited a tendency of continuous acceleration until it reached the mountain foot. The model simulations ended with the onset of a dynamical instability in the entire wave system and consequently the violation to the CFL condition. The maximum surface wave speed at the ending phase was as high as 80m/s which is obviously higher than the observed value.

This is most probably due to the absence of a proper parameterization of the surface frictional drag. Had such a parameterization been included, a steady state may be obtained when there is a balance between the flow acceleration and the surface friction. The possible unsteadiness of the upstream flow may also be part of the reasons that the observed downslope winds were weaker than the simulated ones.

The interaction between the primary upward propagating mountain waves and the downward reflected components is also evident in the numerical solution. However due to the presence of strong nonlinearity and the significant changes in the basic conditions by these large amplitude wave disturbances, the role of the interaction is rather difficult to generalize. We would rather consider this to be of only secondary importance to the development of the severe downslope winds, especially at the later stages.

A number of sensitivity experiments were also carried out. They include increasing the spatial resolution, decreasing the integration time step, re-positioning the lateral boundaries relative to the mountain, altering the top boundary pressure or reducing the background diffusion. None of these was found to produce fundamental changes to the overall time evolution of the windstorm. Four stages of development are well simulated in all of these experiments, though the timing of the development may vary slightly, due to e.g. the change in the amount of background diffusion present. These results lead us to a conclusion that the development of the severe downslope wind is a deterministic feature of the given upstream sounding.

4.5 Trapped mountain waves: Dry and moist lee waves

4.5.1 Introduction to trapped lee waves

Mountain lee waves are gravity waves that are trapped in the low levels due to the variations in the vertical atmospheric structure (wind and/or stratification). As it is easier for longer waves to propagate vertically, these trapped waves are generally of smaller scales and are mostly nonhydrostatic. The problem of mountain lee waves has been a subject of extensive studies for many years. According to linear theory, the character of the mountain gravity waves are principally governed by the size and shape of the mountain, and the Scorer parameter

$$l^2 = \frac{N^2}{U^2} - \frac{U_{zz}}{U}. \qquad (4.5.1)$$

Here N is the Brunt-Vaisala frequency, and U is the mean cross mountain wind speed. As was discussed in section 4.2, the Scorer parameter determines the maximum horizontal wavelength at which steady linear gravity waves can propagate in the vertical. Scorer (1949) found that if l decreases with height, there will be a range of wavenumbers over which standing gravity waves can have wavy solutions in the vertical only near the ground. If this decrease is abrupt and sufficiently large, one or more resonant waves can develop in the lower atmosphere. These waves - called trapped lee waves, can propagate infinitely far downstream of the ridge. In the absence of friction, they can produce strong rotors and destructive winds along the lee slope of the ridge. In a moist atmosphere, cloud streets can form due to the wave motion, and unstable convection can also be triggered by these waves, some times at places far downstream of the mountain forcing.

The simplest structure of atmosphere that supports trapped waves consists of two layers, with the Scorer parameter l being constant in each one. In his classical paper on lee waves, Scorer (1949) provided the solution of the resonant (trapped) waves in such a two-layered atmosphere together with the conditions for such a solution to exist. Let l_1 and l_2 be the Scorer parameter in the upper and lower layer respectively and H the depth

of the lower layer. Scorer showed the linear resonant waves can exist in the lower layer whenever

$$l_1^2 - l_2^2 \geq \pi^2/4H^2. \qquad (4.5.2)$$

This is the condition that non-trivial solutions of the linear equations of motion exist with homogeneous boundary conditions. This condition is obviously more easy to satisfy with a large difference of Scorer parameter in the two layers and with a deeper low layer.

The resonant horizontal wavenumber k satisfies equation

$$\mathrm{Tan}(\lambda_1 H) = i\,\lambda_1/\lambda_2, \qquad (4.5.2)$$

Where $\lambda_1 = \sqrt{l_1^2 - k^2}$, $\lambda_2 = \sqrt{l_2^2 - k^2}$.

When the lower layer is sufficiently deep, multiple solutions to (4.5.2) may exist that correspond to different horizontal wavenumbers. Scorer showed that in such a case the longest wave number will dominate the solution.

For a flow over a 2-D bell-shaped ridge given by $h(x)=h_m/[1+(x/a)^2]$, the streamline displacement due to a single Fourier component of the mountain waves is given by Scorer as

$$\eta(z) = -2\pi h_m a\, e^{-ka}\,\frac{U(0)}{U(z)}\,\Psi_k(z)/\frac{\partial \Psi_k(0)}{\partial k}\,\sin(kx) \qquad (4.5.4)$$

where U(z) is the mean horizontal wind speed, and function $\Psi(z)$ satisfies equation

$$\partial^2\Psi/\partial^2 z + (l^2 - k^2) = 0.$$

Clearly the waves amplitude depends on several factors such as the mountain height and width, the stratification and mean flow speed. The relative importance of the these factors were discussed by Corby and Wallington (1956) in terms of the maximum vertical velocity in the lee waves developed in a two layer atmosphere.

In most situations, qualitative understanding can be obtained on the development of lee waves based on the above linear theory. However realistic atmospheric structures are usually much more complicated, the effects of nonlinearity and moisture condensation can

not be easily included in the analytical models. Durran and Klemp (1982) studied the effects of moisture on trapped mountain waves using a numerical model. They found that the moisture affects the behaviour of lee waves mainly by changing the effective static stability so as to change the trapping condition of the atmosphere. Lee waves can also be destroyed through the destabilization in the process of condensation.

Lee waves and the associated lee wave clouds are very common phenomena in the western mountainous areas of the British Isles. Distinct cloud patterns prevailing hundreds of kilometres downstream of certain mountain ridges are frequently observed from satellite pictures. Two of such cases are selected for our modeling studies. The satellite pictures showing the lee wave cloud patterns of these two cases are displayed in Fig.4.25. The time and dates for the cases are respectively the 14:34 GMT, 20 April 1984 (Case A) and 13:37 GMT, 8 March 1985 (Case B).

In both cases, the satellite pictures display very clear wavy cloud patterns covering almost the whole of Ireland and Scotland. The cloud streets lie roughly NW to SW, while the prevailing winds at the time were mainly southwesterlies, normal to the observed cloud streets. Furthermore, both pictures show clear-cut edges of the wavy clouds, coincident with the west and southwest coast of Ireland, indicating that the moist, maritime air flow was being forced by the hills along the coast. Short waves formed in the low-level stable layer are trapped and propagate to the lee of these hills, and are presumably reinforced by the hills further downstream.

The atmospheric conditions at the corresponding time are represented by the sounding profiles taken at 12Z, 20/4/84, Valentia and 12Z, 8/3/85 Valentia (as marked in the pictures) respectively for the two cases. The slightly modified version of these soundings is given in Fig.4.26 and Fig.4.27. The presence of a low-level stable layer is a common feature of these soundings. In Case A, the stable layer extends to the ground surface, while in Case B the layer of a very strong stability (an inversion in fact) is located above a well mixed surface boundary layer. The atmosphere above these stable layers has a much weaker stratification, the θ profiles are in fact close to the moist adiabats.

Fig.4.25. The visible satellite images showing the lee wave patterns over the British Isles at (a) 14:34 GMT, 20 April 1984, and (b) 13:37, 8 March 1985. Numerical experiments of lee waves will be presented which use the 12Z soundings of the Valentia upper air station (marked by bold cross in the map) to specify the environmental conditions.

Fig.4.26. Vertical profiles of (a) the potential and equivalent potential temperature, (b) the cross mountain wind speed (c) the Brunt-Vaisala frequency, and (d) the Scorer parameter, derived from the 12Z, 20/4/84, Valentia sounding for Case A.

The profiles of the Scorer parameter are plotted in picture (d) of each figure. For Case A, the Scorer parameter decreases almost linearly from the ground level upwards and remains roughly at a small constant value between 4 to 10 km height. Fig.4.27d shows for Case B a large value of Scorer parameter in a shallow layer between 1 to 2 km height., corresponding to a layer of strong inversion there, but above and below this layer the parameter is much smaller. In this case, the short waves will be expected to be confined mainly to the inversion layer - which essentially acts as an effective wave guide! In the following sections, the numerical experiments with the given atmospheric conditions will be presented.

Fig.4.27. As in Fig.4.26, but they are derived from the 12Z, 8/3/85 Valentia sounding for Case B.

4.5.2 Case A: Lee wave experiments with the 20/4/84, Valentia upper air sounding

a) Dry and moist lee waves forced by a single ridge

The potential temperature and wind profiles derived from the 20/4/84, Valentia sounding shown in Fig.4.26 are used to initialize the model atmosphere, in order to simulate the lee waves that occurred on that day over the western parts of the British Isle. But due to the lack of detailed observations, we do not attempt to simulate every aspects of the actual waves, rather we use only idealized (the bell-shaped) mountain profiles while directing our attention to the general lee wave dynamics as to the effects of moisture condensation and the mountain size, etc. on the lee wave development. Table 4.3 provides a list of experiments to be described in this subsection.

Table 4.3 Lee Wave Experiments (LWE) with the sounding of Case A

Experiment	Mountain Scale(km)	Height(km)	(NX,NS)	Δx(km)	Δt(s)	Dry/Moist
LWE1A	3.0	0.5	(257,41)	0.5	4.0	Dry
LWE1B	"	"	"	"	"	Moist
LWE2A	"	1.0	"	"	"	Dry
LWE2B	"	"	"	"	"	Moist

Other parameters used are P_{surf}=1013.25HPa, P_{top}=100HPa. The upper sponge layer is from 12 to 16 km height. In the moist runs, only cloud water is included and is kept in the flow while it is advected, the condensation is therefore reversible. The Flux-Corrected Transport scheme is used only to advect the cloud water. A weak background diffusion is included and the coefficient is 1.0 m^2/s for the lower mountain runs, and 10.0 m^2/s for the higher mountain runs. The deformation and Richardson number dependent turbulence mixing will be switched on where appropriate.

The fields of the vertical velocity w and the isentropes at t=60mins and 180mins of the dry lee wave experiment LWE1A are shown in Fig.4.28. The simulated waves are mostly trapped in the lower 4 km layer, in which the Scorer parameter is large but decreases rapidly with height. The wave disturbances are seen to propagate gradually downstream with time to establish a steady, regularly spaced lee wave pattern. The horizontal wavelength is about 12.57 km, corresponding to a wavenumber of k=0.50 km^{-1}. This wavenumber is between the value of l at z=0 km (l =1.12 km^{-1}) and that at z=4km (l =0.38 km^{-1}), consistent with the prediction of Scorer's theory in the case of a two-layered atmosphere. The vertical velocity maxima are at about 2.5 km height, that is roughly at the top of the low-level stable layer. The wave disturbances decay almost exponentially above this level of maxima. The magnitude of the vertical velocity is about 3m/s and is nearly constant all the way downstream, indicating there is little energy lose in the trapping layer.

Fig.4.28. Fields of vertical velocity w (a),(c), and of isentropes (b),(d) obtained in lee wave experiment LWE1A, at 60 and 180 minutes of model simulation.

Fig.4.29. Fields of vertical velocity w (a) and of isentropes (b) at 180mins of the lee wave experiment LWE1B (the moist run of LWE1A).

Given the half-width of the ridge of 3km, the dominant wavenumbers forced by the ridge are around $k=1/a\approx 0.33$ km^{-1}. This value is lower than the Scorer parameter in the mid-levels, therefore a considerable number of wave components can propagate into high levels. The longer propagating waves are readily visible directly over the ridge in the

model solution (see e.g. the w field at t=180 mins).

According to Scorer's linear theory, the wavelength of the trapped waves are solely determined by the vertical structure of the atmosphere. The role of the mountain is to provide a sufficient forcing of the trapped wave components. This suggests that ridges of smaller scales can be more effective in generating lee waves than broad smooth mountains, although the latter can be rather high. This also lends support to our use of a very simple mountain profile in our lee wave simulations. Finally we can see the simulated wave pattern and the wavelength agree rather well with those shown by the lee wave clouds in the satellite picture.

In experiment LWE1A, the mountain ridge is not high relative to the vertical scale height of the flow. The Froude number $Fr=h_m l$ ranges from 0.19 to 0.56 in the troposphere, with the higher values at the lower levels. Therefore wave overturning would not occur within the troposphere.

In experiment LWE2A, a higher mountain with h_m=1km is used. The w and θ fields at t=180mins are shown in Fig.4.31 (the mountain in now placed at 48 km from the left boundary). Compared with the corresponding fields of LWE1A in Fig.4.28, the wave amplitudes are slightly more than doubled in LWE2A, with the maximum vertical velocity being still at the same level. The Froude number in this case is higher than the critical value for overturning in the low-level flow, but this stable layer is not deep enough for the wave overturning to occur within it. The overturning would also not occur in the upper troposphere where the Froude number is much lower. The crests of the trapped waves are no longer evenly spaced in the model solution, this is most probably due to the interaction between the trapped waves and the longer, propagating waves higher up. The average wavelength of the lee waves is about 13.6 km, longer than that obtained in LWE1A, this difference can be attributed to the nonlinear effects. On the whole, the wave patterns obtained in experiments LWE1A and LWE2A are qualitatively similar, irrespective of the difference in the wave amplitudes.

In experiments LWE1B and LWE2B, the effect of moisture condensation is included. The initial relative humidity profile derived from the corresponding sounding is plotted in Fig.4.30. The relative humidity is rather high at the low levels, actually it is more than 95% in the lower 2km layer. Because of the low temperature in the layer, the absolute moisture content is however not high. The maximum specific humidity is only 7.6g/kg. The equivalent potential temperature θ_e calculated for this atmosphere was given in Fig.4.26(a). Because most of the atmosphere remains unsaturated during the model run, θ_e will not be effective in determining the static stability in most areas.

Fig.4.30. The initial profile of relative humidity (Case A) for experiments LWE1B and LWE2B

Fig.4.31. Fields of (a) the vertical velocity w and (b) the isentropes obtained in lee wave experiment LWE2A, at 180 minutes of model simulation.

Fig.4.32. As in Fig.4.31, but for experiment LWE2B, the moist run of LWE2A.

The simulated fields of vertical velocity w and the potential temperature θ at t=180mins are shown in Fig.4.29 for experiment LWE1B and Fig.4.32 for LWE2B. In both cases, cloud rolls are seen to form in the wave crests, where the lifting is largest in association with the low-lever convergence. These areas coincide with the lines of minimum vertical motion. In both runs, the average wavelength of the lee waves is slightly longer than that in the corresponding dry run, and the magnitudes of the vertical velocities are reduced, especially in the cases of the higher mountain in which more moisture is condensed (maximum q_c is 2.0g/kg in LWE2B but only 0.8g/kg in LWE1B). The increase in wavelength and decrease in the magnitude of the vertical velocity can be explained in terms of the reduction of the effective static stability in the saturated areas. However, due to the limited amount of moisture present, the modification by the moisture condensation is only quantitative rather than qualitative, for the particular sounding used. In other words, in the real atmosphere, the clouds associated with the lee waves observed on the 20/4/84, are actually the products rather than the initiator of the lee waves.

b) Interaction between waves produced by two separate ridges

In realistic situations, topography seldom consists of a single isolated ridge. There may exists a number of mountain ridges of varying size in the direction of prevailing

winds. However the cloud patterns observed from the satellite are frequently very regular and persistent, following the initial setting up at the leading edge of the cloud covered mountainous area. To understand the interaction between the waves produced by different mountain ridges, we performed a series of experiments in which two bell-shaped ridges of equal size are placed at different distances from each other. The experiment setting is basically the same as that for LWE1A, and a list of the experiments is given in table 4.4.

Table 4.4. Dry lee wave experiments with two separate bell-shaped ridges, at different distances from each other

Experiment	Mountain Scale(km)	Height(km)	(NX,NS)	Δx(km)	Δt(s)	Ridge distance
LWE3A	3.0	0.5	(257,41)	0.5	4.0	$0.5L_X$
LWE3B	"	"	"	"	"	$1.0L_X$
LWE3C	"	"	"	"	"	$1.5L_X$
LWE3D	"	"	"	"	"	$2.0L_X$
LWE3E	"	"	"	"	"	$2.5L_X$

The wavelength found in LWE1A is used as the reference wavelength. Both of the bell-shaped ridges have a peak height of 500m and a half-width of 3km. The distance between two ridges is 0.5, 1.0, 1.5, 2.0, 2.5 L_X in each experiment, where the reference wavelength L_X=12.56km. The w and θ fields at 180mins for the five runs are shown in Fig.4.33. In experiment LWE3A, the two ridges are very close to each other so that the spectrum of the topography profile is dominated by both the longer and the shorter Fourier components corresponding to the overall mountain profile and the individual ridges. Therefore a considerable amount of untrapped longer waves can be forced and they are shown clearly in Fig.4.33a over the mountain ridges. Shorter trapped waves are also evident in the model solution but they are not forced effectively as in the case of a single ridge and their magnitudes are small due to the cancellation between the waves

produced by two individual ridges. In LWE3B, the two ridges are one wavelength apart, each of them is able to force the flow independently to generate shorter waves that are mostly trapped. The wave produced by the second ridge is in phase with those already existing in the cross-ridge flow, i.e. those generated by the first ridge, as a result, the wave amplitude doubles in the lee of the second ridge. Such enhancement is more clearly seen the LWE3D in which the ridges are further apart at two wavelength distance from each other. Experiment LWE3C and LWE3E are cases in which the trapped waves produced by the two ridges are out of phase - they tend to cancel each other. A near perfect cancellation is achieved at the lee of the second ridge in LWE3E where the magnitude of the vertical velocity is only about 1m/s as compared to the 6m/s in the in-phase cases.

The results of the above experiments show that the mountain ridges in the lee of the first ridge would force the flow in a similar way to the first ridge as long as the wave amplitude is small, and there is a strong interference between the waves produced by each individual ridge. The result of the interference is found depending strongly on the distance between the ridges in terms of the wavelength of the trapped waves; the waves would be enhanced when the ridges are of integer wavelength apart but would cancel each other when the ridges are of an integer and a half wavelength apart. The resulting waves are close to those obtained by superimposing the waves generated by each individual ridge. These results suggest that both the structure of low-level atmosphere (most importantly the Scorer parameter) and the information on the actual topography is necessary in order to make accurate predictions of the occurance of lee waves. The former will determine the trapping condition of the atmosphere and the wavelength of the waves that are trapped whereas the latter would, to a large extend, determine the magnitude of these trapped lee waves. For the case being studied, the satellite image is not of high enough resolution for us to identify the lee wave interactions. Observational information from other sources would be necessary.

Fig.4.33. Fields of the vertical velocity w (left panel) and the isentropes (right panel) consequently for experiments LWE3A-E.

4.5.3 Case B: Lee wave experiments with the 8/3/85 Valentia sounding

a) Control runs

The sounding profiles used for the control experiments in this subsection is given in Fig.4.27. As was discussed previously, the atmosphere has a strong inversion layer between the 1 to 2 km level, in which most of the short waves are expected to be trapped.

The model configuration for these experiments and those to be described later is much the same as that for LWE1A, only that a smaller horizontal domain is used with a higher resolution to account for the decrease in wavelength of lee waves. The number of the vertical levels is also increased to better resolve the wave activities along the shallow layer of inversion.

Table 4.4 Lee Wave Experiments (LWE) with the sounding of Case B

Experiment	M. Scale(km)	Height(m)	(NX,NS)	Δx(m)	Δt(s)	Dry/Moist	Comment
LWE4A	1.0	500	(257,61)	250	3.0	Dry	
LWE4B	"	"	"	"	"	Moist	Standard RH
LWE5A	3.0	500	"	"	"	Dry	
LWE5B	1.0	750	"	"	"	"	
LWE6A	1.0	500	"	"	"	Moist	High RH
LWE6B	"	"	"	"	"	"	Even-higher RH
LWE7A	1.0	750	"	"	"	Moist	High RH
LWE7B	"	"	"	"	"	"	Even-higher RH

Fig.4.34. Fields of the vertical velocity w (left panel) and the isentropes (right panel) obtained in experiment LWE4A (upper panel) and LWE4B (lower panel).

Experiments LWE4A and LWE4B are respectively the dry and moist control runs that use the standard wind, temperature and moisture profiles. The bell-shaped ridge has a small half-width of 1km and a height of 500m. We show in Fig.4.34 only the w and θ fields at 180mins from both runs.

As is expected from the given atmospheric structure (shown by the profile of the Scorer parameter), the waves generated by the narrow ridge are almost completely trapped in the inversion layer. There is little wave activity in the nearly-neutral surface layer, not much wave activity is seen penetrating into the higher levels. The latter is also due to the lack of long wave components forced by the mountain ridge. Given the exceptionally high Scorer parameter in the inversion layer, the Froude number with respect to the mountain height is very high, therefore the wave amplitudes are, as is expected, rather large.

In the moist run LWE4B, clouds are seen forming in the wave crests similar to the

moist run in Case A, and they form mainly between the 1 to 2km height. But again due to the limited amount of condensation (maximum cloud water content at 180mins is about 0.6g/kg), the modification to the lee wave structure is also limited. The effect of moisture condensation will be seen to be much greater in later experiments in which the low level environmental humidity is increased.

The average wavelength of the simulated lee waves is about 6.5km, slightly shorter than the observed value. This may be because of that the actual inversion is overestimated by the Valentia sounding. In fact the inversion shown in two other soundings taken at the same time is weaker than in the Valentia sounding.

b) Sensitivities to the mountain scale and height

Two variations of experiment LWE4A are performed. In experiment LWE5A, the half-width of the ridge is increased to 3km while keeping the same height, and in experiment LWE5B a higher ridge of 750m is used with the half-width fixed at 1km.

The wave solution in LWE5A is shown by the w and θ fields at 180mins in Fig.4.35. The lee wave pattern and magnitude in the solution are much the same as those in LWE4A (Fig.4.34), but the wave activity propagating into the mid-levels is significantly increased, obviously due to the increase in the horizontal scale of the mountain ridge. The amplitude of the propagating waves over the ridge slope is large, and indicates that overturning would occur had the flow been forced by a higher ridge.

Fig.4.35. Fields of (a) the vertical velocity w and (b) the isentropes from experiment LWE5A.

Fig.4.36. Fields of the vertical velocity w (left panel) and the isentropes (right panel) at time 180, 240, 300mins of experiment LWE5B.

In experiment LWE5B, in which h_m=750m, the Froude number ($Fr=h_m l$) now has a maximum value of 1.88 in the inversion layer, this is much larger than the critical value for wave overturning obtained for a uniform flow over a finite amplitude ridge [0.85 according to Miles and Huppert (1969)], the flow is therefore expected to be very nonlinear. The isentrope fields in Fig.4.12 show that the waves generated in this experiment have indeed been transformed into a nonlinear wave regime, displaying a wave pattern rather different from that in LWE4A. The trapped waves show a clear

aperiodic behaviour - they propagate in the form of wave packets and evolve continuously in time and space. On the lee slope of the ridge, the low-level stable flow is accelerated right down to the ridge foot (see the θ fields at 180 and 300mins), producing rather strong downslope winds. Being forced by this strong low-level disturbance, the flow directly over the lee slope overturns at 180mins at the 4km level, accompanying a certain degree of wavebreaking. However at 240mins, little wave activity remains in the mid-level flow and the breaking waves at the previous time have been absorbed by the mean flow. The decrease in the wave amplitude after 180mins may be because the net forcing of the low-level flow is reduced when a considerable amount of wave energy is transferred to high levels by the waves propagating vertically. At 240mins, most of the wave energy is trapped, the disturbances on lee slope amplify subsequently. By 300mins, a large amplitude wave pattern similar to that seen at 180mins is again established over the lee slope, and the amplitudes are even larger. The vertical velocity pattern shows more clearly the vertical wave energy flux into high-levels at 180mins and 300mins, but much less flux at 240mins.

The formation of the strong lee slope winds can be explained in the context of the flow transition to a supercritical state in association with the low-level inversion layer (see Durran 1987). At the same time the trapping condition in the layer above the inversion is also important, since it determines the amount of the wave energy that will be trapped at the low-levels.

c) Effects of moisture on the lee waves

Four additional experiments were performed as listed in table 4.4. In these experiments the standard sounding used in the previous experiments are modified, mainly by increasing the low-level relative humidity.

In experiments LWE6A and LWE7A, the relative humidity below 1.3km is increased to 100%, (high-RH case), while in LWE6B and LWE7B, this saturated layer extends up to the 4km level (even-higher-RH case). In the latter case, the potential temperature at the

3.5 km level is slightly decreased to avoid excessive convective instability in the presence of a deep saturated layer. Fig.4.37 shows the profiles of (a) the potential and equivalent potential temperature and (b) the relative humidity for the two cases. As shown in the figure, the θ_e profile for the high-RH case (bold line) is almost uniform above the 2km level, indicating the effective static stability will be very small if the air flow there is saturated. In that case, waves from below will be effectively trapped. Whereas for the even-higher-RH case (shown in thin lines), the layer between 2 to 3km is convectively unstable, convection can therefore occur in this layer, but the layer above is then again relatively stable so as to permit the propagation of certain wave components. The convection, if it occurs, may act as a messenger between this layer and the inversion layer at the lower levels.

Fig.4.37. Initial profiles of (a) the potential temperature (solid lines) and the equivalent potential temperature (dashed lines) for the high-RH case (bold lines) and the even-higher-RH case (thin lines), and (b) the relative humidity for the two cases (bold and thin line for the two cases respectively).

Since the effects of condensation is larger in the case of higher mountain ridge, we will present here only the results of experiment LWE7A and LWE7B, the fields from these two runs are given respectively in Fig.4.38 and Fig.4.39. Although there is considerable diabatic effects due to condensation, the isentropes are still a good indication of the flow trajectories, by comparing the isentropes and the contours of the equivalent potential temperature.

The right panel of Fig.4.38 shows that at 180mins of experiment LWE7A, the clouds associated with the lee waves form below the 4km level, except directly over the lee slope where the clouds are deeper. The condensation in the lee waves crests has led to an increase in the wavelength of the lee waves. Compared with that in the corresponding dry run LWE4B, the overturning did not occur over the lee slope, obviously because of the release of latent heat in the cross ridge flow and in the deep cloud over the lee slope. By 240mins, the lee wave clouds have grown deeper, indicating parts of the mid-layer are saturated. The wave disturbances at the mid-levels are very weak in the saturated regions but much stronger in unsaturated regions. These wave disturbances, whose wavelength is now longer due to the reduction in the effective static stability, are clearly seen from the fields of the vertical velocity to be propagating upwards in-between the gaps (at x=16km and 30km) of the clouds. By 360mins, the longer waves at the mid-levels are well established, with the first wave trough remaining at the same place as at t=240mins (x=16km), the second trough has grown deeper and is now at x=32km, giving a well defined wavelength of 16km. Due to the effect of the moisture condensation, the wave crests are seen to be more shallower and broader than the wave troughs, the vertical motion is also concentrated around the wave crests. The amplitudes of the lee waves at the low-levels are seen much reduced downstream of the mountain ridge (see w field at 360mins), caused by the leakage of wave energy into the higher levels. The cloud water concentration shows maxima mostly at the 3km and 5km height, corresponding respectively to the waves crests of the trapped waves at the lower-levels and those of the longer mid-level waves. The wave pattern revealed by the equivalent potential temperature contours is similar to that shown by the isentropes, the difference is mainly at the waves crests where the condensation is greatest.

Fig.4.38. Fields of (a), (c), (e) the vertical velocity w and (b), (d), (f) the isentropes together with the cloud boundaries at time 180, 240, 360mins of experiment LWE7A (the high-RH case). (g) and (h) are respectively fields of cloud water and equivalent potential temperature at 360mins.

Fig.4.39. Fields of the vertical velocity w (left panel) and the isentropes together with the cloud boundaries (right panel) at time 180, 240, 300mins of experiment LWE7B (the even-higher-RH case). (g) and (h) are respectively fields of cloud water and equivalent potential temperature at 300mins.

The fields at various time of experiment LWE7B are shown in Fig.4.39. As was discussed previously, in the even-higher-RH case, the layer between 2 and 3km height is convectively unstable (see the θ_e profile in Fig.4.37), gravity waves can therefore not propagate in this layer, if the air there is saturated. The latter condition can be expected to be true in most areas since initially the air is saturated up to the 3.6km level. The prediction made from the θ_e profile is confirmed by the results of experiment LWE7B shown in Fig.4.39. The θ fields show that the isentropes at the 3km level in the lee are almost completely horizontal, implying there is hardly any wave activity at that level. However, below and above this level, there exist clearly two branches of wave trains The lower branch consists of mostly the shorter waves that are trapped underneath the unstable layer, and the upper branch is composed of waves that are of longer wavelength, and whose structure is significantly modified by the condensation processes - the saturated wave crests are broader than the wave troughs. The upstream tilting phase lines of the longer waves to the lee of the ridge shown by the w fields at all times indicate that a significant amount of wave energy is being transported into higher levels, providing the necessary energy source for the waves in the mid-levels. The two branches of waves are interdependent; the nonlinear amplification of the low-level waves produces wave disturbances of longer wavelength (which may not have been effectively forced by the narrow mountain ridge) that carry wave energy upwards, while the upper branch of the waves changes the trapping conditions so as to influence the amount of wave energy that can be trapped. The structure of the waves at the lower levels is also greatly influenced by the waves propagating separately at higher levels. At places where the upper-level waves are in phase with the lower-level waves, the low-level wave amplitude is enhanced (see e.g. the first wave ridge in the lee at 300mins), otherwise the wave amplitude is reduced (see e.g. the first ridge in the lee at 240mins). When little wave energy is leaked into the upper levels, the low-level trapped waves can persist over a long distance downstream of the mountain ridge (see fields at 240mins), whereas when these waves are untrapped by the moist process, their amplitudes is then much reduced only a few wavelength downstream (see fields at 300mins).

In summary, two experiments, LWE7A and LWE7B are performed, which use the modified sounding taken at 8/3/85 Valentia. The relative humidity is raised to 100% in the layer above the ground up to a different height. It is found that with a high relative humidity in the initial flow, the behaviour of the lee waves and the waves at higher levels are significantly different from the corresponding dry run, especially in areas where saturation is reached. The moisture condensation can change the effective static stability to the extent that it changes greatly the distribution of the wave energy originating from the mountain ridge. Unstable convection can also produce other sources of wave forcing. On the contrary, when the observed humidity profile is used (e.g. experiment LWE4B), little change is found in the wave structure due to the limited amount of moisture condensation. Judging from the wave amplitude on the lee slope, we can state that the pressure drag on the mountain surface in these moist runs is lower as compared to that in the corresponding dry run LWE5B.

Moreover, our experiments suggest clearly a mechanism of triggering deep convection by mountain gravity waves. Experiment LWE7B is a case in which a limited amount of convective instability is present in the environment and the instability is released when low-level trapped gravity waves produce sufficient lifting. These convective activities interact with the gravity waves, modulating the gravity waves and being also controlled by the wave activities. It can be speculated that if the trapped waves propagate along the stable layer at the lower levels into a region of large convective instability, deep convection would be triggered. On the other hand, these gravity wave activities could have been produced by pre-existing convection and further the cold outflow from the pre-existing convective storms can establish a stable layer to radiate the wave activities far away from the source. The problems on deep moist convection and convection forced by mountain ridges will be studied in the following two chapters.

Chapter Five

Strong, Long-lived Squall Lines - Two Dimensional Numerical Experiments

5.1 Introduction

A squall line is known as any line or narrow band of active thunderstorms. Squall lines are frequently observed to last for several hours and sometimes propagate relative to the ground at a considerable speed, producing heavy precipitation on their path. In this chapter, we describe a series of two-dimensional (2-D) experiments carried out using the nonhydrostatic σ-coordinate model described in previous chapters; and we address mainly the problem as to the dynamics and the optimal condition for strong, long-lived squall lines. Recently, Rotunno, Klemp and Weisman (1988, thereafter RKW) presented

a review of both the observational and modeling studies of squall lines. They addressed the issue that whether a squall line is a system of special, long-lived cells, or a long-lived system of ordinary, short-lived cells, they also suggested the optimal conditions for a strong long-lived squall line to be established and maintained.

The classical model of a squall line views it as a system of convective updraughts and downdraughts aligned perpendicular to the wind shear. Ludlam (1963) suggested that a strong updraught tends to lean against the wind shear, allowing the updraught to unload its rain on the upshear side rather than falling directly above the low-level updraught so as to cut off low-level inflow. Newton (1966) also took a similarsingle-cell view of a squall line. Newton and Ludlam's conceptual model is illustrated in Fig.5.1.

Fig.5.1. Schematic of the Ludlam-Newton model of a steady two-dimensional squall line in a deep, uniform-shear environment. The strong updraught leans against the shear and drops its rain out on the upshear side, allowing a long-lived cell (Reproduced from Fig.3 of RKW, 1988).

Fig.5.2 The conceptual model of squall line in a low-level sheared environment derived from a 2-D numerical simulation of TMM (1982) (Reproduced from Fig.5 of TMM, 1983, .).

However, attempts in the seventies to replicate the Newton-Ludlam model in the presence of deep ambient shear using numerical models were not successful. The failure was then thought to be due to the limitation of two-dimensional models. It was considered that three dimensionality was an inherent property of cumulonimbus clouds (Lilly, 1979) and squall lines were mostly composed of organized supercell thunderstorms. On the other hand, this idea was not supported by some of the later observational studies. Bluestein and Jain (1985), by reviewing approximately 10 years of data from the Oklahoma City radar, showed that many intense squall lines are not composed of supercell thunderstorms. Further more their grand average hodograph for all cases shows that the largest wind shear is confined at low levels.

In 1982, Thorpe, Miller and Moncrieff (1982, hereafter TMM) re-examined the strictly two-dimensional problem, with special attention paid to the shear in the ambient wind profile. TMM showed that quasi-steady convection that bore most of the characteristics of observed squall-lines can be produced if the mid- and upper-level flow has small shear but the low-level shear is large. The experiment in which the shear inflow is confined below 2.5 Km with zero wind above was found to produce maximum surface precipitation. The quasi-steady squall line in that experiment appeared to be unicellular, and the conceptual model drawn from the numerical simulations consists of distinct com-

ponents of an overturning updraught, a jump type updraught, a shallow downdraught, and low-level rotor and an inflow boundary layer (Fig. 5.2.).

TMM recognized clearly the essential role of both the low-level shear and the shallow rain-induced downdraught in maintaining steady convection. They reasoned that the low level shear is essential in order to prevent the rain-produced surface outflow from propagating rapidly away from the storm. TMM also showed that when reversed shear was included above the low-level shear, the storm that developed was less vigorous but also long-lived. The storm showed multicellular characteristics with discrete cells being continuously generated and advected rearwards relative to the cold outflow front. When the mid- to upper-level shear was in the same direction as the low-level shear, the storm was short-lived, due to the downshear tilting of the updraught. RKW (1988) and in a companion paper (Weisman, Klemp and Rotunno, 1988; Hereafter WKR), attempted to further explore the mechanism of strong, long-lived squall lines, based on a series of two- and three-dimensional numerical experiments, with particular attention focused on the magnitude of the low-level shear. They also obtained, as TMM did, long-lived deep convection provided there was sufficient low-level shear (uniform shear inflow below 2.5 km level as in TMM). A shear of 17.5 m/s over 2.5 km was found to allow for a sequence of the strongest cell updraughts. The optimal condition for the longest-lasting deep convection, as they claimed, comes from a balance between the circulation induced by the spreading cold outflow or cold pool and the circulation of the sheared inflow. Their arguments are illustrated in Fig.5.3.

Fig.5.3. Schematic diagram illustrating RKW's vorticity arguments on how an erect updraught can form in the presence of both the inflow wind shear and a cold pool. RKW argued that the negative vorticity of the underlying cold pool will induce a circulation that causes the updraught to lean upshear, whereas the positive vorticity in the inflow will cause the updraught to lean back over the cold pool. When the positive and negative vorticity matches each other, an erect updraught may form.

RKW argued that the horizontal inflow can turn to the vertical direction to form an erect updraught in the presence of a cold pool circulation that tends to prohibit deep lifting, only when "the circulation associated with the cold pool's negative vorticity approximately balances the circulation associated with the positive vorticity of the low-level shear."

Their arguments clearly suggest that the tilt of the updraught is dominantly dictated by the amount and the sign of the vorticity contained in the air that enters the updraught. Hence a more or less vertical, symmetric deep circulation requires that the vorticity in the original inflow be largely diminished at the cold pool front (CPF). However RKW did not suggest how this diminishing process could happen., nor did they attempt to quantify the relative importance of the vorticity in the inflow as compared with that of the vorticity to be generated by buoyancy in the updraught. One may argue that the diminishing of the vorticity in the inflow at the cold pool front can only occur when there is sufficient turbulent mixing between the inflow and cold pool air. One may also suspect the role of the net vorticity remaining in the updraught as compared to the role played by the cloud

and subcloud layer relative flow in determining the tilt of the updraught. Our numerical experiments suggest that it is the momentum rather than the vorticity in the inflow that is important, which will act against the cold pool (through a pressure force according to Bernoulli's equation) to prevent the cold pool front from propagating relative to the cloud level air. The air in the inflow that impinges upon the cold pool front is lifted and enters the mid-layer which has to be more or less calm viewed in the frame of reference moving with the cold front. The tilt of the updraught is determined by the relative speed of the cloud layer flow, being also modulated to a certain extent by the horizontal momentum retained in the air that enters the updraught. One can further deduce that the crucial factor is the difference between the speed of the subcloud layer air and the air in the cloud layer, and the optimal condition for the updraught to be near-vertical is that the horizontal speed of the mid- to upper-level flow is approximately equal to (or slightly less than to allow for slightly upshear tilting updraught) the propagation speed of the underlying cold pool.

In later sections, we will describe a series of numerical experiments of squall lines. These experiments are designed to examine the role of the interaction between the low-level ambient inflow and the cold pool outflow, and the mechanism by which such an interaction determines the development and evolution of a squall line. The importance of vorticity versus momentum in the inflow is understood through experiments that have either a step-type (zero-vorticity) or shear-type (constant vorticity) inflow. A conceptual model of the inflow-cold pool interaction (Section.5.4.1) and the optimal conditon for a intense long-lasting squall line (Section 5.5) are proposed. The sensitivity of squall line simulations to diffusion is exmained in Section 5.6. In next section several experiments of moist convection in a zero-wind environment that has the same thermodynamic structure as that for later squall line experiments will be presented first.

5.2 2-D moist thermal convection in a zero-wind environment

The thermodynamics and parameterized cloud microphysics of our numerical model have been described in detail in Chapter three. The model has been used in Chapter four

to study moist mountain waves in which clouds form as condensation occurs. However, the microphysical parameterizations involving both cloud water and rainwater have yet to be tested. We present in this section a number of 2-D experiments of moist convection in a zero-wind environment, which serve partly as the model verification.

Fig.5.4. Tephigram of the thermodynamic sounding for the moist convection experiments and later experiments of squall lines. Straight lines at right angle to each other are isotherms and dry adiabats. Lines lying roughly horizontally are isobars. The thick full lines is the temperature profile and the thick dashed line represents the moisture profile.

The thermodynamic sounding used here and for all the later experiments of squall lines is depicted by a Tephigram in Fig.5.4. This sounding is typical of the environment of mid-latitude squall lines (cf. Bluestein and Jain, 1985) and is also similar to that used in RKW and TMM. The surface layer is relatively dry for this sounding so that rainwater evaporative cooling can be significant. The minimum θ_e (equivalent potential temperature) is at the level of 3.5km (roughly 650HPa) and has a value of about 312K.

The air originating from this level would gain a 12 degree deficit in temperature had it been brought moist-adiabatically down to the surface. This temperature deficit sets the lower limit of the temperature possible for the rain-induced cold pool. The total CAPE (convective available potential energy) for the given sounding is rather high and is typical of the environment of severe mid-latitude squall lines (Bluestein and Jain, 1985).

Table 5.1. Experiments of 2-D moist thermal convection with no ambient winds

Experiment	(NX,NS)	Δx (km)	Δt (s)	FCT for θ'	Ri/Def. mixing	Background diffusion (m^2/s)
MTC1A	(65,30)	1.0	6.0	yes	yes	50.0
MTC1B	(65,60)	0.5	4.0	yes	yes	50.0
MTC2A	(65,30)	1.0	6.0	no	yes	50.0
MTC2B	(65,60)	0.5	4.0	no	yes	50.0
MTC3A	(65,30)	1.0	6.0	yes	no	50.0
MTC3B	(65,30)	1.0	6.0	yes	no	200.0

The parameters for the six moist convection experiments are listed in Table 5.1. In these experiments p_{surf}=1000HPa, p_{top}=50HPa. A damping layer is applied above the 12km level. The convection in all cases is initiated by a saturated line thermal perturbation that has a maximum temperature surplus of 2K. It is 10km wide, 1.5km deep and is centred at 1km AGL. Being saturated, it bears a surplus of about 5K in θ_e. The warm cloud microphysical processes described in Chapter three are all included in these experiments. The terminal fall speed of rainwater is given by formula (3.1.13).

a) Control experiment

Experiment MTC1A is the control run which has a 1km horizontal resolution, 30 levels in vertical, uses the FCT scheme to advect θ', q_v, q_c, and q_r, and incorporates a full formulation of turbulent mixing parameterization together with a constant background diffusion with the coefficient K_{BG}=50m^2/s. In other experiments, the sensitivities to the spatial resolution, the advection schemes and the formulations of diffusion are examined.

The time development of the cloud cell is depicted in Fig.5.5 by the wind vectors and the θ_e fields at various model time. At 10 minutes a convective circulation is seen symmetric around the x=0km central line (Fig.5.5a); and cloud top is slightly higher than 3km. Condensation has occurred by this time, producing a light cloud with a maximum q_c of less than 1.0g/kg. By 20 minutes the cloud cell has risen to the 10km height level (Fig.5.5c) and the core updraught speed is now higher than 30m/s. Rainwater with a mixing ratio higher than 8g/kg is generated but most of it is still suspended at high levels by the strong updraught. By 30 min, the heavy water loading (about 10g/kg at t>20 min) has turned the updraught along the central line of the cloud into downdraughts at both the upper and lower levels, with only a weak updraught remaining at the mid-levels (Fig.5.5e). The rain has just fallen on to the ground (shown by the shading). The main upward motion is now roughly 6km off the original central line, the surface flow immediately below the cloud (at x=0) has changed into spreading outflow. The cloud cell decays rapidly as this cold outflow propagates away in both directions, cutting off the supply of moist unstable air from the low-levels. The life-time of the primary convective cell is about half an hour to 40 minutes.

The development of the cloud cell is also manifested by the fields of the equivalent potential temperature θ_e which is conserved along air parcel trajectories in the absence of diffusion. Fig.5.5 shows that the convection occurs as the high θ_e air penetrates through the mid-level low θ_e air to reach the high-levels. At 20 min, the maximum is at about 8km height. This maximum is shown in Fig.5.6 to rise further to join the high θ_e at about 10.5km height level. At the later time when the updraught at the high-levels has evolved

Fig.5.5. Fields showing the development of a moist thermal convection from control experiment MTC1A. In the left panel are fields of wind vectors together with the cloud boundaries (bold lines) and areas with rainwater (shaded). The right panel shows the fields of θ_e at various time. (Only 16km central domain is shown, with the horizontal grid position indicated by the ticks on the border).

Fig.5.6. Hovmoeller diagrams of (a) the vertical velocity w, (b) the perturbation potential temperature θ', (c) the rainwater content q_r and (d) the equivalent potential temperature θ_e along the central line of the symmetric cloud cell in experiment MTC1A.

into downdraughts, the θ_e contours there (e.g. the 322K contour in Fig.5.5e) are seen dipping downwards while the major upward penetrations have moved off the central line.

The time evolution of properties inside the cloud cell is best depicted by Hovmoeller diagrams, with the quantities along the central line of the cell being plotted against time. These are given in Fig 5.6, and are respectively for w, θ', q_r, and θ_e along the x=0km line. They all show clearly that the cell convection gains its maximum intensity at about 23 mins, and then undergos a rapid decay in which updraught is disrupted by heavy rainwater-loading and turns into a downdraught at lower levels (Fig.5.6a,c). The rain reaches the ground at 30mins,the evaporation of which after this time then produces a

pool of cold air below 2km level (Fig.5.6b). The conservation of θ_e along with the cloud cell is shown by Fig.5.6d to be excellent. This (as will be shown later) should be largely attributed to the use of the FCT scheme for advection.

In conclusion, the control experiment MTC1A simulated successfully the life cycle of a moist thermal convection in a two dimensional frame work. The convection obtained was vigorous and physically consistent. It can be inferred that the θ_e along air parcel trajectories is excellently conserved. With the application of the FCT scheme to the advective processes, the problem with 'negative water' generation by conventional high-order accurate advection schemes is entirely eliminated.

b). Sensitivity to spatial resolution.

In experiment MTC1B, the spatial resolution is doubled over that of control run MTC1A, with 0.5km horizontal grid length and 60 vertical levels. The fields of wind vectors and θ_e at 20min of this experiment are given in Fig 5.7, and in Fig.5.8 is shown the time evolution of q_r and θ_e along the central line of the convective cell. The results from MTC1B are rather different from those of the control experiment. The cell circulation is clearly better resolved and a mushroom-shaped cloud cell is seen to have formed at 20min (Fig.5.7) with the high θ_e air being advected from the upper edge of the cloud sidewards and downwards by the cell circulation. There is an indication of the mid-level low θ_e air being wrapped up by the circulation into the cloud, though this did not continue due to the subsequent formation of downdraught. The updraught in this high-resolution run is however much weaker (Fig.5.8a), with a downdraught forming at the top of the cloud as early as 15min. This is caused by the thinning of the layer of high θ_e air at the cloud top boundary hence the reduction in buoyancy force there (Fig.5.7b). The earlier cutting off of the low-level high θ_e air supply (by the intruding mid-level low θ_e air) contributes also towards the lack of overall vigor in the convection. At any rate, we should regard the development of the convective cell obtained in this high-resolution run is as being more realistic.

Fig.5.7. As in Fig.5.5 but for experiment MTC1B (Fields are only shown at t=20min here).

Fig.5.8. As in Fig.5.6 but for experiment MTC2A.

c) Sensitivity to advection schemes.

The flux-corrected transport (FCT) scheme, as is described in chapter three, is used in all cases to advect water quantities (q_v, q_c and q_r). But its use for the θ' equation is optional. The leapfrog-centred advection scheme can be used instead. Experiments MTC2A and MTC2B correspond to MTC1A (control) and MTC1B respectively expect that the leapfrog-centred instead of the FCT scheme is used for the θ' equation.

Fig.5.9. The fields of (a) wind vectors and (b) θ_e at 20min from experiment MTC2A. The leapfrog-centred advection scheme is used for θ' equation instead of the FCT as in MTC1A. The conservation of θ_e is far from being as good as in MTC1A.

Fig.5.10. Hovmoeller diagrams of (a) w and (b) θ_e along the central line of the convective cell for experiment MTC2A (cf. Fig.5.6).

Fig.5.11. As in Fig.5.10 but for experiment MTC2B (cf. Fig.5.10 and Fig.5.8).

The convective circulation and the θ_e field at 20min of experiment MCT2A are shown in Fig.5.9. Compared with the corresponding fields in Fig.5.5c and Fig.5.5d, the circulation is very much weaker and more shallow. The θ_e along with the rising cell is clearly not well conserved. The low-level 328k contour present initially is now completely absent in Fig.5.9b, and the maximum height the cloud top reaches is more than 2km lower (Fig.5.10). The value of θ_e is progressively reduced along with the rising cell (Fig.5.10b). The maximum q_r is only 4g/kg. All of the above results suggest that the leapfrog scheme is inadequate for advecting a relatively small volume of buoyant air penetrating a layer of air that has a lower θ_e.

Given the fact that the updraught is only resolved over a few grid points in MTC2A, one may ask where the inadequacy may be relieved by increasing the spatial resolution. This is done in experiment MTC2B. However, a similar effect of resolution increase is found as in experiment MIT2B; when the resolution is increased, a downdraught forms at the top of the cloud between 15 to 20mins, making the major updraught even weaker. Therefore increasing in spatial resolution did not improve the results and the use of the FCT scheme in the θ' equation as in the equations for water quantities is having a very significant impact on the conservation properties of the numerical model. The leapfrog-

centred scheme, at least when the FCT scheme is used for the water quantities, is inadequate to describe thermal convection in which the updraughts are frequently very narrow.

d) Sensitivity to turbulent mixing.

In experiments MTC3A and MTC3B, the Richardson number and deformation dependent turbulent mixing is switched off, with only a constant background diffusion being included, and the coefficient K_{BG}=50m^2/s and 200m^2/s respectively. The differences in the solutions as compared to those for MCT1A are found to be only quantitative. The solutions in MTC3B in which K_{BG}=200m^2/s are found very similar to those from MTC1A in which the calculated mixing coefficient is of the order of 200m^2/s (compared Fig.5.12 with Fig.5.6). When K_{BG}=50m^2/s as in MTC3A, the maximum speed of updraught is larger (36m/s) and the cold pool air more shallow (Fig.5.13), due to the weaker diffusion.

Fig.5.12. Hovmoeller diagrams of (a) w, (b) θ_e along the central line of the convective cell in experiment MTC3B, in which K_{BG}=200m^2/s.

Fig.5.13. As in Fig.5.12 but for experiment MTC3A, in which $K_{BG}=50m^2/s$.

e) Summary

In this section, the model simulation of the life cycle of a two-dimensional moist convection in a zero-wind environment has been presented, together with a number of sensitivity tests. These experiments verify the thermodynamical and cloud microphysical processes of the numerical model. The control run demonstrates a very good performance of the model while the use of the FCT scheme significantly contributes to this. Appropriate spatial resolution is shown to be necessary to properly resolve convective circulations, but the different formulations of diffusion is not found to have a major impact, at least in the simulations of the life cycle of isolated convection. The results of these experiments in a simple environment will lend guidance to the experimental design of our squall line simulations in the following sections.

5.3 Experimental design for squall line simulations

Although squall lines in reality may not be exactly two-dimensional, our use of two-dimensional numerical model is justified by the conclusions of RKW through inter-

comparison of 2-D and 3-D simulations - the essential physics of the squall line that develops in a medium shear perpendicular to the line is contained in the 2-D framework. Recent successes in 2-D squall line simulations such as those of Dudhia, Moncrieff and So (1987, thereafter DMS) and Forvell and Ogura (1988) also lend support to this.

The model characteristics are similar as used for the control experiment MTCIA in the last section, in which the FCT scheme is used to advect both water and thermal quantities. For all the following experiments, a domain of 192km in horizontal is used with Δx=1km. The vertical domain ranges from 1000HPa to 50HPa with 60 levels. The corresponding vertical grid-length varies from about 150m at the low-levels to nearly 1.5km at the top. The high resolution at the low levels is considered necessary since the major activities associated with wind shear and cold pool outflow are concentrated at these levels. The vertical resolution in our model is naturally higher at the lower levels with constant increment in σ. The time step Δt=4 seconds.

The development and evolution of squall lines can be dependent upon many factors, among them are the wind profile, the thermodynamic sounding of the pre-storm environment. However, the work of TMM and RKW, WKR, has shown that the interaction between the cold pool outflow and the low-level wind shear is most important in determining the characteristics of simulated squall lines. In order to isolate the key role of the inflow, we shall fix the environmental thermodynamic conditions in all of our subsequent experiments while altering only the inflow. This modelling philosophy is also followed by TMM and RKW. The sounding is given in Fig.5.4 and is typical of the severe mid-latitude squall line environment as was discussed in the previous section. Two types of inflow profile are used in our experiments. The first has an uniform inflow (constant horizontal velocity U_0) between z=0 and z=1.5km. The flow speed decreases to zero from 1.5 to 2.0km and then remains as zero above. We call this the step type inflow. The second type is the low-level shear inflow as was used in TMM and RKW. The flow reduces from U_0 to zero linearly from z=0 to z=2.0km, and then remains zero above. This shear layer is slightly shallower than in TMM (2.5km deep there). The inflow

profiles are schematically illustrated in Fig.5.14. Experiments with these wind profiles help us to understand the specific role of the momentum versus the vorticity in the inflow.

Fig.5.14. Schematic diagram of the inflow profiles for the squall line experiments. (a) shows step type inflow profiles which has a uniform speed therefore zero vorticity below 1.5km, (b) show shear inflow profiles which has a constant vorticity.

The convection in our experiments is initiated in a similar way as in TMM, i.e. by specifying an initial localized cooling which attempts to model evaporative cooling from previous convective cell. Convection can also be started by specifying an initial thermal perturbation as in RKW, but the procedure of initial cooling would accelerate the process by which the initial convection is established. Comparisons show that the development of simulated squall lines at later stage depends very little on the initiation procedure.

The cooling function $\dot{Q}(x,\Phi_S,t)$ is specified as

$$
\begin{aligned}
t \le 15 \text{ min} \quad & \dot{Q} = Q_c && 0.0 \le \Phi_s/g < 1.5\text{km} \\
& = Q_c\,(2.5 - \Phi_s/g) && 1.5 \le \Phi_s/g < 2.5\text{km} \\
& = 0.0 && 2.5 \le \Phi_s/g \\
15 \le t < 21 \text{ min} \quad & \dot{Q} = (21 - t\,)\,\dot{Q}(t=15)/6 \\
t > 21 \text{ min} \quad & \dot{Q} = 0.0
\end{aligned}
$$

where

$$
\begin{aligned}
Q_c &= -\,0.48 \text{ K/min} && |x-x_0| \le 5\text{km} \\
&= 0.0 && |x-x_0| > 5\text{km}.
\end{aligned}
$$

The imposed cooling will produce a temperature perturbation of about -6 degree, but the cooled air will be quickly advected downstream by the low-level flow, and the subsequent cold pool is entirely maintained by the rainwater evaporative cooling.

Table 5.2. The specifications of numerical experiments of long-lived squall lines

Experiment	Inflow	$\|U_0\|$ (m/s)	Ri/Def mixing	Background dif. (m^2/s)
SLE1A	Step	10	No	100.0
SLE1B	"	15	"	"
SLE1C	"	18	"	"
SLE1D	"	25	"	"
SLE2A	Shear	12	No	100.0
SLE2B	"	15	"	"
SLE2C	"	20	"	"
SLE2D	"	28	"	"
SLE3A	Jet	10/18	No	100.0
SLE4A	Step	18	No	20.0
SLE4B	"	"	"	200.0
SLE5A	Step	18	Yes	20.0
SLE5B	"	"	"	100.0

In the case of step inflow, there exists a layer of strong shear between 1.5 to 2.0km. Diffusion acting on the full flow field is obviously detrimental to the maintenance of such an initial state. On the other hand, diffusion that acts only on perturbation fields will help to maintain this state. Therefore, only a constant background diffusion is included in a majority of our experiments. A few experiments with differing diffusion magnitude and formulation are also presented. Table 5.2 summarizes the specifications of the experiments to be discussed. Experiment SLE5A uses a jet inflow profile in which the inflow speed has a maximum speed at z=1.5km and decrease linearly to 10m/s at z=0 and to 0.0m/s at 2.0km and remains zero above 2.0km. Such an inflow contains vorticity of opposite signs.

5.4 Results of the squall line experiments

5.4.1 Step type inflow

The surface precipitation rates averaged over two minutes for four experiments SLE1A to SLE1D are plotted against time in Fig.5.15. In all cases, rainfall is seen falling to the ground in-between 30 to 40 minutes. The first cell, as indicated be the associated rainfall pattern is generated at around x=0.0km, and then moves to the rear of the line (to the left). However the subsequent development, especially the propagation, of these lines are very different. The convection is most persistent in SLE1C in which the system is almost stationary relative to the ground before it starts to surge ahead at 4.5hrs. In experiment SLE1A in which the inflow is weakest (10m/s), the system move rapidly against the inflow at a speed exceeding 4m/s relative to the ground, and the precipitation rate, especially after 2hrs, is much lower than that in the other three cases. The convective system obtained in SLE1B is almost as persistent as in SLE1C, only that it moves at a steady speed relative to the ground. Fig.5.15c shows clearly that multiple cells are being generated at the CPF and are then advected to the rear of the line. The cell re-generation after 4hrs are extremely regular, with a period of about 15 minutes. Experiment SLE1D has the strongest inflow (25m/s), the convective line in the run is seen moving in the opposite direction as in the other three, with the cold pool being pushed back by the strong inflow. In spite of this, still a considerable amount of precipitation is produced. After 315 minutes, this system weakens when another convective line develops upstream at x=10km, altering the upstream conditions for the first line. The secondary development is clearly related to the disturbances that developed on the low-level strong shear, but it is not clear whether its development and its location are deterministic.

Fig.5.15. The surface rainfall rate (mm/hr) for experiments (a) SLE1A, (b) SLE1B, (c) SLE1C and (d) SLE1D respectively.

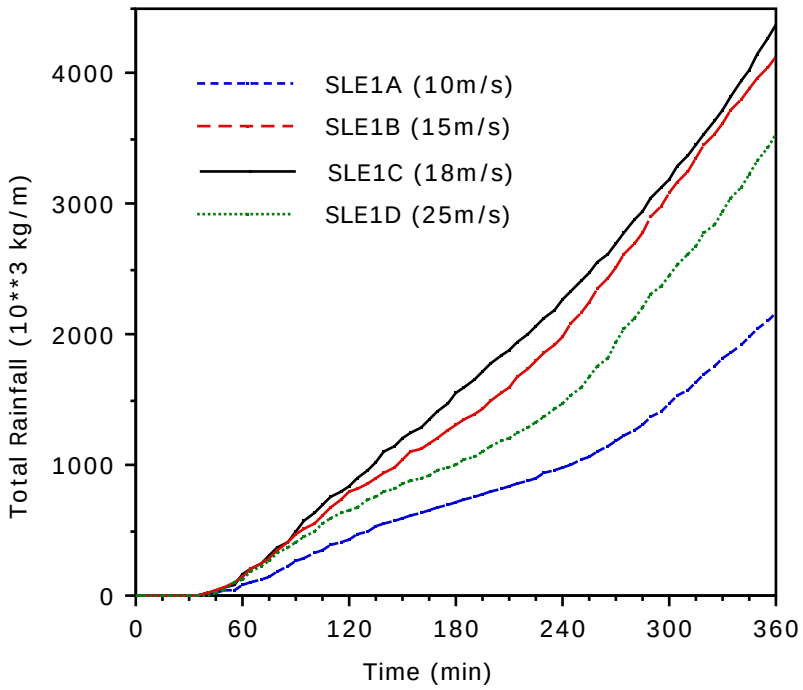

Fig.5.16 The accumulated total surface rainfall in the model domain against time for experiment SLE1A to SLE1D.

Fig.5.15 indicates that in spite of the differing propagation behaviour, the squall line systems in a moderate to strong low-level inflow (15-25m/s) are all long-lived. Especially in SLE1B and SLE1C, the system is not exhibiting any sign of decaying by the end of simulation (6hrs for SLE1C and up to 10hrs for SLE1B). They may be expected to last forever if the environmental conditions are not changed.

The total accumulated precipitation in the model domain is plotted against time for the four cases in Fig.5.16. The maximum precipitation is produced in SLE1C, with SLE1B in the second place. Experiment SLE1A produces the least rain. In fact the precipitation becomes very weak after 2hrs. The difference between SLE1B and SLE1C comes mainly at the early stage when the convection in SLE1B is relatively weaker. The amounts of rainfall from both runs produced between 4 to 6hrs are almost the same (2.30×10^6 versus 2.29×10^6 kg/m). The precipitation in SLE1D comes partly from the second convective line therefore the precipitation from the first line is less than that shown in Fig.5.16.

Fig.5.17. The time series of the w_{max}, w_{min} for experiment SLE1C (a) and SLE1B (b), and of the θ'_{max}, θ'_{min} for SLE1C (c) and SLE1B (d).

The time evolution in the intensity of the simulated squall line system is also well indicated by the time series of the maxima and minima of vertical velocity and temperature perturbations. These are given in Fig.5.17 for SLE1C and SLE1B. In general, the maximum intensity of updraught occurs at 35min when the first convective cell is triggered by the low-level cold outflow which has a minimum temperature of about -6K at 20min when the specified cooling is switched off. A rapid decrease in the cold pool temperature immediately follows after 35min when the rain from the first intense

convective cell reaches ground (Fig.5.17b). Subsequently, several oscillations are seen in the intensity of updraught (Fig.5.17a), similar to that found by RKW. This period is named by RKW as a phase of 'quasi-periodic redevelopment' of cells, but this phase in our simulations with step inflow is generally shorter. Associated with these cell re-developments, there are further decreases in the cold pool temperature. By 2hrs, a very low temperature of about -10K is reached in both cases, the system then enters a long stage of steady evolution, in which new cells are periodical generated at the CPF and advected rearwards, as is reflected by the surface rainfall pattern in Fig.5.16. This stage of steady evolution is absent in the 'optimal' case of RKW, instead they found that after the cold pool is intensified, the system starts to decay while the cold pool surges ahead. Fig.5.17d shows that the minimum temperature of the cold pool in SLE1B is maintained at a nearly constant level of -10K after 2hrs, and the system then propagates at a near constant speed relative to the ground (Fig.5.16b). In SLE1C, the cold pool temperature exhibits oscillations whose time scale is much longer than that of individual cells. It is noticeable that the cold pool is strengthened at 280min, associated with this, the cold pool experienced a sudden surge ahead and began a stage of steady propagation after the quasi-stationary phase the time before.

Regardless of the ground relative speed of the system, the surface rainfall pattern in both cases are rather similar to that produced by a simulated squall line of Forvell and Ogura (1988) in which the environmental sounding derived from a Oklahoma squall line (Ogura and Liou, 1980) is used. Their results agree with observation in that the squall line system is multicellular and the system propagates rapidly relative to the ground. Their wind profile include weak low-level flows and stronger flows at the upper level, with the wind shear being concentrated mostly below 2.5km. They showed a system relative surface rainfall pattern that was extremely regular at the mature stage of the squall line, and the primary cell regeneration period was about 30 minutes. The cell regeneration clearly occurs quicker in our simulations, with the period being only about 15 minutes. This difference is almost certain to be due to the different wind profiles used.

a) Experiment SLE1C

The flow fields of the simulated squall line in SLE1C are shown in Fig.5.18. The fields of u, w, θ', θ_e, q_r and Φ at selected time are shown on Fig.5.19-21. At 60 minutes after initiation the second cell becomes mature as indicated by the maximum updraught intensity and maximum θ' in Fig.5.17. The updraught at this time is vigorous and almost vertical (Fig.5.18a and Fig.5.19b), the cloud top is up to 12km and the rainwater exceeding 9g/kg is seen suspending at the 6km level (Fig.5.21a). At the low-levels ahead of the CPF, the inflow speed is decelerated to zero over only 2-3km horizontal distance (Fig.5.19a). The convergence forces the entire inflow air to go up which is then accelerated upwards by the buoyancy force (Fig.5.19b). The downdraught underlying the low-level updraught is evident (Fig.5.19b) which is clearly bringing mid-level low θ_e air down to the surface (Fig.5.20b). Further to the left of this low-level low θ_e air we can see alternating blobs of air with high and low θ_e. The low θ_e air is produced by the downdraught of the first intense convective cell, and the high θ_e air is mostly the evaporation cooled inflow air that forms part of the cold pool in between the gaps of cell regeneration. The outflow at the high levels from the updraught spreads equally in both directions. During the next hour, the cold pool greatly intensifies (Fig.5.17b) to about -10 degree, and moves forward slightly. At 120min, the updraught becomes titled upshear (downstream of the inflow), and spans over a 30km horizontal distance but remains very deep. Embedded on this broader scale updraught are a number of alternating updraught and downdraught cores that are associated with individual cells that are advected rearwards after being generated at the front line and that are seen to be at different stages of their life history. Directly behind the CPF, a well established rotor is evident. The θ_e field (Fig.5.20d) indicates that the air inside this rotor is mostly of low-level origin, that is, the air lifted at the CPF, cooled by rain evaporation, then entrained into the rotor at the back, forming part of the downdraught. Further to the rear is a downdraught circulation consisting of air of mid-level origin (Fig.5.20d).

Fig.5.18. The flow fields of squall line experiment SLE1C at selected time. This experiment produced a maximum surface precipitation among four experiments using step type inflow. In the pictures, x=0 is the centre of the initial cooling, which in this experiment is 72km from the left boundary. Only a portion of the model domain is shown here. The cloud boundary (q_C=0.01g/kg) is indicated by the thick lines, so is the boundary of the cold pool (θ'= -1.0K). The velocity shown by the arrows are ground relative. At t=60min, (a) the system is in the initial 'cell re-development' stage, the updraught is shown to be almost vertical, though the vorticity in the inflow is zero. (b) At t=120min, the system has just entered a stage of steady evolution. The updraught is relative weaker than before but still very deep and is tilting downstream (upshear with respect to the sub-cloud and cloud layer relative shear). (c) (d) At t=240 and 360 min, the flow fields change very little in a broad sense from that at 120min, showing the system is rather steady during this period.

Fig.5.19. The fields of ground-relative horizontal velocity u (left panel) and the vertical velocity w (right panel) at selected time for SLE1C (U_0=18m/s). The picture setting in this figure and the most of the following figures is the same as in Fig.5.18.

Fig.5.20. As in Fig.5.18, but are fields of the potential temperature perturbation θ' (left panel) and the equivalent potential temperature θ_e (right panel).

Fig.5.21. As in Fig.5.18, but are fields of the rainwater content (q_C) (left panel) and the potential height perturbation (Φ'/g) (right panel)

The circulation at 120min is already very close to that in the conceptual model of TMM (Fig.5.2), and it remains qualitatively similar (Fig.5.18c,d) during the next a few hours of model simulation. At 240min, the rear-to-front flow at 2 to 3 km levels is intensified and extends right to the CPF, with the flow speed exceeding 8m/s. The cloud anvil is spreading over a wider area in both the front and back, as a result, the rain curtain is also spreading over a wider region, inducing even stronger downdraughts by evaporative cooling. The system hardly moves during the first 4 hours of simulation.

A sudden forward surge of the system occurs at 270min (Fig.5.15c) as the cold pool is enhanced. At 300min, the cold pool is 14km from the the centre of initial cooling. The cold pool, therefore the system propagates a further 4km during the next hour. At 360min, the rain is seen extending over more than 80km to the rear of the front (Fig.5.18a), and the rear-to-front flow is now exceeding 12m/s. The observational evidence of this type of strong rear inflow is documented in Smull and Houze (1987) and is generally regarded as self-induced, i.e. induced by the convective system itself. The multicellular structure indicated by the surface rainfall pattern is also evidenced by the separate updraught cores in the w field at 360min (Fig.5.19f).

The θ_e field at t=300min shows that the air ahead of the CPF below 2km is almost completely drawn into the updraught to levels higher than 7km. This suggests that although the updraughts are not vertical, a very high efficiency is still being achieved by the system in releasing the CAPE contained in the low-level flow. In fact, the upshear tilting of updraughts has been regarded in classical conceptual models as the effective orientation (Browning, 1977), this seems to be true even in a strictly two-dimensional framework. It can then be inferred that the 'optimal' state suggested by RKW in which the updraughts should be vertical may not necessarily be the most efficient state energetically.

b) Experiment SLE1B

The squall line obtained in experiment SLE1B is also intense and steady. In fact, it is

even more steady than the one in SLE1C which produces the maximum rainfall. The simulation is extended further to 10 hours and the surface rainfall rate during the extra 4hrs is shown in Fig.5.22. Clearly the system has been remarkably steady throughout the later 8hrs. This squall line differs from that in SLE1C in that it propagates at an almost constant speed relative to the ground, as a consequence of weaker low-level inflow. The propagation speed of the cold pool, therefore, of the system is about 2.5m/s, so that the line relative inflow speed is 17.5m/s. This relative speed is very close to the low-level inflow speed (18m/s) in SLE1B, in which the cold pool is essentially stationary at the early stage. As the CPF propagates relative to the ground, it also moves relative to the mid-level flow. A flow of 2.5m/s towards the line is enough to tilt the updraught lying in its way downstream (upshear). An upshear tilting updraught is clearly shown in Fig.5.23a, i.e. the flow field at 60min. This intense and narrow updraught is also indicated by the θ_e contours in Fig.5.23b. During the next hour (up to 120min), the system evolves gradually towards a quasi-steady state, and then remains steady and propagates at an almost fixed speed for 8 hours of model simulation. The convection at the end of the simulation is as vigorous as it was at 2hrs.

Fig.5.22. The surface rainfall rate between 6 and 10hrs of the model simulation (experiment SLE1B). The rainfall rate before 6hrs for the same simulation is shown in Fig.5.15.

Fig.5.23. The flow fields (left panel) and the θ_e fields (right) from experiment SLE1B, in which the step inflow speed is 15m/s. The squall line obtained is very steady. (Note the picture translation with time).

Throughout this period of steady evolution, the flow field is typified by a major jump type updraught, a weak overturning updraught, a strong rotor and a downdraught together with strong rear-to-front inflow.

Since the squall line is moving relative to the air at all levels, it can be expected that certain mid-level air will pass through the line to arrive at the rear of the line. This is evident in Fig.5.23d as shown by the θ_e-tracer. A low-θ_e blob is seen swimming in the middle of high-θ_e air towards the rear of the line to feed into the cold pool. Directly above x=15km, a new cell is seen forming, which would soon trap another blob of low-θ_e air to it left, and this blob of air will presumably follow a similar trajectory as the one now situated to its left. It is suggested that the line-relative motion of ambient air flow at all levels is also important in ensuring the steadiness of the squall line. Since in such case, the line moves into an environment whose conditions are hardly changed from the initial ones. Such a steadiness can not be expected to last for very long if the squall line is stationary (relative to the ground and to the mid-level air), since the whole troposphere would be quickly stabilized by the vigorous convection.

c) Comparison of experiments with step inflow: What determines the tilt of updraught?

The flow fields at 1hr and 3hrs from experiment SLE1A to D are put together in Fig.5.24 and Fig.5.25. It can be seen that the tilt of the updraught is clearly dependent on the magnitude of the low-level inflow: The updraught turns from upshear-tilting to downshear-tilting with the increase in the low-level inflow speed. Since most of the low-level inflow has zero-vorticity, we can not argue that it is the vorticity balance between the inflow and the cold pool that induces an updraught of vertical orientation as we have seen in SLE1C (Fig.5.14c).

Fig.5.24. The flow fields at t=60min from experiment (a) SLE1A, (b) SLE1B, (c) SLE1C and (d) SLE1D. The circulation shown is at the initial development stage of the squall line. The updraughts in all cases are intense at this time, but their orientations are very different. The orientation of the updraught is a strong function of the speed of the low-level inflow, in other words, a function of the mid-level system-relative flow since the line is propagating at a different speed. We argue here that it is the subcloud-cloud layer relative shear that dictates the tilt of updraught while the vorticity (zero here) in the low-level flow is only of secondary importance.

Fig.5.25. As in Fig.24, but at 180min.

Fig.5.26. Schematic diagram illustrating the way in which the interaction between the low-level inflow and the rain-induced cold pool occurs depending on their relative strength, and how this determines the tilt of the updraught. The C in the figure is the propagation speed of the CPF relative to ground, which is mainly dependent on the cross frontal pressure jump and the speed of the inflow. In the above three cases, the strength of cold pool is assumed to be the same but the magnitude of low-level inflow U increases from case (a) to case (b) as indicated by the inflow profiles in the figure. x=0 is the initial position of the cold pool, the final position of the cold pool is shown by the cold front indicator. The bold arrow near the cold pool front indicates the displacement of the CPF as a result of the imbalance between the front and the low-level inflow. In case (a), the inflow is not strong enough to balance the pressure force induced by the cold pool at the front so that the CPF surges ahead (C>0) inducing a deep anti-clockwise circulation as shown by the circle in picture (a). This circulation then forces the updraught to tilt upshear. Case (c) is just the opposite; the inflow is very strong so that the CPF recedes (C<0) inducing a deep clockwise circulation which forces that updraught to tilt downshear. In case (b) the cold pool and the inflow are just in balance so that the CPF is stationary (C=0). The air lifted at the CPF in this case enters the undisturbed middle levels to establish an upright updraught.

A close examination of Fig.5.25 reveals that the consequence of the interaction between the low-level inflow and the cold pool is best signified by the movement of the CPF. In case of weak inflow, the cold pool is strong enough to propagate forward through the inflow as in SLE1A and SLE1B. An immediate result of this is that an anti-clockwise deep circulation is set up through mass continuity. This circulation acts to effectively tilt the updraught upshear (Fig.5.24a,b). On the other hand, when the inflow is too strong for the cold pool to resist, the cold pool would recede which then introduces a clockwise circulation that in turn forces the updraught to tilt downshear (Fig.5.24d). Fig.5.24c shows a case in which the cold pool and the inflow is almost in an exact balance so that the CPF is stationary. The inflow is decelerated to be stationary at the CPF, and is lifted upwards and then enters the mid-troposphere that is hardly disturbed to form a vertical updraught. But it should be pointed out that the maintenance of an exactly vertical updraught in a squall line system is not required in order to achieve a maximum efficiency in releasing the CAPE in the low-level flow. Our arguments on how the interaction between the cold pool and the low-level inflow determines the updraught slope is illustrated schematically in Fig.5.26.

The dependence of the updraught tilt on the relative strength of inflow and cold pool is further illustrated by the model-simulated flow fields at 3hrs (Fig.5.25). By this time, the CPF has propagated over a different distance in each case. The updraught in all cases except in SLE1D is tilting upshear. In SLE1C, the updraught turns from the vertical direction to upshear in response the intensification of cold pool, but the cold pool and inflow are still roughly in balance. Fig.5.15 shows that at this time the squall line in SLE1C is most efficient in producing precipitation.

5.4.2 Shear type inflow

The rainfall rates at the surface from experiments with shear type inflow (SLE2A-D) are shown in Fig.5.27. It is clear that the line propagation speed is strongly dependent on the inflow magnitude; the line in SLE2A is fast propagating whereas the line in SLE2D (U_0=28m/s) is stationary if not receding. The convection is most vigorous in SLE2A and SLE2B but very weak in SLE2C and SLE2D. In the later two, the low-level shear is so strong as to suppress severely deep convection. It is also evident (Fig.5.27) that as the mid-level system-relative front-to-rear flow increases, the system becomes increasingly multicellular, and the line relative speed at which the individual cells moves away from the line where it is generated increases also. The accumulated rainfall in the domain from each line is plotted against time in Fig.5.28. The overall precipitation from these lines are much lower than those with step type inflow. The case with a shear magnitude of 15m/s over 2km produces maximum rainfall whereas hardly any rain is produced by line SLE1D. It is therefore suggested that the shear in the low-level inflow is detrimental to rather than favourable for strong, deep convection, and for a given environmental sounding, there exists a preferred magnitude of shear with which the squall line convection is most vigorous. This preferred condition can also be understood through the mechanism we suggested previously (Fig.5.26) in terms of the inter-balance between the low-level inflow and the cold pool. A maximum efficiency of rain-generation is achieved when the inflow is just strong enough to keep the cold pool front stationary or propagating slowly relative to the mid-level flow.

The flow fields at 1hr and 3hrs from four experiments are given in Fig.5.29 and Fig.5.30. The CPF in SLE2A (Fig.5.29a, U_0=10m/s) moved forward by 14km during the initial one hour, consistently the updraught is seen tilting upshear although individual updraught cores are nearly vertical. The updraught that forms in SLE2B (U_0=15m/s) is almost exactly vertical at 60min, with the entire low-level inflow being drawn up into the updraught. The other two cases with stronger low-level shear have much weaker updraughts, with most of the inflow air running through under the convective area. In

these two case, there is a tendency for the cold pool to recede, but it appears stationary because it is being fed by evaporation cooled air from the convection. By 3hrs, the convection in the later two cases remains very weak, whereas the other two squall lines experience steady evolution (Fig.5.30). The line in SEL2A propagates faster and the multicellular structure is most pronounced, with four separate updraught cores being identifiable in Fig.5.30a. The corresponding θ_e field (not shown) indicates that the cold pool is also fed by the air from mid-level at the front of the line.

Fig.5.27. The surface rainfall rate as a function of time for experiments (a) SLE2A , (b) SLE2B, (c) SLE2C, and (d) SLE2D.

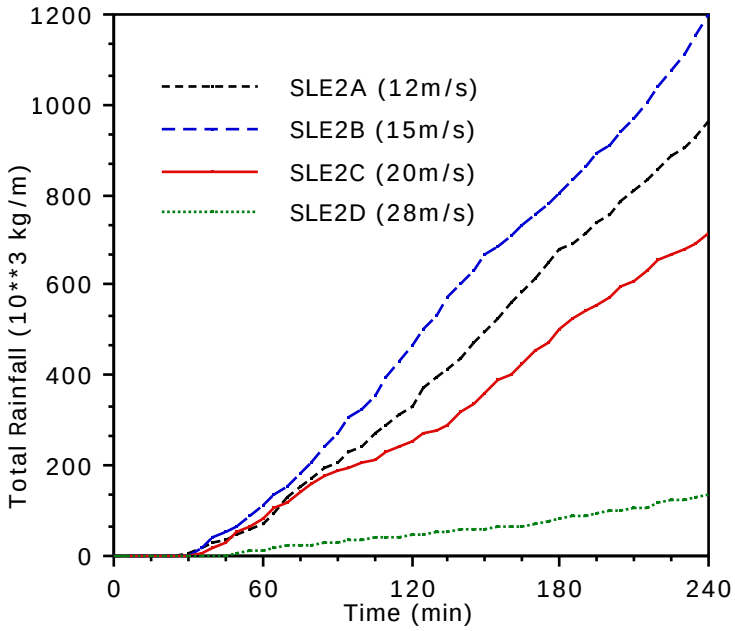

Fig.5.28 The accumulated surface rainfall in the model domain produced by squall lines (as indicated in the diagram) with a shear type low-level inflow. It can be seen that a 15m/s shear inflow produces the maximum rainfall (SLE2B), therefore the most active squall line.

In conclusion, the results of the experiments with shear type inflow again lend support to the mechanism we suggested, by which the interaction between the low-level flow and the cold pool in terms of their relative strength determines the development and evolution of squall line systems. The important role of the low-level inflow is to stop the cold pool from propagating too rapidly relative to the mid-level flow, but the cold pool should also be strong enough to resist the inflow so as to maintain a vertical-to-upshear tilting updraught. The vorticity in the low-level in flow is only of secondary importance in determining the tilt of updraught. A stationary or slow-propagating cold pool relative to the mid-level air flow, as a result a slightly upshear tilting updraught, is optimal to allow for a vigorous, long-lived squall line.

Fig.5.29. The flow fields at 60min from experiments with shear type inflow. They are for (a) SLE2A, (B) SLE2B, (c) SLE2C and (d) SLE2D.

Fig.5.30. The flow fields at 180min from experiments with shear type inflow. They are for (a) SLE2A, (B) SLE2B, (c) SLE2C and (d) SLE2D.

5.4.3 Jet type inflow

Another experiment (SLE3A) is performed with a jet type low-level inflow. This inflow has a maximum of 18m/s at 1.5km level, and decreases linearly to 10m/s at z=0.0km and to 0.0m/s at and above 2.0km.

Fig.5.31. The flow fields at (a) 60min and (b) 240min of the simulated squall line in a jet type low-level shear. (c) The field of θ_e at 240min of this simulation.

Since the inflow at the ground level is weak, the strong cold pool enhanced by evaporation from a wide area of rain pushes its way ahead very quickly through the inflow, inducing a strong compensating anti-clockwise circulation which together with the strong inflow at 1.5km level swamps the lifted air rapidly to the rear of the front line. (Fig.5.31). Deep convection is only seen considerably a long distance to the rear of the front line where the prohibiting circulation and water drag are weaker. The θ_e field shows that at 240min, the cold pool consists largely of the air from ahead of the CPF, which is of higher θ_e. Due to the lack of vigorous, deep convection in the line, the total precipitation produced is very limited. In short, the development and evolution of the squall line in this experiment is consistent with our interpretation on the conditions for strong long-lived squall lines.

5.5 The optimal conditions for intense, long-lived squall lines

Our numerical experiments have shown that squall lines that develop in an ambient flow with a strong enough relative shear between the lower 2km and the layer above are mostly long-lived. However, the intensity of convection in the system depends strongly on the relative strength of the rain-induced cold pool outflow and the low-level ambient flow. When the cold pool is not strong enough to resist the low-level ambient flow, it would, at least tend to, recede. As a result, a deep circulation as indicated in F.g.5.26c would be induced which tends to tilt updraught downshear (with respect to the deep ambient shear). In this case the rain that falls overhead of the low-level inflow would be prohibitive to persistent deep convection, and as the rainwater evaporative cooling is limited the cold pool will be weak. On the other hand, when the low-level inflow is relatively weak, the cold pool would propagate forward so that the air above the cold pool is left behind. A deep circulation having an opposite direction as in previous case would then be induced (Fig.5.26a), which tends to tilt the updraught upshear. This case is regarded by RKW as being 'less than optimal', however, the upshear tilting orientation of

updraught is generally considered the most effective (e.g. Browning, 1977). The extremely persistent convection in the squall line obtained in SLE1B clearly supports the latter view. In such a situation, the rain falls from the upshear tilting updraught without interrupting the low-level inflow. Moreover, the rain evaporation at the mid- and low-levels beneath the tilting updraught would strongly enhance the cold pool. Since there exists a lower limit to the cold pool temperature (determined by the minimum θ_e in the domain), a quasi-steady state with cold pool temperature fixed could be eventually established. Provided that the CPF does not move too rapidly (within a few meters per second) relative to the air above the cold pool, a upshear tilting but still deep and persistent updraught can be maintained in which there may be a number of updraught cores related to individual cells at different stages of their life cycle. In the intermediate case in which the cold pool is roughly in balance with the low-level inflow, the cold pool would hardly move. The inflow would then be lifted at the CPF and enter the scarcely disturbed mid-layer to form an erect updraught (Fig.5.26b). Although the updraught developed in this case can be more vigorous than in the upshear tilting case, it would not be as persistent. It will be periodically disrupted by heavy liquid water loading. Moreover, this state with vertically symmetric convective circulations can not last for very long since the latent heating accumulated at the mid- and high-levels would soon change the environmental conditions.

Based on the above arguments, we propose here the optimal conditions for long-lived, intense squall lines. Assuming the environment has an uniform flow of speed U_0 (<0) below $z=H_1$, and zero flow above, the optimal state requires that the cold pool propagation speed relative to the ground, hence relative to the air above the cold pool also, be zero or slightly greater (forward) than zero, namely

$$C = k\,(\Delta\Phi')^{1/2} + \alpha\, U_0 \geq 0. \qquad (5.5.1)$$

Here $\Delta\Phi'$ is the jump in geopotential height across cold pool front, k and α are two non-dimensional parameters. When $C\geq 0$, its value should be within a few meters per second.

Formula (5.5.1) is based on the speed of atmospheric density current propagating in an atmosphere at rest. Seitter (1986) gave a formula of the speed as

$$C_* = k\,(\Delta p/\bar{\rho})^{1/2}, \qquad (5.5.2)$$

where the Δp is the pressure jump across density current head (cold pool front) and $\bar{\rho}$ the average density inside the density current head. This pressure jump includes the contributions from not only the temperature deficit inside the density current (cold pool), but also warming in the updraught, water loading and nonhydrostatic effects. It is therefore more accurate than the classical formula for density current propagation which takes into account of the density deficit only (Benjamin, 1968). k=1.1 is suggested by Seitter (1986) based on numerical experiments.

When a density current propagates in an environment with opposing inflow, its speed is given by Thorpe, et. al. (1980) as

$$C = C_* + \alpha\, U_{0,} \qquad (5.5.3)$$

where C_* is the density current speed without opposing flow, and U_0 is the ground relative inflow speed α=0.7 is suggested by Thorpe, et.al when calculating C_* based on temperature buoyancy only. A larger value of about 0.9 is more appropriate according to our later experiments.

Condition (5.5.1) can be rewritten as

$$|U_0| \le k'\,(\Delta\Phi')^{1/2} \equiv C_*/\alpha, \qquad (5.5.4)$$

i.e. the inflow speed, adjusted by factor α (of the order one), is equal to or slightly less than the absolute density current propagation speed C_* (here $k'=k/\alpha$).

The optimal condition given by RKW is

$$\Delta U = k\,[\int_0^H (-B)dz\,]^{1/2} \equiv c \qquad (5.5.5)$$

where ΔU represents the wind difference across the low-level environmental shear, B represents the full buoyancy term, including water loading, and H is the level where negative buoyancy first vanishes. $k=\sqrt{2}$ as is given in their formula, but a smaller value

of about 1.0 was also suggested when the propagation of the cold pool was discussed taking diffusion into account. Therefore c in (5.5.5) and C_* in (5.5.4) are both the prediction of cold pool propagation speed. Regardless of the exact equality required in (5.5.5), condition (5.5.4) and (5.5.5) predicts essentially the same dividing line of the magnitude of the low-level inflow, but the interpretations of them are very different. RKW obtained condition (5.5.5) based on the assumption that the low-level inflow is sheared, and ΔU is the magnitude of shear across depth H. The flux of vorticity in this sheared flow should balance exactly the generation of vorticity of opposite sign at the cold pool front. This condition is obviously not consistent with the results of our numerical experiments in which the low-level inflow has a constant speed therefore zero vorticity. To obtain condition (5.5.5), RKW also neglected the fact that the diminution of vorticity in the inflow is not possible unless there is a thorough mixing between the inflow and the cold pool air. This is clearly not occurring in the model simulations. We think that the role of the inflow is to control the propagation of the cold pool outflow so that a slightly upshear tilting updraught is maintained, rather than to provide vorticity to be destroyed by the cold pool. The vorticity possessed by the air lifted to enter the updraught has only a secondary effect on the orientation of updraught.

The condition (5.5.4) is verified against the results of our experiments with step type flow. In SLE1B, SLE1C and SLE1D, the ground relative propagation speed of the CPF is respectively positive, nearly zero and negative. With reference to the surface rainfall pattern in Fig.5.15, we chose a relatively steady period of one hour for each case for testing calculations. They are 1 to 2hrs for SLE1C and SLE1D, and 2 to 3hrs for SLE1B. The cross frontal jump in geopotential height perturbation Φ' is calculated as the average of Φ' at the beginning, middle and end of each one hour period. The corresponding curves of Φ' at the surface are shown in Fig.5.32. The values of C_* calculated according to (5.5.4) are listed in Table.5.3, together with the inflow speed (U_0) and the ground relative speed of CPF (C) calculated from the actual CPF positions.

It can be seen that for the nearly stationary case SLE1C, C_*=17.2, this is very close

to the absolute speed of inflow (18m/s). For the upshear tilting (also forward propagating) case SLE1B, $|U_0|<C_*$ and for SLE1D in which the updraught remains downshear tilting and the cold pool recedes, $|U_0|>C_*$. These are clearly consistent with our previous discussions on how the inflow controls the propagation and further the development and evolution of a squall line. Condition (5.54) gives a good guide line towards our understanding of squall line dynamics. Finally by fitting in the values of C_*, U_0 and C into formula (5.5.3) we find an average value of 0.89 for factor α. Therefore we suggest $\alpha=0.9$ being most appropriate in formula (5.5.3).

Fig.5.32. The curves of the geopotential height perturbations at $\sigma=1$ showing the pressure jump across the cold pool front within squall lines obtained in experiment SLE1B (upper panel), SLE1C (middle panel) and SLE1D (lower panel). The curves are plotted as Φ'/g (m).

Table.5.3. Verification of the propagation speed of cold pool and the condition for intense and long-lived squall lines with experiments SLE1B, SLE1C and SLE1D

Experiment	$\overline{\Delta\Phi'}/g$	C_* (m/s)	U_0 (m/s)	C (m/s)	α
SLE1B	22.0	16.15	-15.0	2.8	0.89
SLE1C	25.0	17.22	-18.0	0.35	0.94
SLE1D	35.3	20.47	-25.0	-0.56	0.84

Furthermore, Table.5.3 shows that $\Delta\Phi'$ in SLE1D is greater than in SLE1B, but the cold pool in SLE1D is considerably weaker. This suggests that the contribution to the cross frontal pressure jump from other factors, in particular the warming above the cold pool, are significant. The strong heating overhead of the cold pool in SLE1B (also in SLE1C, see Fig.5.21) considerably reduces the pressure at the surface.

5.6 Sensitivity of squall line simulations to diffusion

As is listed in Table.5.2, four experiments are performed with other model settings exactly the same as in the maximum rain-production experiment SLE1C, except that different formulations or magnitudes of diffusion are used. In experiment SLE4A and SLE4B, the Richardson number and deformation dependent diffusion is switched off as in SLE1C, but a smaller ($20m^2/s$) or larger ($200m^2/s$) coefficient (K_{BG}) of constant background diffusion is used. In SLE5A and SLE5B, the former diffusion is activated and $K_{BG}=20m^2/s$ and $100m^2/s$ respectively.

The rainfall rate from each of the four experiments is plotted against time in Fig.5.33, the time series of maximum and minimum θ' are shown in Fig.5.34. In Fig.5.35 are the flow fields at 3hrs from these experiments. It can be seen that SLE4B is most rain-productive while SLE5A is the least. On the whole, the squall lines are mostly intense and long-lived, consistent with the prediction made according our optimal condition (5.5.4).

Fig.5.33. The rainfall rate at the surface plotted against time for experiment SLE4A (a), SLE4B (b), SLE5A (c) and SLE5B (d).

Fig.5.34. The time series of θ'_{max} and θ'_{min} for respectively experiment SLE4A (a), SLE4B (b), SLE5A (c) and SLE5B (d).

In SLE4A, the diffusion is much weaker than in all the other three, as a result, the cold pool is the strongest and is established earlier (θ'=-9.5K at 100min, Fig.5.34) The strength of the cold pool enables it to propagate forward against the inflow, inducing a strongly upshear tilted updraught. Fig.5.35a shows that the flow field at 3hrs of this experiment is fairly similar to that in SLE1B. This system should be expected to be also long-lived if the upstream conditions are properly maintained (the background diffusion helps to maintain the initial environmental state). The evolution of the squall line in SLE4B is very similar to that in SLE1C (cf. Fig.5.15c); both systems are intense and nearly stationary. Only that the cold pool at the early time (50-130min) is weaker in SLE4B, due to stronger diffusion on the temperature perturbation. Accordingly, the system is seen receding slightly first in SLE4B, but it remains stationary in SLE1C. By 240min, the cold pool in both cases has a similar strength, the subsequent evolutions of two systems are much the same. The squall line in SLE4B is very intense (Fig.5.35b).

Fig.5.35. The flow fields at 180min of the squall line in experiment SLE4A (a), SLE4B (b), SLE5A (c) and SLE5B (d).

In the other two experiments (SLE5A, SLE5B), the time evolution of system appears to be somewhat different. Both systems experienced a period of 'single cell redevelopment' (from 120 to 225min in SLE5A and 90 to 135min in SLE5B). Within this period, the system appears to be unicellular. The cell life cycle in rather short, the period of cell regeneration is only about 11 minutes (Fig.5.33c,d). During this period, the cold pool is relatively weak (Fig.5.34c,d) and the updraughts are vertically oriented. At t=225min in SLE5A and 135min in SLE5B, the cold pool is evidently enhanced (Fig.5.34c,d), corresponding to this, the surface rainfall pattern exhibits a distinct change from unicellular to multicellular one. At the same time, the updraught changes from more or less vertical to upshear orientation. The convection is since more vigorous and persistent, the flow field becomes similar to those in SLE1C and SLE4B. We show in Fig.5.35 the flow fields at t=180mins for SLE5A and SEL5B, they happen to be at different stages of development in each case.

In general, the squall lines in all of the above experiments are long-lived and nearly stationary. This is consistent with our discussions in section 5.5. However, the time taken in each experiment to establish a rain-productive system with an upshear oriented updraught differs greatly. It is fairly quick when the constant background diffusion only is included (≤2hrs) and even quicker when K_{BG} is smaller, but it takes up to 4 hours to reach that state in experiment SLE5A in which K(Ri, Def)≠0 and K_{BG} is small. These experiments show the diffusion does affect the time evolution (especially the timing) of simulated squall lines, but it would not change very much the final state of a mature squall line which is mainly controlled by the relative strength of cold pool and low-level inflow.

5.7 Summary

A series of experiments of two-dimensional squall lines have been performed using our σ-coordinate model. The results agree with the finding of TMM and RKW that the interaction between the rain-induced cold pool and the low-level inflow plays a crucial role in maintaining an intense, long-lived squall line. However, the results of our experiments do not support RKW's argument that the orientation of the updraught is solely dictated by the net vorticity in the updraught air. Rather, we believe that the orientation of updraught is mainly controlled by the flow speed at the cloud (mid-) levels relative to that of the cold pool front at which the inflow air is lifted, whereas this relative speed is related to the deep environmental shear between the sub-cloud layer and the cloud layer, when the intensity of cold pool is roughly fixed. This deep shear is required so that the cold pool propagates at a considerable speed relative to inflow air but not relative to the cloud layer flow. To achieve this, we do not require vorticity in the low-level flow. The mechanism of vorticity balance happens to predict a magnitude of low-level shear agreeing with the results of numerical experiments (RKW) (the evaluations of certain parameters are rather arbitrary). But such a success comes for the wrong reasons. The low-level shear in their case is to, just like the un-sheared low-level inflow in our case, produce a pressure force to balance the pressure gradient produced by the total buoyancy at the cold pool head, such that the cold pool does not propagate rapidly relative the air above the cold pool. This conclusion is in line with that of TMM.

The slightly upshear tilting orientation is shown to be the most effective one of updraught, just as suggested by classical conceptual models of 2-D squall lines. An exactly vertical updraught may be vigorous but has to be intermittent due to liquid water loading. Moreover, even in a strictly two dimensional framework, a quasi-steady squall line system is still possible, and the system can even propagate relative to flows at all levels. This being possible is because that the system is in most cases multicellular, in which new cells are continually generated at the front line and sometimes moved rather rapidly rearwards and air in front of the line can pass the line through in-between the gaps

of individual cells.

The experiments with low-level sheared inflow of different magnitudes show results consistent with the prediction made according to our optimal condition, and that the updraughts in these cases are less intense than in the step inflow cases.

Diffusion is found to be able to affect the timing of squall line evolution, but not to the extend as to change the final state of long-lived squall lines.

Supercell type convective storms generally exist in an environment of deep and strong shear, and they have three dimensional structures (Browning, 1977). This type of deep convectrion is not considered here.

Chapter Six

Deep Orographic Convection - Numerical Study on The Big Thompson Storm

6.1 Introduction

Compared with squall line type convection and broad scale orographic precipitation systems, deep orographic convection is an area not much studied, part of the reason is that fewer observational events have been documented due to the smallness of such systems and the attachment of them to particular geographical locations. The lack of modeling studies is mainly because the simulations of these systems require appropriately formulated numerical models (being capable of dealing with irregular orography) as well as a rather large amount of computing resources. In spite of these, Orville (1965) in the sixties managed to carried out some numerical studies on convection over an idealized ridge. In his case, the ridge was composed of two straight slopes with the slopes being coincident with rectangular grid mesh. The effect of ambient winds were examined. Later on, numerical models with terrain-following coordinate transformation emerged in the mid-seventies (Gal-Chen and Somerville, 1975, and Clark, 1976), but still little effort has been devoted to problems of deep orographic convection. In our nonhydrostatic sigma-coordinate model, both the convective processes and orographic effects are included, it is therefore an ideal tool to study problems in this area.

There are some observational studies in the literature on convective processes over mountains. The best documented events may be the Big Thompson storm that occurred

over the Big Thompson Canyon, east of Continental Divide, Rocky Mountains on the 31 July to 1 August, 1976. On that day, a large quasi-stationary thunderstorm complex formed over the Big Thompson river drainage west of Loveland, Colorado, and intense rainfall produced devastating flash floods that cost many lives. It is this event that we are going to study using our numerical model. Other observational studies include Grossman and Durran (1984), in which the orographic convection due to interaction between monsoon flow and the coastal mountains of the Indian sub-continent was examined.

A detailed analysis of the meteorological conditions which culminated in the Big Thompson floods was presented in Maddox et al. (1978). They were summarized in Caracena et al. (1979) as follows:

1) At upper levels (500-300hPa), the flow around a negatively tilted ridge was light southeasterly over the Front Range area of Colorado.

2) A short-wave trough on the meso-α scale (at 500hPa) was approaching the region from the south along the west side of the ridge.

3) A polar air mass lay to the northeast of the Front Range, with the polar front stretching across southeastern Colorado.

4) During the day, increasing surface pressure over Nebraska and northeastern Colorado, and falling pressure over northwestern Colorado, accelerated a secondary cold frontal surge that reached the foothill of the Front Range about 0000 GMT 1 August 1976.

5) Behind the secondary cold front, a deep moist flow in the boundary layer carried potentially very unstable air upslope. The strong moisture intrusion focused on the Big Thompson area. The storm complex developed over the Big Thompson river drainage and remained quasi-stationary for several hours.

Fig.6.1. Skew *T*/log*p* plot of upper air sounding constructed for Loveland, Colorado, 0000 GMT 1 August 1976. LCL and LFC levels and moist adiabats are shown for a lifted parcel with mean thermodynamic characteristics of lowest 100hPa layer.

Fig.6.2. Heavy rainfall components accumulated throughout the lifetime of the storm from 0000 to 0500 GMT 1 August 1976. (From Caracena et al. 1979)

Caracena, et al. (1979) further analysed the mesoscale features and cloud microphysical aspects of the Big Thompson storm, making use of radar data and surface observation, rain gauge data. A post-frontal sounding profile was constructed based on various sources of information for Loveland, Colorado (about 30km from the major mountain ridge), 0000GMT, 1 August 1976. The skew $T/\log p$ plot of the sounding is reproduced in Fig.6.1. The air between the surface and the 730hPa is very moist (mean mixing ratio 14.8g/kg) so that the air mass is convectively very unstable. As is shown in Fig.6.1, the post-frontal air mass is however capped by a strong frontal inversion at 730hPa, which is also the height of lifted condensation level (LCL). An additional 80hPa of lift is necessary to bring this air to its LFC and release its strong potential instability. This additional lifting was realized as the air mass moved up into the foothills. Meanwhile, other convection over the plains was suppressed by the nocturnal cooling so that a steady inflow into the storm was established and continued to feed the quasi-stationary storm. Fig.6.1 also shows that the air in the inversion was rather dry, corresponding to low-θ_e values there. If this low-θ_e air is brought to ground levels (say in the form of downdraught) it will be considerably colder than the inflow air. This suggests a potential for a strong cold outflow to form. Fig.6.1. further indicates that strong flow is limited to a 1.5km deep surface layer, while the wind aloft is very light. Such a wind profile is favourable for long-lived squall line system as was discussed in last chapter.

The total accumulation of heavy rain from the storm estimated according to radar data is shown in Fig.6.2. The maximum rainfall accumulated is 178mm (7.0 inches). Although several maximum centres are visible the overall rainfall pattern is aligned with the mountain ridge, and the north-south extent of the storm is much longer than its east-west scale. The storm can therefore be regarded as two dimensional to the first approximation.

Fig.6.3. Physical model of one of the initial cells of the Big Thompson storm complex. LCL, LFC, winds and levels of 0^0C and the -25^0C isotherms are from interpolated Loveland sounding. Grover 0045 radar reflectivities are shown with 10dBZ contours beginning with 15 dBZ level.

A physical model has been given by Caracena, et al. (1979) for this storm. It is depicted in Fig.6.3, in which the contours with shading show the radar reflectivity (dBZ) in a cross section through one of the initial cells at 0045 GMT. According to the model, a strong low-level inflow produces a strong moisture and mass flux into the storm area, and is lifted above the LCL on approaching the Front Range. Stratus and stratocumulus clouds form first in the 80hPa thick layer between the cloud base and the LFC. Further on at some point along the mountainous topography the air mass is forced above the LFC and vigorous convection develops. With the vertical transport of the easterly momentum into the storm and very light winds at high levels, the updraught tilts slightly in the direction of the inflow to the west, and this westward tilted updraught allows precipitation to fall out of the rear of the updraught, enabling the system to exist in a nearly steady

state. The downdraught circulation was found very weak in the system, which was attributed to the lack of appreciable hail therefore weaker drag, cloud base very close to the surface and the lifting of the mountain terrain. The cold outflow did not spread eastward out of the mountains to trigger new cells further east. Warm rain processes are believed to play the major role in generating storm precipitation, as is evidenced by the low echo-centroid and lack of hail. A very high precipitation efficiency (total precipitation to the total low-level moisture influx) of up to 85% was achieved by the storm, helped by the minimal lose of rainwater by evaporation in the rather weak downdraught circulation.

In the next section we will give a list and the specifications of two dimensional numerical experiments with the Loveland sounding. The results of these will be presented in section 6.3 and some discussions and conclusions will be found in the last section.

6.2 Experimental designs

The model initialization procedure is essentially the same as that for the simulations of moist mountain lee waves in Chapter four. The initial state for all the following experiments are in hydrostatic balance. The model is initialized from a given sounding profile of temperature and humidity, therefore the initial state is a function of height or pressure only. Also the initial flow field depends on height only. The specified mountain is introduced at the beginning of simulations therefore a period, but generally very short period of adjustment is required after setting up.

The pressure at the ground level, $P_{surf}(\Phi_s=0)$, is 850hPa, and this is chosen to match the pressure at the surface of the high plain to the east of the mountain range. For all the experiments, we have P_{top}=100hPa, a 256km horizontal model domain with Δx=1km, and 40 levels in the vertical so that $\Delta\sigma$=1/40. Time step Δt=6s. Richardson number and deformation dependent mixing parameterization is activated and a constant background diffusion with K_{BG}=100.0m^2/s is incorporated.

The sounding profiles used as model input are re-plotted in Fig.6.4 on a Tephigram

(T-lnθ). The temperature profile is unchanged in all the experiments but the moisture profile is modified at mid-levels (thin dashed line in Fig.6.4) in the second set of experiments (DOC2A-C), we will refer to these cases as modified moisture sounding cases. The upstream wind profile is given in Fig.6.5 which shows that inflow is mainly below 2.5km AGL, with a jet at the 1.0km level. This profile is in a broad sense similar to those used in the squall line experiments in the last chapter.

Fig.6.4. Tephigram of sounding profiles used as model input of deep orographic convection experiments. They are based on the Loveland sounding given in Fig.6.1. Straight lines at right angle to each other are isotherms and dry adiabats. Lines lying roughly horizontally are isobars. The temperature profile is in bold solid line and the moisture profiles are in dashed lines, with the bold being the standard and the thin one being the modified one.

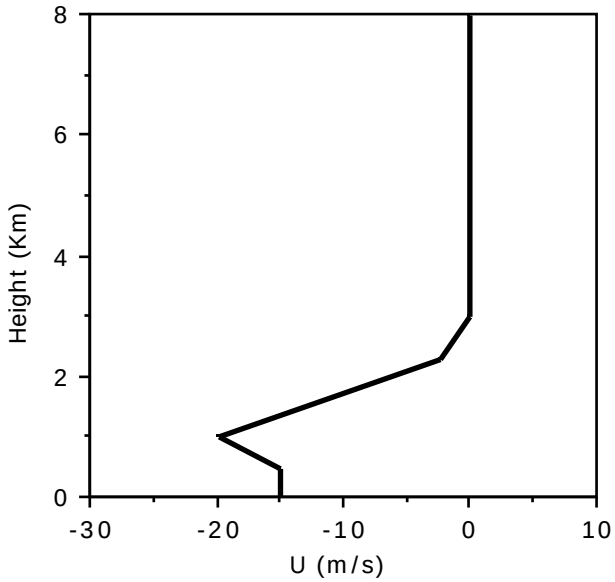

Fig.6.5. The initial upstream wind profile used in all experiments of deep orographic convection. All winds are seen confined below 3.0km, with a jet at 1.0km level.

Three types of mountain shapes are used to represent the orography profile outlined in Fig.6.3. The first one is the symmetric bell-shaped mountain (SBM) given by $h(x)=h_m/[1+(x-x_0)^2/a_1^2]$ with h_m being the maximum height and a_1 the half-width of the mountain (see Fig.6.6a). The second is the asymmetric bell-shaped mountain (ABM, Fig.6.6b) which is actually composed of opposite haves of two bell-shaped mountains of scales a_1 and a_2 respectively. The third is the plateau type mountain consisting of a flat high plain joined up with half a bell-shaped mountain (PBM) as shown in Fig.6.6c. In all the experiments, the half-width of the bell-shaped mountain on the windward side a_1 is 10km, while the half-width of the left portion of the asymmetric bell-shaped mountain a_2 is 50km. The specifications of the three sets of experiments of deep orographic convection (simulations of the Great Thompson storm) are listed in Table.6.1.

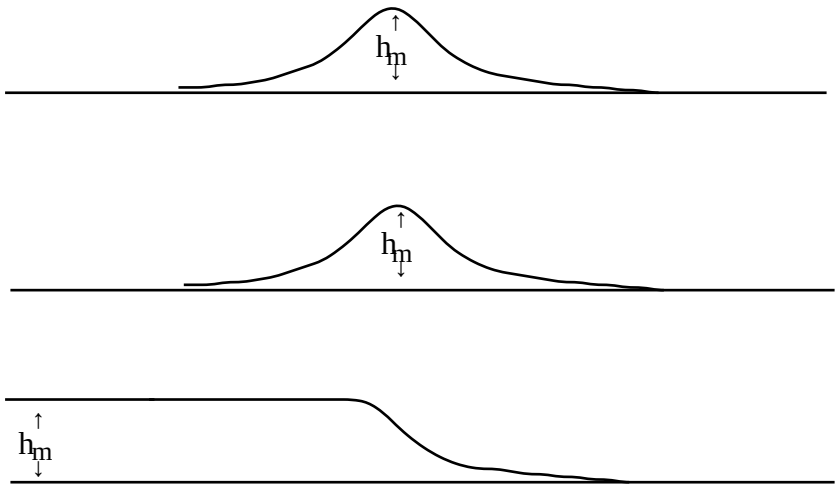

Fig.6.6. Sketches of three mountain profiles used to present the orography that forces the Big Thompson storm.

Table.6.1. Specifications of deep orographic convection (DOC) experiments.

Experiment	Mountain shape	Height h_m(km)	Moisture profile
DOC1A	Symmetric Bell-shaped (SBM)	1.8	Standard
DOC1B	Asymmetric Bell-shaped (ABM)	"	"
DOC1C	Plateau + Bell-shaped (PBM)	"	"
DOC2A	SBM	1.8	Modified
DOC2B	ABM	"	"
DOC2C	PBM	"	"
DOC3A	SBM	1.0	Standard
DOC3B	ABM	"	"
DOC3C	PBM	"	"

6.3 Results of experiments

In this section, three sets of experiments are to be reported. Each set includes three experiments that use different mountain profiles. For all the experiments in the first set (DOC1A-C), standard sounding profiles are used and the maximum mountain height h_m is 1.8km. In the second set (DOC2A-C), the moisture sounding is modified at the low levels to remove the dry layer there (see Fig.6.4) with the other specifications remaining

the same. The last set of experiments differs from the first one only in the height of the mountain which is now 1.0km.

6.3.1 Experiments with standard sounding

The standard sounding (shown in bold lines in Fig.6.4) has a fairly dry layer at about 700hPa (about 1.5km AGL) corresponding to the layer of inversion. The θ_e is at a minimum at this layer, and is higher immediately below and above. The mid-level low θ_e layer is at about 500hPa, i.e. about 4.5km AGL. The existence of this low-level low θ_e layer suggests an increase in the potential for a strong cold pool if this air can descend low enough and be cooled by rain evaporation. Strong cold pools indeed form in certain experiments to be reported.

Fig.6.7. Hovmoeller diagrams of the surface rainfall rate (averaged over 2 minutes) in experiments DOC1A (a), DOC1B (b) and DOC1C (c) through four hours of model simulations. x=0 indicates the position of the mountain summit, or the edge of the flat plateau.

Fig.6.8 The wind vector fields in the vertical plane, at 1 to 4hrs from experiment DOC1A. The convection is forced by a symmetric bell-shaped mountain ridge. Thick lines in the pictures outline the cloud boundaries and the rainy areas are shaded. Wind vectors are plotted at every other grid points in horizontal and at all levels in the vertical, running average over 6km horizontal distances is performed on the wind fields for clarity of illustration.

Fig.6.9. Fields of potential temperature perturbation θ' and equivalent potential temperature θ_e at 3 and 4hrs from experiment DOC1A. In the former, areas with $\theta' \leq -1$K are heavily shaded to indicate the position of low-level cold pool. The layer with negative θ' between 1 to 2km is mainly induced by adiabatic cooling due to ascending motion in the inversion layer.

We start by showing the rainfall rates produced by the storms obtained in experiments DOC1A, DOC1B and DOC1C (Fig.6.7). The orographic convective systems in both DOC1A and DOC1B are intense and nearly stationary. Rain is seen first falling at near the summit of the mountain at half an hour, and individual cells are seen moving rearwards. The site of cell initiation shifts slightly downslope during the later hours with most of the rain still falling on the upwind slope of mountain. The convection in the case of asymmetric bell-shaped mountain is more intense than with the symmetric mountain (Fig.6.7a,b). The convective storm forced by a plateau type mountain however behaves very differently (Fig.6.7c); after being initiated on the upwind slope, it propagates rapidly downslope away from the mountain, and at the later time, it appears more like a usual squall line driven by a strong cold pool. The convection becomes very weak after 3hrs, being prohibited by the strong relative flow above the cold pool.

The flow fields at 1 to 4hrs of experiment DOC1A are shown in Fig.6.8. Only a portion of model domain is shown. The fields of potential temperature perturbation θ' and equivalent potential temperature θ_e at 3 and 4hrs are shown in Fig.6.9.

Similarly as depicted in the physical model of the Big Thompson storm proposed Caracena, et al. (1979), as the low-level moist inflow approaches the mountain range, it is forced up so that stratus clouds first form at above 1km levels AGL. As the air runs further upslope, it is lifted above its level of free convection, deep convection is then break out. At 1.0hr of model simulation, the cloud top is seen to be at 12km height already (Fig.6.8a), however, a large proportion of low-level inflow is running through over the mountain top and then descending on the lee slope of the bell-shaped ridge, this implies that the precipitation efficiency is not high at the moment. By 3hrs, it is seen from Fig.6.8c that the convective storm is at it full intensity, and the storm structure at this time bears a strong resemblance to the Big Thompson storm described by the physical model of Caracena et al. A vigorous updraught leans against the upwind slope of ridge in a slightly downwind direction, and the rain falls off the updraught directly over the mountain ridge. Downdraught is fairly weak. The air on the upwind slope above

z=0.5km is saturated, being rendered so partly by the evaporation of rain water, as a result it is slightly colder then its surrounding (Fig.6.9a). The air in this region is nearly stagnant therefore it enhances the lifting to the incoming flow. On the lee slope, there is a rather strong downslope flow. This flow is composed of both the air originating from the upwind side of the ridge and from the mid-levels on the lee side. By 4hrs, the convection becomes less vigorous as the updraught becomes more rearward tilted due to the intensification and the propagation of cold pool along the upwind slope. A rotor circulation associated with the cold pool front is now clearly exhibited in Fig.6.8d. The downstream (upshear) tilting of the updraught can be explained by the mechanism of cold pool and inflow interaction as was discussed in last chapter for squall lines.

On the whole, the convective systems obtained are intense and nearly stationary during the four hours of simulation.

Corresponding to Fig.6.8 and Fig.6.9, the flow fields and the temperature fields from experiments DOC1B with an asymmetric bell shaped mountain are given in Fig.6.10 and Fig.6.11. In a broad sense, the development and evolution of the orographic convection in this experiment are similar to those in simulation DOC1A. But in this case, the rotor circulation associated with the cold pool on the upwind slope establishes earlier and propagates by a longer distance during the period simulation. In this case, the lee slope of mountain ridge is much more gentle than that in DOC1A, as a result, the evaporation-cooled air at the top and on the lee slope of the ridge is not drained away as efficiently as in DOC1A (see Fig.6.9), instead it tends to pile on the mountain top and feed the cold pool on the upwind slope. This increases the pressure over the lee slope and drives the cold pool front downward along the slope. The position (at x=29km) of the cold pool front is clearly further away from the ridge top in DOC1B than in DOC1A (at x=19km).

Fig.6.10. As in Fig.6.8, but for experiment DOC1B in which the mountain asymmetric bell-shaped.

Fig.6.11. As in Fig.6.9, but for experiment DOC1B in which the mountain asymmetric bell-shaped.

upright

Fig.6.12. As in Fig.6.8, but for experiment DOC1C in which the mountain profile is of the plateau type. A larger portion of model domain is shown here. The storm in this case is rapidly propagating.

upright

Fig.6.13. Fields from DOC1C of (a) horizontal velocity u, (b) potential temperature perturbation and (c) equivalent potential temperature θ at 3 hours.

In general, simulations DOC1A and DOC1B captured the essential characteristics of the observed Big Thompson storm. The simulated storm structure resembles that described by the physical model of Caracena et. al. Heavy precipitation over the mountain ridge persists throughout the four hours of model simulations (rainfall rate exceeds 100mm per hour) although the storm consists of individual cells that are continually regenerated and undergo their own life cycles (Fig.6.7). It should be noted that the fields in Figs.6.8-11 are only snap shots of the evolving systems which do not necessarily show major cells in the system at their mature stages. The simulated storms exhibit slow propagation down the upwind slope as a result of the formation of a relatively weak cold pool. This is in fact not surprising considering the sounding profile used which has a layer of low-θ_e air at quite low levels. The θ_e fields in Fig.6.11 shows clearly that the cold pool consists of this low θ_e air ($\theta_e \leq 344$K). In experiment DOC1A, this low θ_e air appears only on the top of the ridge.

In DOC1C, the mountain profile is of the semi-infinite plateau type. It has been seen from the surface rainfall pattern in Fig.6.7 that the convective storm in this run is not stationary relative to the mountain, rather it propagates rapidly downslope and upstream.

Fig.6.12 displays the flow fields at one hour intervals up to 4 hours of model simulation. Fig.6.13 shows the fields of u, θ' and θ_e at 3hrs. The convection at 2 hrs is rather intense with the deep updraught tilting in the downwind direction. Different from previous cases, the downdraught in this case in very strong. It lies under the sloping updraught and brings mid-level low-θ_e air right down to the surface (Fig.6.12b). Due to a large contrast between the θ_e of the air at mid-levels and that of the low-level inflow, a cold pool with a very large temperature deficit ($\theta' \leq -11$K) is formed. This strong cold pool drives the system rapidly upstream against the inflow that is too weak to resist this strong cold pool. The rapid propagation of the cold pool relative to the air above prohibits deep convection resulting in the decay of the system (Fig.6.12).

In the previous cases of a bell-shaped mountain, much of the evaporation-cooled downdraught air was drained away along the lee slope of the ridge, so that the cold pool

on the upwind slope was much weaker, the convective storm therefore remained nearly stationary. In the case of plateau type mountain, the cold air is piled on the edge of the plateau, and much of it then find its way down the slope, enhancing the cold pool there (Fig.6.12b). This cold pool is rendered even deeper and stronger by the presence of the plateau that blocks the cold outflow in the left ward direction. Although we would not say that the storm obtained in this experiment (DOC1C) is a successful reproduction of the observed Big Thompson storm, its development and evolution are physically consistent with the given sounding and mountain profile.

In summary, using the pre-storm sounding of Loveland, attempts to reproduce the devastating event of Big Thompson storm were made by performing three experiments each of which uses a different mountain profile. The storms simulated in DOC1A and DOC1B with bell-shaped mountains were persistent and quasi-stationary, whereas that obtained in DOC1C with plateau type mountain was fast-propagating. It is suggested therefore if we are to believe in the representativeness of the environmental sounding used here which has a potential of producing strong cold pool, and we assume that the mountain and the storm itself are quasi-two-dimensional, the mountain profiles must then allow for the drainage of cold outflow from the lee of the ridge. In reality, probably neither the orography nor the storm is strictly two dimensional, so that the blocking effect as in case of a plateau would not be that strong.

As was pointed earlier, the presence of a dry, low-θ_e layer at the lower levels contributes positively to the formation of a strong cold pool, in next section, we will discuss the results of experiments in which this low-level low-θ_e layer is removed by modifying the moisture profile of environmental sounding.

6.3.2 Experiments with modified moisture sounding

In the second set of experiments (DOC2A, DOC2B and DOC2C, see Table.6.1) to be reported in this section, the moisture sounding profile is modified to remove the dry layer at 700hPa level. The modified profile is shown in Fig.6.4 in thin dashed line.

Correspondingly, the θ_e there is increased so that it decrease monotonically from ground level to a minimum at the mid-levels (about 500hPa).

Corresponding to Fig.6.8, we show in Fig.6.14 the surface rainfall rates from these three experiments. It can be seen that storms developed over bell-shaped mountains (Fig. 14a,b) are very persistent and stationary, and are even more so than those in DOC1A and DOC1B where standard sounding was used. The maximum precipitation in both DOC2A and DOC2B is still falling directly over the mountain ridge by the end of simulation. In the case of the plateau type mountain, the trend of downslope (upstream) propagation of the storm is unchanged. The Storm in DOC2C is initially stronger than in DOC1C but it decays more quickly, as a result of even faster propagation of the cold outflow.

Fig.6.14. Hovmoeller diagrams of the surface rainfall rate (averaged over 2 minutes) in experiments DOC2A (a), DOC2B (b) and DOC2C (c) through four hours of model simulations. x=0 indicates the position of the mountain summit, or the edge of the flat plateau. (cf. Fig.6.7).

Fig.6.15. The flow fields (left panel) and the fields of θ' (right) at 2hrs (upper) and 4hrs (lower panel) of simulation DOC2A.

Fig.6.16. As in Fig.6.15 but for experiment DOC2B.

Fig.6.17. Flow fields (a) (b) and the fields of equivalent potential temperature (c) (d) from experiments DOC2C. (cf. Figs.6.12-13).

The flow fields and those of θ' from experiment DOC2A and DOC2B are shown in Fig.6.15 and Fig.6.16. Compared with those of experiment DOC1A and DOC1B (see Figs.6.8-11), the convective storm obtained here are more intense, the cold pools are weaker. Minimum θ' of the cold pool here is only -3 to -4K, instead of -6K as in previous cases. In fact, the air that forms the cold pool on the upwind slope is cooled due to primarily adiabatic ascent rather than rain evaporation. A relatively weak downdraught is only seen on the lee slope. Therefore we can say that the storms simulated in experiments DOC2A and DOC2B are closer to the observed Big Thompson storm.

The flow fields and θ' fields at 2 and 4hrs of simulation DOC2C are shown in Fig6.17. The general trend of system evolution is similar to that seen in DOC1C (Fig.6.12-13), but it happens quicker. At 2hrs a very strong downdraught is seen in Fig.6.17a lying along the slope of the plateau, bringing low θ_e air at the mid-levels right down to the mountain foot, resulting a cold temperature deficit of -8K. The cold pool temperature falls further to -12K by 3hrs.

Driven by this exceptionally strong cold pool the system propagates rapidly and then decays as a result (Fig6.17a,b). In this case, although the low-θ_e layer at the lower levels is removed, a strong cold pool forms still due to the descent of the low-θ_e air at the mid-levels, and also due to the blocking effect of the plateau to its left.

The above experiments show that the removal of the low-level dry, low-θ_e layer results in weaker cold pools for any of the bell-shaped mountain simulations and therefore in more stationary orographic storms. In fact the storm obtained in experiment DOC2A is the most persistent and stationary of all. The storm developed over the slope of a plateau is rapidly-propagating even when the dry layer at lower levels is removed. In this case, the cold pool forms as the strong downdraught brings mid-level low θ_e air down to the surface.

6.3.3 Orographic convection over lower mountains

A third set of experiments (DOC3A, DOC3B and DOC3C) are performed in which the mountain height is 1.0km, lower than in previous cases, in order to examine the effect of mountain height on orographic convective storm. The other specifications of this set of experiments are the same as for the first set (see Table.6.1). Since the results of experiment DOC3B differs from those of DOC3A only qualitatively, we will show the results of experiments DOC3A and DCO3C only and compare these results with those of DOC1A and DOC1C mainly.

Again we show first the rainfall rates at the surface produced by these two storms (Fig.6.19). Due to the lower height of mountain, the initiation of convection is slower therefore the rain reaches ground later than in previous cases (cf. Fig.6.7). The rain is less heavy too. The storm moves faster in DOC3A than in DOC1A, but slower in DOC3C than in DOC1C. The propagation speed of the storm is closely related to the intensity of rain-induced cold pool.

Fig.6.18. Hovmoeller diagrams of the surface rainfall rate (averaged over 2 minutes) in experiments DOC3A (a) and DOC3C (b) through four hours of model simulations. x=0 indicates the position of the mountain summit, or the edge of the flat plateau.

horizontal

Fig.6.19. Flow fields (upper panel) and those of θ' (lower panel) at 3 or 4hrs of simulation DOC3A. This experiment corresponds to DOC1A but the mountain is lower (h_m=1.0km).

upright

Fig.6.20. Flow fields (a) (b) and fields of θ' (c) (d) at 3 or 4hrs of simulation DOC3C. This experiment corresponds to DOC1C but the mountain is lower (h_m=1.0km).

In DOC3A, the bell-shaped mountain is lower than in DOC1A, the cloud base is therefore higher above the mountain surface so that this is larger depth for rain evaporation to occur. The result of this is the earlier formation and larger intensity of the cold pool on the upwind slope. At 2hrs, a rotor circulation is just about to be seen on the mid-slope of mountain (not shown), by 3hrs, the rotor is fully developed and its front has reached the mountain foot (x=16km, see Fig.6.19a), the minimum θ' of the cold pool is at this time -5K. The cold pool front surged ahead further during the next hour to x=28km (Fig.6.19b). The temperature deficit of the cold pool at 4hrs is about -8K, much colder that in DOC1A but not as cold as in the plateau type mountain cases because the downdraught is still relatively weak and the cold pool is mainly composed of air that is of low-level origin.

The development of storm in DOC3C is depicted in Fig.6.20. Again we see that the cold pool is very strong. Since the plateau is lower in this case, the convection is not as intense as in DOC1C, the downdraught is also weaker. The storm propagation is slightly slower.

The results of the experiments in this section suggest that mountain should have sufficient height not only to provide enough lifting of the low-level conditionally unstable air, but also to ensure that the cloud base is very close to the mountain surface so that rain evaporation is minimal. A quasi-stationary deep orographic storm can thereby be maintained in the absence of appreciable cold pool.

6.4 Summary and discussions

A series of numerical experiments using our σ-coordinate model have been reported in the chapter. These experiments, initialized using an original or a modified version of sounding taken prior to the Big Thompson storm, successfully reproduced the intense and quasi-stationary nature of that storm in certain runs. It is further shown that, with the given environmental sounding, the simulated storms are sensitive to the mountain profile. A bell-shaped mountain produces an intense quasi-stationary storm over the mountain

whereas a plateau type mountain produces a storm that tends to propagate quickly away from the mountain range. The storm remains quasi-stationary in the former case due to the lack of an appreciable cold pool on the upwind slope since air that is cooled by rain evaporation is mostly drained away from the other side of the bell shaped mountain range. When the mountain is of a semi-infinite plateau type, this cold air can not be drained away in the same way, it instead tends to run down the upwind slope to form density current which intensifies further and drives the convective line downslope away from the mountain range. The storm is therefore no longer stationary. Our experiments also show that the removal of a dry layer in the original sounding reduces the intensity of cold pool therefore helps in keeping the storm stationary. To maintain a storm stationary, the mountain also has to have a sufficient height so that the cloud base is close to the mountain surface therefore rain evaporation is minimal.

The real orography shown in Fig.6.3 is more like a plateau but the observed storm that developed over it was quasi-stationary. This discrepancy may be attributed to the two-dimensional assumptions made on both the storm system and the orography. In a strictly 2-D frame work, the possibility of drainage of cold outflow in the third dimensional is eliminated, this would clearly enhance the cold outflow on the upwind slope as in the plateau type mountain case. The three dimensionality of orography may also be important since cold outflow can possibly be drained from mountain valleys or over the ridge as in the bell-shaped mountain case. Moreover, our experiments are based on the single sounding constructed for Loveland after Caracena, et al. (1979), this sounding may not be exactly representative of the air mass that fed the Big Thompson storm. Clearly if the relative humidity of the low-level inflow was higher, the cold pool that forms would be expected weaker. Further studies on the environmental conditions and the three dimensionality of both the orography and the storm are clearly necessary.

N.B. On completion of this work, we recognized that very recently Yoshizaki and Ogura (1989) have also completed a numerical study on the Big Thompson storm. Their

mountain profile consists of a flat high plain with a gentle slope of 50km horizontal scale, which is rather close to our plateau type mountain. The Loveland sounding was modified to remove both the temperature inversion and lower relative humidity layer at the lower levels. They also noticed the existence of a cold pool but it was relatively weak. The storm remained quasi-stationary during a few hours of simulation.

Chapter Seven

Conclusions and Discussions

This thesis can be broadly divided into two parts. The first part consists of Chapters one to three, which gives a detailed account of the nonhydrostatic σ-coordinate model. Chapters four to six form the second part in which are applications of the model to various mesoscale meteorological problems.

The quasi-nonhydrostatic equation system in σ-coordinates was introduced in Chapter one together with discussions on the properties of the system. This system of equations has been derived by Miller and White (1984) using the small parameter expansion technique, while our model is the first attempt to solve it numerically. Not surprisingly, a number of problems have to be resolved while developing the model. It has been pointed out in Chapter one that two procedures of solving the equation system are possible, one of which solves the vertical momentum equation explicitly and the other derives the vertical velocity from the continuity equation. The former procedure was chosen since it treats both the horizontal and vertical velocity components in a similar fashion. The mass continuity in the model is ensured by an accurate solution of the elliptic equation. This equation is essentially a divergence equation.

The details of the model equations and the numerical formulations of dynamic processes were given in Chapter two, whereas the treatment of physical processes and the numerical techniques employed to advect thermodynamical quantities and to solve the elliptic equation for Φ' were presented in Chapter three

The Arakawa C-grid is chosen to represent the model variables which ensures the conservation of quadratic quantities by advective processes so as to effectively control nonlinear instability. As with all limited area numerical models, the definition of boundary

conditions is perhaps the most difficult part. This problem is further complicated in our model by the non-orthogonality of the coordinate system and the time dependence of the surface pressure. In spite of these, a radiative boundary condition due to Orlanski has been successfully applied on the lateral boundaries, and in certain situations an adjustment procedure is necessary to ensure the conservation of the total mass in the model domain. On the lower and upper boundaries, the conditions for velocities are specified under the constraint of mass continuity.

An efficient and accurate solution of the elliptic equation for Φ' [Eq.(2.1.10)] is another major issue with this model. Apart from the extra complexity of the forcing function on the right hand side of the elliptic equation, the presence of cross-differentiation terms with respect to x and σ on the left hand side makes the equation impossible to be solved directly using fast Poisson solvers. But fortunately, these cross-differentiation terms are generally at least one order of magnitude smaller than two major terms. A procedure of solution has been found which treats the less important terms explicitly and solve the resultant Poisson equation directly using a fast FFT solver. An acceptable accuracy is reached after typically two or three iterations associated with updated right hand side terms. To make the above problem complete, the value of Φ' at $\sigma=1$, i.e. the lower boundary condition of the elliptic equation, needs to be properly determined. But the way in which this is done is however not obvious. In the model, $\Phi'(\sigma=1)$ is related to the surface pressure based on the definition of the reference state, which is in a hydrostatic balance. As such a recursive equation (which would be a 2-D Poisson equation in a 3-D model) has to be solved. The overall procedure for solving the elliptic equation is found to be rather efficient.

As is well known that conventional second-order accurate advection schemes will generate 'negative water' when used in the water quantity conservation equations. This problem is eliminated in our model by using the Flux-Corrected Transport (FCT) scheme instead, the model accuracy is also greatly improved by using this advection scheme. Of course, the FCT scheme is more expensive than conventional methods, but the positive

contributions it makes towards improving the model accuracy prove its use to be well worthwhile.

In most of our experiments, an absorbing layer with a Rayleigh type damping is included near the top of the model domain in order to remove reflections from the top boundary. This method is found to be efficient in our calculations although a better boundary condition such as that of Klemp and Durran(1983) may be possible. Subgrid scale turbulence in the model is parameterized using the deformation and Richardson number dependent formulation due to Lilly (1962). A constant background diffusion is also included. Microphysical processes in the model include evaporation and condensation, auto-conversion and accretion and the evaporation and sedimentation of rain. Kessler's parameterizations are adapted. Solid water phases can be included in the future.

The results of our model calculations have confirmed the validity of the quasi-non-hydrostatic σ-coordinate equation system as suggested by the analysis of Miller and White (1984). This model has certain specific advantages. One of these is common to hydrostatic numerical models formulated in σ-coordinates (Phillips, 1957). In pressure-based coordinates thermodynamical (condensation and evaporation) calculations are more straightforward. Another outstanding advantage is that the nesting of this model with other large scale weather forecasting models which are generally in σ-coordinates is much more natural and easier. And it has been shown in chapter four that this model can be easily switched to its hydrostatic version which makes close comparisons between hydrostatic and nonhydrostatic solutions more direct and revealing than using totally different models. For certain problems, the hydrostatic version of the model is sufficiently accurate.

A major disadvantage of this model is the presence of fast Lamb wave modes in the system. It is not clear at present whether these can be easily removed. Lamb waves tend to limit the maximum time step that can be taken for time integration, however, this restriction is greatly relieved when the model grid length is small relative to the vertical scale of air motion. In this case the nonhydrostatic Lamb waves are significantly retarded.

For example, a six second time step was used in the deep orographic convection experiments where the horizontal grid length was 1km. According to the CFL condition for wave propagation on a staggered grid, the corresponding maximum phase speed of wave modes is less than 100m/s. In certain experiments (e.g. the squall line experiments in which 60 vertical levels were used), the limitation on the time step is from the small vertical grid length. As the horizontal grid length increases (e.g. in the experiments of inertial mountain gravity waves), the restriction on the time step becomes serious. Large time steps can not be used unless a mothod is found that eliminates or retards the Lamb waves. Using semi-implicit techniques such as time averaging of the geopotential height field, or possibly only the surface pressure may be a feasible way of solving this problem. At least, in applications we have carried out (Δx is around a few kilometres), the limitation on time steps imposed by Lamb waves has not been very serious.

Several mesoscale models (e.g. that of Klemp and Wilhelmson, 1978) are based on a fully compressible equation system, in which sound waves (both horizontal and vertical) are dealt with using time-splitting techniques. In general, a very small time step is used to describe the acoustic oscillations. While the computer code of such models is relatively simple, it is not advantageous either when the horizontal grid length is relatively large since in that case the time step will be limited mainly by the small vertical grid length. The anelastic equation system of Ogura and Phillips (1962) seems superior in this aspect but this also has problems when used to describe flows of large scales. These problems clearly deserve further investigation.

The model developed was verified and applied to a number of two dimensional problems. They includes those of dry and moist mountain gravity waves and related phenomena in stratified air stream flowing over a 2-D mountain ridge, and those of the long-lived squall lines and deep orographic convection.

In Chapter four, numerical solutions of steady state mountain gravity waves were obtained in various wave regimes. These solutions were quantitatively compared with analytical results and those obtained by other numerical models, very good agreement has

been found. The hydrostatic version of the model was also shown in this chapter to have produced consistent mountain wave solutions.

The 11 January 1972 Boulder severe downslope windstorm associated with the amplification of tropospheric mountain gravity waves was further studied using the σ-coordinate model. Our simulations demonstrated even more clearly the mechanism of wave amplification; the wave system amplified as a result of the fully nonlinear transition of the tropospheric flow from a subcritical to supercritical state whereas the existence of the lower level inversion layer and the creation of a nearly stagnant well mixed region by wave breaking played crucial roles. The final state of our simulation and the associated surface pressure drag were very close to the nonlinear analytical results of Smith (1985) and to those of observation. The possible mechanism of resonant interaction between the upward propagating waves and the downward reflected wave components is believed to be only of secondary importance.

Finally in Chapter four, trapped mountain lee waves were studied based on two real soundings taken over the west of the British Isles. Lee wave patterns seen from the satellite pictures were well reproduced. And the experiments showed that the trapped wave amplitudes were sensitive to the underlying topography spectrum as well as to the atmospheric structure. Experiments with increased lower-level humidity demonstrated the way in which lee wave structures were significantly modulated by moisture condensation. Convection was seen breaking out in certain regions. The sensitivities of the trapping and development of lee waves to mountain scale and height were also examined.

Intense, long-lived two-dimensional squall lines were studied in Chapter five. Experiments were designed to examine the role of the interaction between the cold pool outflow from the system and the low-level ambient inflow, and the mechanism by which such interaction determines and maintains an optimal state of squall line convection. It was shown that the orientation of the updraught is largely determined by the direction of propagation of the surface cold pool front relative to the cloud layer (layer above the cold pool) ambient flow, which in turn is determined by the relative strength between the cold

pool and the low-level ambient flow. A slightly upshear (with respect to the cloud-subcloud layer shear) tilting is the most efficient orientation of updraught in a squall line. An optimal condition for most intense, long-lasting squall lines was proposed based on the propagation speed of cold pool. The vorticity mechanism of Rotunno, Klemp and Weisman (1988) is not supported by our experiments, on the contrary, we believe the vorticity in the low-level inflow is largely irrelevant to the determination of the updraught orientation while it is the difference between the flow speed at the subcloud layer and that at the cloud layer that is important. Also in this chapter, the sensitivities of convection to the use of FCT scheme, and to spatial resolution and diffusion were also examined. The improvement in the model accuracy due to the use of FCT was found very significant.

In chapter six, deep orographic convection is studied using our σ-coordinate numerical model. A pre-storm environmental sounding was used to initialize the model in order to simulate the quasi-stationary Big Thompson storm that occurred over the Front Range of the Rocky Mountains and caused flash floods. Intense and quasi-stationary storm was obtained when the orography has either a symmetric or asymmetric bell-shaped profile, but the storm was fast propagating when a plateau type mountain was used. In the latter case, the rain induced cold pool was very strong due to the blocking effect of plateau. The removal of the low-level dry layer existing in the original sounding was found to reduce the intensity of cold pool therefore increase the stationarity of the storm. To maintain a stationary storm, sufficient height of the mountain is found also necessary to keep the cloud base close to the mountain surface so as to allow for little rain evaporation. Finally the possible impact of the two-dimensionality on the storm simulation are discussed.

In conclusion, a mesoscale numerical model that has certain unique features has been developed and verified. The successful applications of this model to a variety of mesoscale meteorological problems has shown both its efficacy and its potential of further development for applications to more complex mesoscale weather systems.

Appendix A A brief description of the leapfrog-trapezoidal transport algorithm

We outline in this appendix the high and low-order algorithms used in section 3.2 for the FCT scheme. We seek the finite difference approximations to equation (3.2.1),

$$\frac{\partial r}{\partial t} + \frac{\partial f}{\partial x} = 0 \qquad \text{(A1)}$$

We assume that at the beginning of a time step, values of r_i and f_i are known at grid points x_i and at time levels t-Δt and t. The leapfrog-trapezoidal finite difference approximation to Eq. (A1) in flux form is:

$$r'_i = r_i^{t-\Delta t} - [\, F^t_{i+1/2} - F^t_{i-1/2} \,]\, 2\Delta t / \Delta x_i \qquad \text{(A2)}$$

$$f_i^* = \frac{1}{2}\,(f_i^t + f'_i) \qquad \text{(A3)}$$

$$r_i^{t+\Delta t} = r'_i - [\, F^*_{i+1/2} - F^*_{i-1/2} \,]\, \Delta t / \Delta x_i \qquad \text{(A4)}$$

Here $F^t \equiv F(f^t)$ and $F^* \equiv F(f^*)$. The trapezoidal step Eq. (A3) and (A4) strongly damps the computational mode generated at the leapfrog step Eq. (A2). Time centring in both steps guarantees second order accuracy in time. The trapezoidal step is implemented in the model at every time step.

If Δx_i is independent of i, the functional form of the flux F of second order spatial accuracy (implemented in the model) is defined as

$$F_{i+1/2} = \frac{1}{2}\,(f_{i+1} + f_i) \qquad \text{(A5)}$$

Even higher order spatial differencing can also be used.

The low-order flux of the leapfrog-trapezoidal FCT schemes is simply the upstream-forward (donor cell) scheme plus a zeroth order diffusive flux with coefficient 1/8. The donor cell algorithm requires that f=ur, where u is an advective velocity. Specifically

$$F^L_{i+1/2} = u_{i+1/2}\, r^{DC}_{i+1/2} - \frac{1}{8}\,(x_{i+1} - x_i)(r^n_{i+1} - r^n_i) \qquad \text{(A6)}$$

where

$$r^{DC}_{i+1/2} = \begin{cases} r^n_i & \text{if } u_{i+1/2} \geq 0 \\ r^n_{i+1} & \text{if } u_{i+1/2} < 0 \end{cases} . \qquad \text{(A7)}$$

References

Alaka, M. A., Ed., (1960) *The Airflow over Mountains*. WMO Tech. Rep **34**, 135pp.

Anthes, R. A. and T. T. Warner, (1978) Development of hydrodynamic models suitable for air pollution and other mesometeorological studies. *Mon. Wea. Rev.*, **106**, 1045-1078.

Arakawa, A. and V. R. Lamb, (1977) Computational design of the basic dynamical processes of the UCLA general circulation model. *Methods in Computational physics*, **17**, Academic Press, 174-265, 337pp.

Asselin, R., (1972) Frequency filter for time integrations. *Mon..Wea. Rev.*, **100**, 487-490.

Beard, K. V., (1977) Terminal velocity and shape of cloud and precipitation drops aloft. *J. Atmos. Sci.*, **33**, 857-864.

Bluestein, H. B. and M. H. Jain, (1985) Formation and mesoscale lines of precipitation: Severe squall lines in Oklahoma during spring. *J. Atm. Sci.*, **42**, 1711-1732.

Boris, J. P. and D. L. Book, (1973) Flux-corrected transport: Part I SHASTA a fluid transport algorithm that works. *J. Comput. Phys.*, **11**, 38.

Bretherton, F. P., (1969) momentum transport by gravity waves, *Quart. J. R. Met. Soc.*, **95**, 213-243.

Browning, K. A., (1977) The structure and mechanism of hailstorms. *Meteor. Monogr.*, **38**, Amer. Met. Soc., 1-39.

Buzbee, B. L., G. H. Golub and C. W. Nielson, (1970) On direct methods for solving Poisson's equations. *SIAM J. Numer. Anal.*, **7**, 96-112.

Caracena, F., R. A. Maddox, L. R. Hoxit and C. F. Cappell, (1979) Mesoanalysis of the Big Thompson Storm, *Mon. Wea. Rev.*, **107**, 1-17.

Clark, T. L., (1976) A small scale dynamic model using a terrain-following coordinate transformation,. *J. Comput. Phys.*, **24**, 186-215.

———— and W.D. Hall, (1979) A numerical experiment on stochastic condensation theory. *J. Atmos. Sci.*, **36**, 470-487.

———— and W. R. Peltier, (1984) Critical level reflection and the resonant growth of nonlinear mountain waves. *J. Atmos. Sci.*, **41**, 3122-3134.

Cooley, J. W., P. A. W. Lewis and P. D. Welch, (1970) The fast Fourier transform algorithm: Programming considerations in the calculation of Sine, Cosine and Laplace transforms. *J. Sound Vib.* **12**, 315-337.

Corby, G. A. and C. E. Wallington, (1965) Airflow over a ridge: The Lee-wave amplitude. *Quart. J. R. Met. Soc.*, **82**, 266-274.

Crowley, W. P., (1968) Numerical advection experiments. *Mon. Wea. Rev.*, **96**, 1-11.

Deardorff, J. W., (1971) On the magnitude of the subgrid scale eddy coefficient. *J. Comput. Phys.*, **7**, 120-133.

————, (1972) Numerical investigation of neutral and unstable planetary boundary layers. *J. Atmos. Sci.*, **29**, 91-115.

Dudhia, J., M. W. Moncrieff and D. W. K. So, (DMS) (1987) The two-dimensional dynamics of West Africa squall lines. *Quart. J. R. Met. Soc.*, **113**, 121-146.

Durran, D. R., (1986) Another look at the downslope windstorms. Part I: On the development of analogue to supercritical flow in an infinitely deep, continuously stratified fluid. *J. Atmos. Sci.*, **43**, 2527-2543.

————, (1987) Another look at severe downslope winds: Part II *J. Atmos. Sci.*, **44**, 3402-3412.

———— and J. B. Klemp, (1982) The effects of moisture on trapped mountain lee waves. *J. Atmos. Sci.*, **39**, 2490-2506.

————, (1983) A compressible model for the simulation of moist mountain waves. *Mon. Wea. Rev.*, **111**, 2341-2361.

Eliassen, A., (1949) The quasi-static equation of motion with pressure as independent variable. *Geophs. Publik.*, **17**, No 3.

———— and E. Palm, (1960) On the transfer of energy in stationary mountain waves. *Geophs. Publik.*, **22**, 1-23.

Fovell, R. G. and Y. Ogura, (1988) Numerical simulation of a midlatitude squall line on two dimensions, *J. Atmos. Sci.*, **45**, 3846-3879.

Fulton, S. R., P. E. Ciesielski and W. H. Schubert, (1985) Multigrid methods for elliptic problems: A review. *Mon. Wea. Rev.*, **114**, 943-959.

Gal-Chen, T. and R. C. J. Somerville, (1975) Numerical solution of the Navier-Stokes equations with topography. *J. Comput. Phys.*, **17**, 276-310.

Gill, A. E. (1982) *Atmosphere-Ocean Dynamics*, Academic Press, 662 pp.

Grimshaw, R. H. J. and N. Smyth, (1986) Resonant flow of a stratified fluid over topography. *J. Fluid Mech.*, **169**, 429-464.

Grossman, R. J. and D. R. Durran, (1984) Interaction of low-level flow with the Western Ghat Mountains and off shore convection in the summer monsoon. *Mon. Wea. Rev.*, **112**, 652-672.

Haltiner, G. J. and R. T. Williams, (1980) *Numerical Prediction and Dynamic Meteorology*, second edition. J. Wiley and Sons, 477pp.

Harlow, F. H. and J. E. Welch, (1965) Numerical calculation of time-dependent viscous incompressible flow of fluid with free surface, *Phys. Fluids* , **8**, 2182-2189.

Hoskins, B. J. and A. J. Simmons, (1975) A multi-layer spectral model and the semi-implicit method, *Quart. J. R. Met. Soc.*, **101**, 637-655.

Johnson, M., (1978) The structure of vorticity in cumulonimbus convection: a numerical study. Ph.D. thesis, University of London.

Kessler, E., (1969) On the Distribution and continuity of water substance in atmospheric circulation. *Meteor. Monogr.*, **32**, Amer. Meteor. Soc., 84pp.

Klemp, J. B. and D. R. Durran, (1983) An upper boundary condition permitting internal gravity wave radiation in numerical mesoscale models. *Mon. Wea. Rev.*, **111**, 430-444.

———— and D. K. Lilly, (1975) The dynamics of wave induced downslope winds. *J. Atmos. Sci.*, **32**, 320-339.

————, (1978) Numerical simulation of hydrostatic mountain waves, *J. Atmos. Sci.*, **35**, 78-107.

Klemp, J. B. and R. B. Wilhelmson, (1978) The simulation of three-dimensional convective storm dynamics. *J. Atmos. Sci.*, **35**, 1070-1096.

Lilly, D. K., (1962) On the numerical simulation of buoyant convection. *Tellus*, **14**, 148-172.

————, (1978) A severe downslope windstorm and aircraft turbulence induced by a mountain wave. *J. Atmos. Sci.*, **35**, 59-77.

———— and J. B. Klemp, (1979) The effects of terrain shape on nonlinear hydrostatic mountain waves. *Fluid Mech.*, **95**, 241-261.

Lilly, D. K. and E. J. Zipser, (1972) The front range windstorm of January 1972-A Meteorological narrative. *Weatherwise*, **25**, 56-63.

Long, R. R., (1953) Some aspects of the flow of stratified fluids: Part I A theoretical investigation. *Tellus*, **5**, 42-58.

Ludlam, F. H., (1963) Server local storms: A review. *Meteor. Monogr.*, **5**, Amer. Met. Soc. 1-30.

Maddox, R. A., L. R. Hoxit, C. F. Chappell and F. Caracena,, (1978) Comparison of meteorological aspects of the Big Thompson and Rapid City flash floods. *Mon. Wea. Rev.*, **106**, 375-489.

Marshall, J. S. and W. McK. Palmer, (1948) The distribution of raindrops with size. *J. Meteor.* **5**, 165-166.

Miles, J. W. and H. E. Huppert, (1969) Lee waves in a stratified flow. Part IV: Perturbation approximation. *J. Fluid Mech.*, **35**, 497-525.

Miller, M. J., (1974) On the use of pressure as vertical coordinate in modelling convection. *Quart. J. R. Met. Soc.*, **100**, 155-162.

————, (1978) The Hampstead storm: a numerical simulation of a quasi-stationary cumulonimbus system. *Quart. J. R. Met. Soc.*, **104**, 413-427.

———— and R. P. Pearce, (1974) A three-dimensional primitive equation model of cumulonimbus convection. *Quart. J. R. Met. Soc.*, **100**,133-154.

Miller, M. J. and A. J. Thorpe, (1981) Radiation conditions for the lateral boundaries of limited-area numerical models. *Quart. J. R. Met. Soc.*, **107**, 615-628.

Miller, M.J. and A. A. White, (MW) (1984) On the non-hydrostatic equations in pressure and sigma coordinates, *Quart. J. R. Met. Soc.*, **110**, 515-533.

Moncrieff, M. W. and M. J. Miller, (1976) The dynamics and simulation of tropical cumulonimbus and squall lines, *Quart. J. R. Met. Soc.*, **102**, 373-394.

Newton, C. W., (1963) Dynamics of severe convective storms. *Meteor. Monogr.*, **5**, Amer. Met. Soc. 33-58

Ogura, Y. and M.-T. Liou, (1980) The structure of a midlatitude squall line. *J. Atmos. Sci.*, **37**, 553-567.

Ogura, Y. and N. A. Phillips, N. A., (1962) A scale analysis of deep and shallow convection in the atmosphere. *J. Atmos. Sci.*, **19**, 173-179.

Ogura, Y. and T. Takahashi, 1971: Numerical simulation of the life cycle of a thunderstorm cell. *Mon. Wea. Rev.*, **99**, 895-911.

Ogura, Y. and M. Yoshizaki. 1988, Numerical study of orographic-convective precipitation over the eastern Arabian Sea and the Ghat Mountains during the summer monsoon. *J. Atmos. Sci.*, **45**, 2097-2122.

Orlanski, I., (1976) A simple boundary condition for unbounded hyperbolic flows. *J. Comput. Phys.*, **21**, 251-269.

Orville, H. D., (1968) Ambient wind effects on the initiation and development of cumulus clouds over mountains. *J. Atmos. Sci.*, **25**, 385-403.

Peltier, W. R. and T. L. Clark, (1979) The evolution and stability of finite-amplitude mountain waves: Part II Surface wave drag and severe downslope windstorms, *J. Atmos. Sci.*, **36**, 1498-1529.

Phillips, N. A., (1957) A coordinate system having some special advantages for numerical forecasting. *J. Meteor.*, **14**, 184-185.

Pielke, R. A., (1984) *Mesoscale Meteorological Modelling.* Academic Press, 612pp.

Queney, P., (1947) Theory of perturbations in stratified currents with applications to airflow over mountain barriers. Dept. of Meteorology, Univ. of Chicago, Misc. Report No. 23.

————, (1948) The problem of airflow over mountains: A summary of theoretical studies. *Bull. Am. Met. Soc.*, **29**, 16-26.

Richtmyer, R. D. and K. W. Morton, (1967) *Difference Methods for Initial Value Problems.* Wiley (Interscience), New York, 406pp.

Robert, A. J., (1966) The integration of a low order spectral form of the primitive meteorological equations. *J. Met. Soc. Japan*, **44,** 237-245.

Rotunno, R., J. B. Klemp and M. L. Weisman, (RKW) (1988) A theory for strong, long-lived squall lines, *J. Atmos. Sci.*, **45**, 463-485.

Sawyer, J. S., (1960) Numerical calculation of the displacements of a stratified airstream crossing a ridge of small height. *Quart. J. R. Met. Soc.*, **86**, 326-345.

Scorer, R. S., (1949) Theory of lee waves of mountains *Quart. J. R. Met. Soc.*, **75,** 41-56.

Seitter, K. L., (1986) A numerical study of atmospheric density current motion including the effects of condensation. *J. Atmos. Sci.*, **43**, 3068-3076.

Smagorinsky, J., (1963) General circulation experiments with primitive equations: Part I The basic Experiment. *Mon. Wea. Rev.*, **91**, 99-165.

Smith, R. B., (1979) The influence of mountains on the atmosphere. *Advances in Geophysics*, **21**, Academic Press, 87-230.

————, (1985) On severe downslope winds. *J. Atmos. Sci.*, **42**, 2597-2603.

Smull, B. F. and R. A. Houze, Jr., (1987) Rear inflow in squall lines with trailing stratiform precipitation. *Mon. Wea. Rev.*, **115**, 2869-2889.

Soong, S-T. and Y. Ogura, (1973) A comparison between axis-symmetric and slab-symmetric cumulus cloud models. *J. Atmos. Sci.*, **30**, 879-893.

Swarztrauber, P. N., (1977) The methods of cyclic reduction, Fourier analysis and the FACR algorithm for the discrete solution of Poisson's equation on a rectangle. *SAIM Review*, **19**, 490-501.

Sweet, R. A., (1977) A cyclic reduction algorithm for solving block tridiagonal systems of arbitrary dimension. *SAIM J. Numer. Anal.*, **14**, 706-720.

Tapp. M. C. and P. W. White, (1976) A non-hydrostatic mesoscale model. *Quart. J. R. Met. Soc.*, **102**, 277-296.

Thorpe, A. J., M. J. Miller and M. W. Moncreiff, (TMM) (1982) Two-dimensional convection in non-constant shear: a model of mid-latitude squall lines, *Quart. J. R. Met. Soc.*, **108**, 739-762.

Wallace, J. M. and P. V. Hobbs, (1977) *Atmospheric Science: An introductory Survey*, Academic Press, 467pp.

Weisman, L. W., J. B. Klemp and R. Rotunno, (WKR) (1988) Structure and evolution of numerically simulated squall lines, *J. Atmos. Sci.*, **45**, 1990-2013.

Wilhelmson, R. B. and J. H. Ericksen, (1977) Direct solutions for Poisson's equation in three dimensions. *J. Comput. Phys.*, **25**, 319-331.

Wilhelmson, R. B. and Y. Ogura, (1972) The pressure perturbation and the numerical modelling of a cloud. *J. Atmos. Sci.*, **29**, 1295-1307.

Williams, G. P., (1969) Numerical integration of the three-dimensional Navier-Stokes equations for incompressible flow. *J. Fluid Mech.*, **37**, 727-750.

Zalesak, S.T., (1979) Fully multidimensional flux-corrected transport algorithms for fluids. *J. Comput. Phys.*, **31**, 336-362.

List of symbols

'	prime denoting perturbation or deviating variables
–	overbar denoting average or reference state
a	half-width of bell-shaped mountain
α	parameter for Robert time filter
A_r	rainwater auto-conversion rate
c, C	Sound wave phase speed, phase speed of other physical waves
c, C, C_*	propagation speed of density current or thunderstorm cold outflow front
$\hat{c}$	estimated disturbance propagation speed for radiative boundary conditions
C_g	group velocity of physical waves
C_p, C_v	specific heat of dry air at constant pressure and constant volume respectively
C_r	rainwater accretion rate
D	pressure drag due to mountain gravity waves
$\Delta\sigma$	grid interval between σ levels
Δt	time integration step
D_u, D_w, D_θ, D_q	diffusion or turbulence mixing terms for various equations
Δx	grid interval in x direction
E	total energy
E_r	rainwater evaporation rate
e_s	saturation vapour pressure
f	Coriolis parameter, arbitrary function
Φ, Φ', Φ_s	geopotential height, the perturbation and that of the reference state
F_e	mountain gravity wave energy flux
F_Φ	forcing function for Φ' equation

Fr	Froude number
Γ	stratification parameter $1/2\ d\ln\rho_s/dz$
g	acceleration due to gravitation
γ	ratio of specific heat at constant pressure to that at constant volume, $\gamma \equiv C_p/C_v$
H	heat flux, scale height, layer depth parameter
h	mountain height
η	y-component of vorticity vector
h_m	maximum height of mountain
i, j	grid point index in x and σ direction respectively
K	diffusion coefficient
k	horizontal wavenumber
κ	total wave number, parameter R/C_p
K_{BG}	coefficient for background diffusion
K_D, K_R	coefficients for sponge layer damping
K_m, K_H, K_q	diffusion coefficients for momentum, temperature, water quantities
L	latent heat of condensation of water, horizontal scale length
l	Scorer parameter
m	wavenumber in vertical direction
M_θ, M_q	terms representing parameterized microphysical processes
n	index of time levels, wavenumber in y direction
N, N_s	Brunt-Vaisala frequency
NX, NS	number of grid points in x and σ direction respectively
P	mass weighted pressure
Π	nondimensional pressure $\Pi \equiv (p/p_0)^\kappa$
p	pressure
p_*	difference between p_{surf} and p_{top}
p_0	constant pressure of 1000HPa
p_{surf}, p_{top}, p_t	pressure at the lower surface and top of model domain

θ	potential temperature
θ', θ_s	potential temperature for perturbation and reference state
q_v, q_c, q_r	mixing ratios for water vapour, cloud water and rainwater
$\dot{Q}$	heat source or sink
R	gas constant for dry air, residual of elliptic equation for Φ'
ρ, ρ_0, ρ_s, $\bar{\rho}$	air density
Ri	Richardson number
R_o	Rossby number
S	scale height parameter
σ	independent variable in σ-coordinates, $\sigma \equiv (p-p_t)/p_*$
s	suffix denoting the reference state
$\dot{\sigma}$	velocity component in σ coordinate direction
T	nondimensional time, absolute temperature
t	time, temperature in Celsius
τ_{ij}	stress tensor
u'	perturbation x-velocity
U, $\bar{U}$, U_0	basic flow speed in x direction
U, V, W	mass weighted velocity components in x, y, z direction respectively
u, v, w	velocity components in x, y, z direction respectively
UFLUX, WFLUX, TFLUX, QFLUX	flux terms in u, w, θ' and q equations
v	vector velocity
V_t	terminal fall speed of rainwater
w, $\tilde{w}$	vertical velocity in σ-coordinates
x, y, z	independent variables in Catesian coordinates
ψ, Ψ	arbitrary functions

Acknowledgement

The author is deeply indebted to his supervisor, Dr. Alan J. Thorpe, for his enlightening guidance and continual encouragement throughout, without which the completion of this thesis would not have been possible.

He also would like to thank Dr. M. J. Miller of Eropean Centre for Medium Range Weather Forecasting, and Dr. B. Johns for many useful suggestions on this work. Discussions on issues in Chapter five with Dr. Steven Garner is gratefully acknowledged here. Thanks are also due to Dr. R. Saktreger for arranging computing facilities and introduction to computer systems. Excellent facilities provided by University of London Computer Centre, Rutherford Appleton Laboratory and University of Reading Computer Centre are deeply appreciated.

This author would like to thank Dr. Zuojun Zhang, for his initiative and cooperation in developing graphic analysis package ZXPLOT which generates all the pictures of model output in this thesis. He is grateful to Liu Xia for typing the references and part of chapter five, and for her encouragement during the course of writing up. The encouragement and care from his parents throughout the period of study are beyond the literal expressions.

The author's thanks are due to Dr. Chris Thorncroft for reading through part of the text.

This work was supported by the Chinese State Educational Commission and the British Council through Technical Cooperation Award.